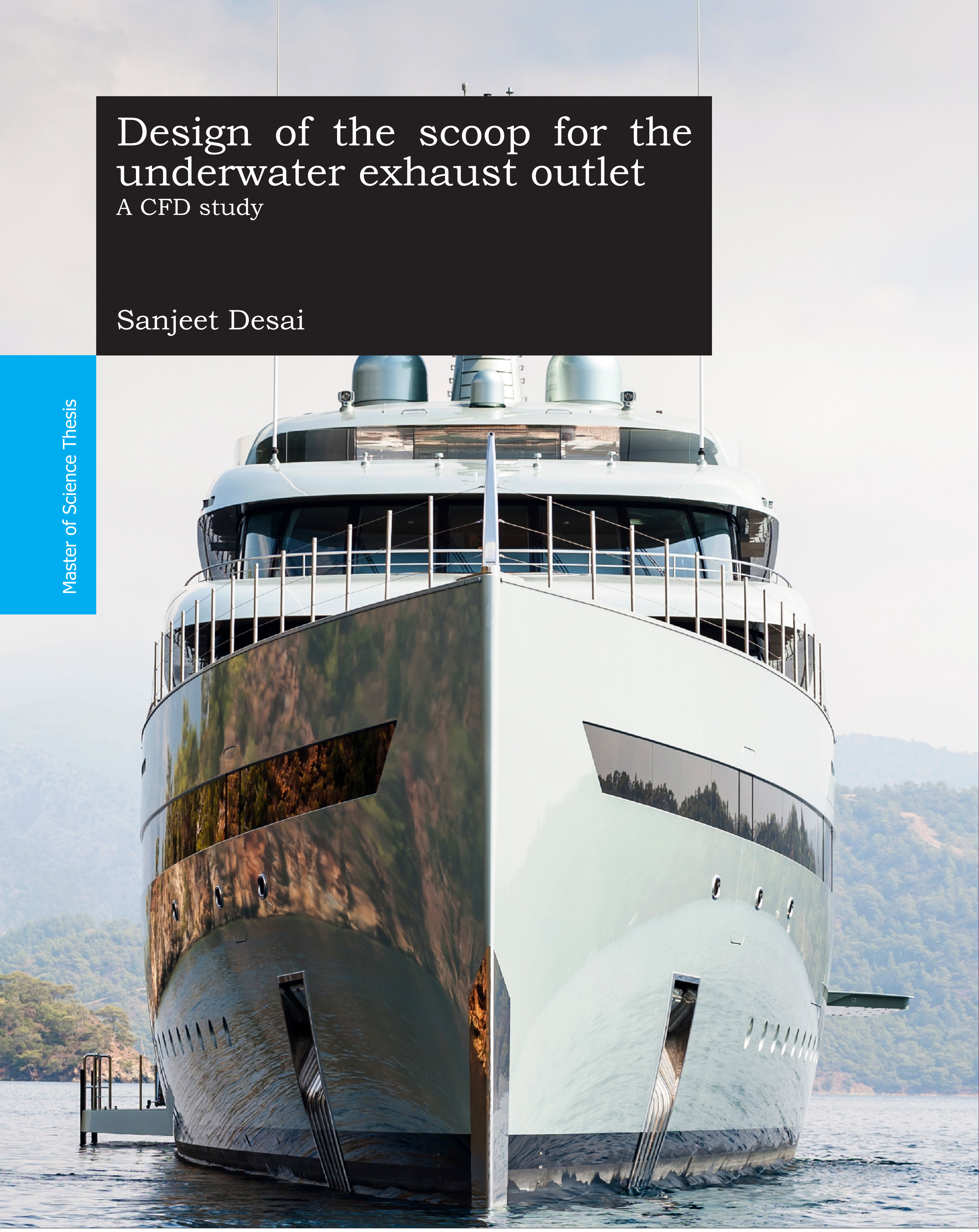

Design of the scoop for the underwater exhaust outlet

A CFD study

Sanjeet Desai

Master of Science Thesis

TU Delft
Delft University of Technology

De Voogt
Naval Architects

Challenge the future

Design of the scoop for the underwater exhaust outlet

A CFD study

by

Sanjeet Desai

in fulfillment of the requirements for the course of

AE5110 Master Thesis
in Faculty of Aerospace Engineering

at the Delft University of Technology.
to be defended publicly on October 25, 2018 at 01:00 PM.

Student number:	4622286	
Project duration:	January 1, 2018 – Septemebr 28, 2018	
Thesis committee:	Dr. ir. M. Gerritsma,	Delft University of Technology
	Ir. O. Boelens,	De Voogt Naval Architects
	Ir. L. Rietveld,	De Voogt Naval Architects
	Dr. ir. S. Hickel,	Delft University of Technology
	Dr. ir. M. Snellen,	Delft University of Technology

TU Delft Delft University of Technology

DE VOOGT NAVAL ARCHITECTS

The work in this thesis project was supported by De Voogt Naval Architects B.V.

Cover image courtesy of Feadship, [9].

Preface

This report is the result of the graduation project performed over nine months at the De Voogt Naval Architects B.V.

This project enabled me to look into the specific applications of CFD in maritime engineering, while at the same time enabled me to apply the knowledge obtained at the university. It was an interesting learning experience where each new step provided a further insight into yacht design.

I would like to thank my supervisors, Ir. Okko Boelens and Ir. Stephanie van den Brink for the constant guidance and feedback on the project. I appreciate the freedom and trust I received throughout the project. Furthermore, I would like to thank Ir. Leon Rietveld for assisting me with the understanding of the exhaust systems. Also, I would like to thank Dr. ir. Marc Gerritsma at Delft University of Technology for his valuable help.

Finally, I would like to thank De Voogt Naval Architects B.V. and Delft University of Technology to provide me with a wonderful opportunity to perform this graduation project.

Sanjeet Desai
Delft, October 2018

Summary

Luxurious Feadship yachts are designed for the leisure and cruising across the oceans. These luxury yachts are mostly powered by diesel engines or in some cases, a diesel-hybrid system. To prevent the inconvenience and the discomfort arising from the diesel exhaust gases for passengers, Feadship yachts are equipped with an underwater exhaust outlet. These underwater exhaust outlets are located on the side of the hull close to the dynamic waterline. It consists of an external appendage called ”scoop” which creates a low pressure region for the exhaust outlet. During recent sea trials of the Feadship yachts, undesirable variations in the exhaust back-pressure were observed at the underwater outlet. These undesirable variations led to a situation with either too high back-pressure or too low back-pressure. An excessive back-pressure will increase the fuel consumption and will damage the diesel engine. Contrary, an extremely low back-pressure will give a visible exhaust flow above water thereby discolouring the hull and contaminating the deck with exhaust gases and steam.

An ideal scoop design would substantially reduce the above described problems. To investigate the optimal design for a scoop, a numerical method will be used. The method applicable in this study will be the Mutiphase Flow models from the commercial Computational Fluid Dynamics (CFD) software called Star CCM+. A multiphase fluid interaction between the exhaust gases and sea water will be examined to find the physical phenomenon affecting the back-pressure at the underwater outlet. In return, this phenomenon will be useful for a thorough analysis of the different scoop designs and how this design could impact the back-pressure. Furthermore, the validation of the numerical method will be carried out against the data procured from sea trials of the yachts with current scoop design.

To conclude, design recommendations for an optimal scoop geometry will be provided such that it can reduce the excessive back pressure, have a low resistance and prevent the discolouring of the hull.

Contents

List of Figures

List of Tables

Abbreviations

FEADSHIP	First Export Association of Dutch SHIPbuilders
CFD	Computational Fluid Dynamics
CCM	Computational Continuum Mechanics
CAD	Computer Aided Design
SCR	Selective Catalytic Reactor
CO_2	Carbon Dioxide
H_2O	Water
N_2	Nitrogen
O_2	Oxygen
MTU	Motoren- und Turbinen-Union
MARIN	MAritime Research Institute Netherlands
SST	Shear Stress Transport
DNS	Direct Numerical Simulation
LES	Large Eddy Simulation
RANS	Reynolds Averaged Navier-Stokes
RST	Reynolds Stress Transport
VOF	Volume Of Fluid
TID	Technical Investigation Department
GPS	Global Positioning System

List of Greek symbols

ρ	Density	kg/m^3
μ	Dynamic viscosity	$Pa\,s$
ω	Specific dissipation rate	s^{-1}
ϕ	Solution variable	-
$\bar{\phi}$	Mean solution variable	-
$\phi^{'}$	Fluctuating solution variable	-
τ_{ij}	Newtonian viscous stress	-
ϵ	Dissipation rate	m^2/s^3
α	Volume fraction	-
τ_w	Wall shear stress	Pa
ϕ_i	Arbitrary flow quantity	-
ϕ_{exp}	Experimental value	-

List of Roman symbols

p, P	Pressure	Pa
Δp, ΔP	Internal pressure loss	Pa
ΔP_B	Exhaust Back-pressure	Pa
ΔP_{scoop}	Pressure at the underwater outlet	Pa
k	Turbulent kinetic energy	m^2/s^2
V	Velocity	m/s
C_p	Specific heat	$J/(kg \cdot K)$
$y+$	Dimensionless wall distance	-
y	Normal distance from the wall to the wall-cell centroid	mm
ν	Kinematic viscosity	m^2/s
u^*	Reference velocity	m/s
R_{rms}	Root Mean Square of residual value	-
R_{pres}	Normalized residual value	-
R_{norm}	Normalization value	-
U_{val}	Validation uncertainty	-
U_{ϕ}	Numerical uncertainty	-
U_{inp}	Parameter uncertainty	-
U_{exp}	Experimental uncertainty	-
E	Validation comparison error	-

1
Introduction

This chapter provides an introduction to the proposed research work. It will further provide the information about the report structure. The chapter ends by presenting the main research question to be solved during the proposed work and the final research objective.

1.1. Description

Generally, Feadship yachts which are powered by diesel combustion engines are equip-ped with exhaust funnels exposed to the atmosphere. Such a configuration can cause several discomforts to the passengers on-board like: 1) Diesel smoke; 2) Pungent smell; and 3) Noise. To overcome these problems, modern Feadship yachts incorporate underwater exhaust outlets to release the exhaust gases in the sea water. The underwater exhaust outlets are normally located on the side of the hull and close to the dynamic waterline of the yacht. Furthermore, the underwater outlet is provided with an external appendage known as ″scoop″. The scoop facilitates the creation of a low pressure region near the outlet to help exhaust gases flow out easily in the sea water.

Recent sea trials of Feadship yachts indicated the unwanted back-pressure behaviour with the current scoop design at the underwater outlet. The behaviour could be separated into two parts; 1) the excessive back-pressure and 2) too low back-pressure at the underwater outlet. An excessive back-pressure results in the increased wear and tear of the engine components thereby decreasing the operational lifespan, [31]. Furthermore, such a condition also results in an increased fuel consumption as the engine needs to work more to push out the exhaust gases. In contrast, an extremely low back-pressure will allow the exhaust gases to escape from the water possibly resulting in discolouring of the hull and deck contamination with exhaust gases and steam. This behaviour of the scoop was deemed undesirable. To enable evaluating several scoop designs, a numerical model will be studied to predict the flow behaviour between exhaust gases and sea water.

Multiphase Flow models will be used from the commercial Computational Fluid Dynamics (CFD) software called Star CCM+ developed by Siemens. Initially, multiphase fluid interaction between the exhaust gases and sea water will be examined to identify the physical phenomenon responsible for the back-pressure behaviour at the scoop. The established model will then be validated against the data procured from the sea trials of the yacht with the current scoop design.

Knowledge of the identified phenomenon will be employed to improve the scoop design to establish the desired performance of the underwater outlet. This will be achieved through a steady state analysis of a parametric scoop design by varying the different geometric parameters affecting the back-pressure at the outlet. To further refine the design, the scoop geometry will be incorporated in a simplified geometry in the unsteady multiphase flow model to study the interaction of exhaust gases with sea water, [16]. Finally, a full scale model with the improved scoop design will be analyzed to study the exhaust flow behaviour upon interaction with the waves induced by the yachts.

In conclusion, the research study will provide design recommendations for the scoop geometry for the underwater exhaust outlet. The improved scoop will have a low resistance and will be able to provide a greater control over the back-pressure at the underwater outlet thereby preventing the engine and hull damage.

1.2. Report structure

This report describes the literature study and the research carried out for the thesis project. Chapter 2 discusses the different types of exhaust systems and its ramification on the marine vessels. Additionally, the background of the problem is presented in detail in this chapter. A literature study with regards to the research topic is presented in Chapter 3.

Chapter 4 describes the background and the setup of the numerical model for the CFD simulation. The validation of the CFD model is presented in Chapter 5.

The following chapters present the results from the CFD simulations. Chapter 6 discuss the findings from the simulations of the baseline geometries of the scoop. Chapter 7 presents the modified baseline geometries and the implications on the exhaust system. New design recommendations for the scoop geometries are shown in Chapter 8. It further shows the advantages of the new geometries over the baseline geometries.

Finally, Chapter 9 provides the conclusions for the thesis project. It further presents the recommendations for future research.

Note: Due to confidentiality reasons, the detailed specifications of Feadship yachts and diesel engines are not mentioned.

1.3. Objectives

The main research questions pertaining to the given task is presented below:

"Which parameters affect the performance of the scoop at the underwater exhaust outlet?"

The goal / aim of this research is to provide design recommendations for the scoop geometry which can help to control the excessive back-pressure at the underwater exhaust outlet. Additionally, the scoop design should be able to keep the exhaust gases submerged to prevent hull fouling and polluting the deck with smoke and fumes. Furthermore, the scoop should have a low resistance geometry to improve the hydrodynamic efficiency of the hull. The above goal is planned to be achieved by performing a numerical analysis of various scoop designs using multiphase flow models and investigating the impact of the scoop design on the back-pressure of the underwater exhaust system. The final research objective can be framed as follow:

"Designing a scoop for the underwater exhaust outlet by numerically analyzing the effect of the scoop design on the back-pressure of the underwater exhaust system"

The objective statement represents the required criteria for successful implementation of the scoop design as optimal back-pressure at the underwater outlet and prevention of hull fouling/deck contamination. In order to achieve the objective, the following fundamental goals need to be accomplished:

- Study the existing scoop design and its impact on back-pressure by means of a literature review
- Validating the numerical model with the data obtained from sea trials
- Study the design parameters of the scoop influencing the back-pressure at the underwater outlet
- Study the behaviour of exhaust flow interaction in presence of multiple underwater exhaust outlets
- Design a novel scoop that can achieve the required criteria as discussed in the paragraph above

Required actions to accomplish the above mentioned fundamental goals:

- Analyze the validation data
- Create a parametric scoop geometry (different aspect ratio, diameter, etc.)
- Implement the multiphase flow model to perform flow analysis on the exhaust system
- Perform a mesh sensitivity test for the fluid domain
- Perform the CFD simulations for various scoop geometries using Star CCM+

These are some of the important actions that need to be performed in order to achieve the primary objective. Apart from the above mentioned actions, some CFD related questions need to be answered like optimal solver settings, time-steps, type of mesh and domain size.

2
Problem Background

The chapter presents the classification of different exhaust systems and its ramifications on the marine vessel. Furthermore, it discusses the properties of the exhaust gas to be considered for CFD simulations. The chapter ends by discussing the consequences of the exhaust back-pressure on the engine performance and the deck atmosphere.

2.1. Exhaust systems

This section provides an overview of the different exhaust systems currently in use with the recreational ships. The exhaust systems for the recreational ships can be divided into three types namely dry exhaust system, wet exhaust system and underwater exhaust system.

2.1.1. Dry exhaust system

Dry exhaust systems are not the most common type preferred for the recreational ships. In this system, the exhaust smoke is usually transferred in a vertical pipe passing through the decks from engine. The exhaust smoke is then discharged into the atmosphere through the use of a funnel (smokestack or chimney) as seen in Figure 2.1.

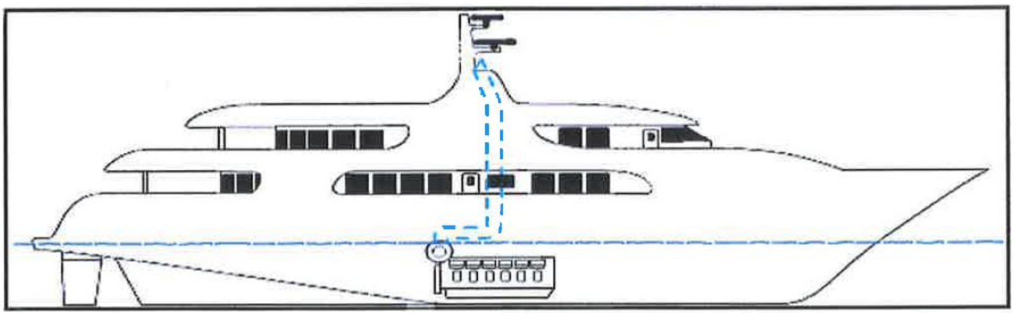

Figure 2.1: Dry exhaust system [10]

The advantage of the dry exhaust system is the low level of complexity as it does not require any water injection system to cool the exhaust gas. Moreover, the maintenance is low due to the simple construction. However, the dry exhaust system requires a large amount of space for the exhaust pipe layout and a significant production time. Furthermore, due to the absence of water-cooling, the temperature of the exhaust gas is extremely high posing a significant threat of burn injury.

Kulkarni et al. [17] review the nuisance of smoke from the dry exhaust system and the possible solutions to minimize them. One of the major nuisances due to a dry exhaust includes contamination of the top decks due to the discharge of smoke from the exhaust funnel. This is especially a major problem for the recreational ships where the comfort of the passenger is of prime importance.

The problem has been analyzed through the use of wind-tunnel experiments, analytical methods, field measurements and recently through CFD. The investigation of the problems mostly focused around the optimization of the funnel shape and stack length. However, as most of investigations belong to naval and defence applications, they are not available in open literature.

From the perspective of recreational ships, deck contamination is a serious issue for the comfort of the passengers. Hence, the use of a dry exhaust system is not preferred in yachts.

2.1.2. Wet exhaust system

A wet exhaust system provides a good alternative for a dry exhaust system. In this system, seawater is injected into the exhaust gas and the mixture is then discharged slightly above the waterline through the outlet as seen in Figure 2.2.

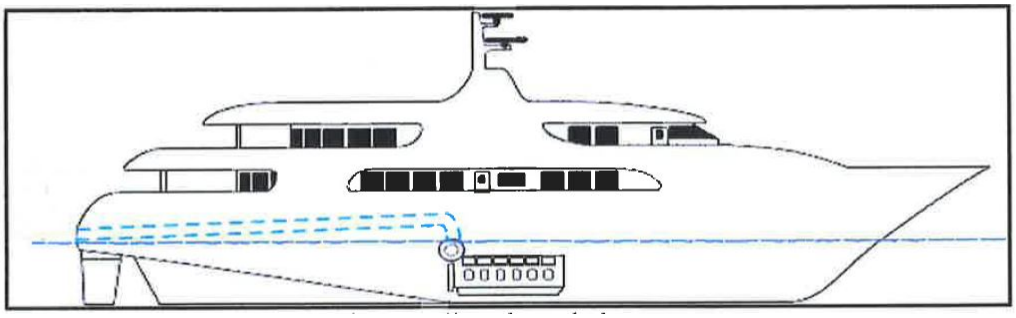

Figure 2.2: Wet exhaust system [10]

The advantage of the wet exhaust system is the reduced temperature of the exhaust gas and no deck contamination. The low temperature eliminates the risk of being burnt due to exhaust gas. However, there are several downsides related to this system. Firstly, the addition of a water injection system makes the system complex and high in maintenance. Moreover, in case of a poor design or system failure, there is possibility of water leakage into the engine compartment. Also, a faulty design of the wet exhaust pipe can lead to a prime source of noise and vibrations.

Most of these systems evolved out of professional experience rather than research. Furthermore, the usage of wet exhaust system is limited to small recreational boats. Additionally, the research content on this topic is limited or is not available in open literature.

2.1.3. Underwater exhaust system

Similar to the wet exhaust system, sea-water is injected into the exhaust gas to lower the temperature for these systems. The exhaust gas is then discharged underwater slightly below the waterline as depicted in Figure 2.3.

This type of exhaust system is mostly used in the recreational ships to prevent deck contamination and to reduce the vibrations generated due to exhaust systems. Further-

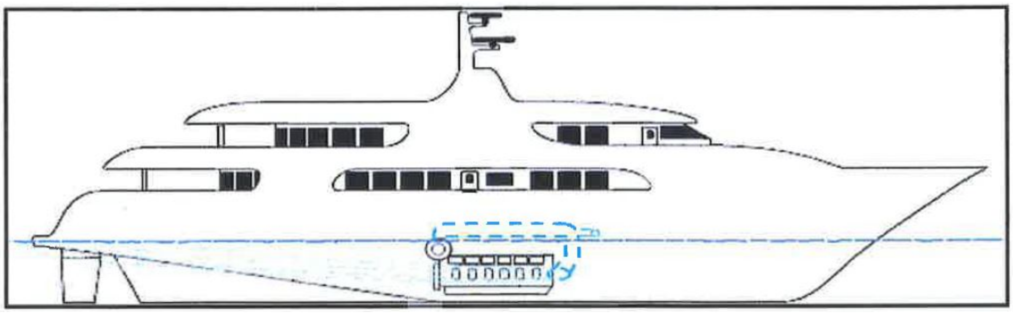

Figure 2.3: Underwater exhaust system [10]

more, such systems are also employed for submarines to minimize the head signature as required by their operational profile.

The underwater exhaust systems for surface ships can be accompanied by an external appendage called scoop. The exhaust outlet and scoop can be located either on the side or the bottom of the hull. A schematic presentation of the types of exhaust scoop is given in Figure 2.4. The image provides an example of a possible scoop geometry placed on the underside of the hull. The exhaust scoops facilitate the creation of a low pressure region near the outlet by increasing drag force and wake behind the exhaust pipe. This helps the exhaust gases to flow out easily in the sea-water.

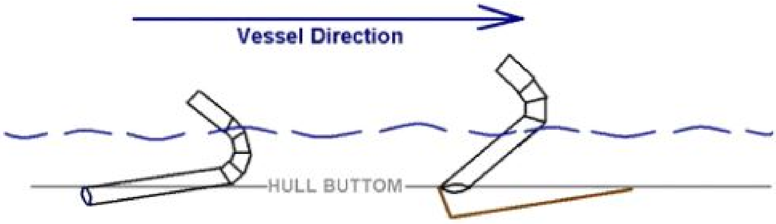

Figure 2.4: Side view - Scoop for the underwater exhaust system at the underside of the hull [37]

A theoretical analysis of the scoop and its impact on exhaust back pressure has been carried out by Ganzeveld, [10]. It is discussed in detail in Section 3.1. Furthermore, Delvoye, [4], investigated the single phase, steady state flow around the underwater exhaust scoop to study its impact on the back-pressure. The discussion is presented in Section 3.2.

2.2. Exhaust gas properties

This section describes the physical properties of the exhaust gas. These properties are important for the design of exhaust systems and will be required as an input for the CFD simulations. It must be noted that most of the data for the physical properties of the exhaust gas are obtained from open literature. Experimental data is not available for all the physical quantities.

The gases that needs to be discharged from the yachts are the exhaust gases of the diesel engine. As stated by Jääskeläinen, [13], the exhaust gas contains an increased concentration of water vapour (H_2O) and carbon dioxide (CO_2) relative to the ambient air. These concentrations may vary by a few percent depending on the engine load. The volumetric concentration of the exhaust gas components is shown in Table 2.1.

Table 2.1: Volumetric concentration of exhaust gas components [13]

Component	Concentration
CO_2	2-12 %
H_2O	2-12 %
O_2	3-17 %
N_2	59-93 %

The major concentrations in the exhaust gas are oxygen (O_2) and nitrogen (N_2). Their concentration will be reduced by few percents at high engine loads. The error associated with the change in these concentrations is usually less than 2%, [13]. Thus, as an approximation the properties of air can be used for the calculations.

For some of the Feadship yachts, the temperature of the exhaust gas was measured at the end of turbocharger outlet in the diesel engine. As per the information provided in [25], the properties of the exhaust gas can be derived from the physical properties of air at atmospheric pressure. The density and the dynamic viscosity of the exhaust gas at 420$^\circ C$ is presented in Table 2.2.

Table 2.2: Physical properties of exhaust gas [25]

Temperature (K)	Density (kg/m^3)	Dynamic Viscosity ($Pa \cdot s$)
350	0.995	$2.08x10^5$

2.3. Effect of exhaust back-pressure on diesel engine performance

This section examines the effect of the static back-pressure on the performance of the marine diesel engine from the investigation performed by Sapra et al., [31]. Emissions from marine vehicles are subjected to strict international regulations like IMO Tier III. To meet the requirements, the marine diesel engines are fitted with after-treatment technologies such as scrubbers or Selective Catalytic Reactors (SCR), [20]. Such additions to the exhaust system leads to pressure loss in the exhaust gas.

Additionally, underwater exhaust systems are becoming the latest trend in the shipping industry. Such systems avoid polluting the atmosphere directly, consume less space in the engine room and reduce noise and smoke contamination on the decks, [31]. Also, underwater exhaust systems reduce the thermal signature for naval ships and help to provide aesthetic appearance to recreational ships. In contrary, the exhaust flow from an underwater exhaust system experiences increased flow resistance due to the hydrostatic pressure from the water column.

Tauzia et al. [36], briefly describe the effects of the dynamic back-pressure due to the partially submerged exhaust on the marine diesel engine. It was concluded that the short wave period alongside a low engine loading can lead to water penetration inside the exhaust pipe, thereby increasing the back-pressure.

According to Sapra et al. [31], it was established that the increased back-pressure at the underwater outlet could lead to an increase in fuel consumption, high temperatures at the turbochargers inlet and incomplete combustion.

With the increased back-pressure, engines need to work more to pump out the exhaust gases. This increases the load on the engine, thereby increasing the fuel consumption. Furthermore, for the increased fuel consumption, the air intake remains constant which leads to an incomplete combustion. This reduces the combustion efficiency and produces black smoke which is undesirable for naval ships and recreational yachts.

Additionally, the effect of low back-pressure cannot be ignored. Although low back-pressure does not have a negative impact on the engine lifespan, such a condition facilitates the escape of exhaust gases from water which deteriorates the paint job of the hull and pollutes the deck environment. The effect can be clearly seen on the Feadship yacht in Figure 2.5.

Figure 2.5: Hull discoloration

To conclude, the increased back-pressure due to the underwater placement of the exhaust outlet is detrimental to the engine performance. To overcome this negative impact of the underwater exhaust outlet, there is a need for an external appendage which can counteract the hydrostatic pressure and maintains the back-pressure within desirable limit.

3

Literature Review

With the general background provided for the problem, this chapter will give an overview of the work that has been carried out on the related topics. It gives an impression of the current understanding and the methods employed in recent studies. First, a theoretical analysis of the underwater exhaust system is provided followed by the steady state analysis of the exhaust scoop. The last section takes a look at the use of multiphase flow models for the study of underwater exhaust systems and the effect of sea-trial conditions on the model validation.

3.1. Theoretical analysis of underwater exhaust system

This section analyzes the different sources of pressure loss within the underwater exhaust system. Furthermore, a theoretical analysis is carried out to calculate the approximate pressure loss within the entire exhaust system, [10]. This will also help to identify the potential areas within the exhaust system that can be optimized.

3.1.1. Division of the underwater exhaust system

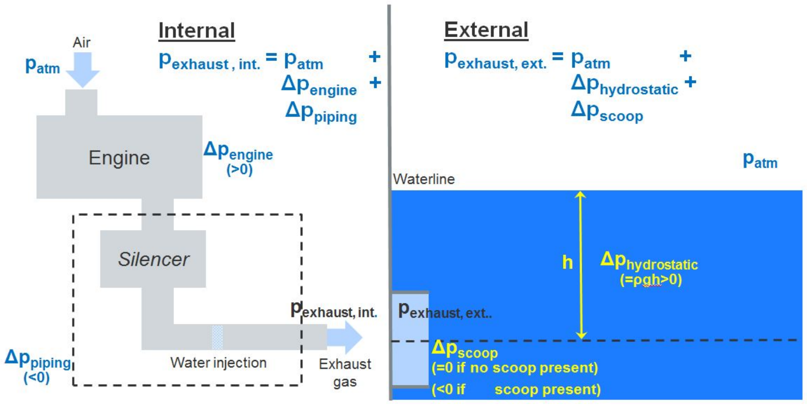

Figure 3.1: Internal and external components of the exhaust system

Figure 3.1 shows the schematic diagram of the underwater exhaust system and the different sources of pressure loss associated with each component. Primarily, the system could be divided into two sections namely the internal exhaust system and the external exhaust system.

The exhaust piping laid out between the engine and the hull can be described as the internal exhaust system. It mainly consists of the bellows, exhaust silencer, SCR unit and the water injection unit. An external appendage like the scoop attached to the exhaust outlet at the hull can be described as an external exhaust component. One of the early designs of the scoop developed by Feadship is shown in Figure 3.2.

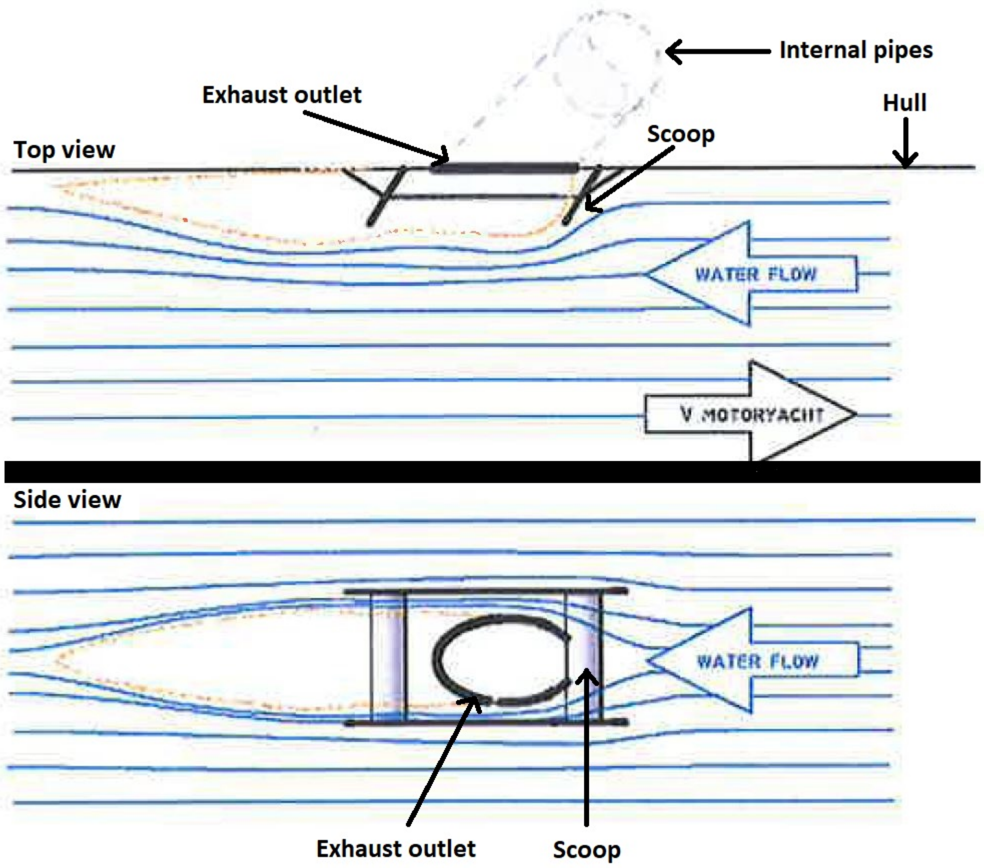

Figure 3.2: Top view and side view of the scoop attached to the side of a hull, [10]

3.1.2. Pressure loss analysis of the exhaust system

Ganzeveld, [10], examined the underwater exhaust system and approximated the pressure loss for the individual components within the system. Also, the impact of the scoop design on the underwater exhaust back-pressure was theoretically analyzed.

Bellows are fitted between the engine and the silencer to absorb the engine vibrations. Since the bellows have a rough surface, the pressure loss is significant in this area. Furthermore, the silencer, the SCR unit and the water injector unit contribute to the major proportion of the overall pressure loss within the internal system. According to previous measurements for Feadship yachts, the above mentioned three components contribute to almost 60% of the pressure loss within the internal system. Furthermore, the bends within the exhaust pipe layout contribute to a small amount of pressure loss. Here most of these components are supplied by external manufacturers and hence there is no possibility for in-house optimization to reduce the pressure loss. However, the exhaust pipe layout has been optimized by adding fewer bends and guide vanes within the bends to reduce flow resistance.

On the external part, absence of the scoop leads to a high back-pressure. If the scoop is present, a low pressure region is created near the outlet due to a large drag force on the scoop structure. This facilitates the smooth flow of the exhaust gas out of the hull. Additionally, the hydrostatic pressure component due to the water column increases the overall pressure at the exhaust outlet. Thus, one of the design requirement for the scoop is that it should be able to counteract the hydrostatic pressure.

The majority of the modern Feadship yachts uses a turbocharged diesel engine. The maximum allowed back-pressure and the permissible limit are listed in the Table 3.1.

Table 3.1: Back-pressure limit for diesel engines used by Feadship

Allowable back-pressure	5000 Pa
Maximum back-pressure	8500 Pa

Also, the pressure loss measurements for the internal exhaust system of a Feadship yacht are presented in Table 3.2. The values shown here present the gauge pressure value. By taking the difference between the back-pressure limit for diesel engine and the available pressure loss values, the pressure requirement in the scoop region can be approximated. Thus, for a functional scoop design, the pressure in the scoop region should be lower than the atmospheric pressure at a given submergence depth of the outlet and a given ship velocity.

Table 3.2: Pressure loss calculation

Quantity	**Pressure loss (Pa)**
Pressure loss between engine and water injector (includes SCR)	3500
Pressure loss between water injector and exhaust outlet	1600
Permissible back-pressure	5000
Pressure in scoop region	-100

To conclude, an analytical approach can provide the approximation for the pressure requirement in the scoop region. For accurate measurements and to improve further understanding of the scoop behaviour, either computational analysis or experimental simulations (like sea trials or model testing) are required, [10].

3.2. Single phase analysis of exhaust scoop

This section reviews the single phase, unsteady analysis of the exhaust scoop carried out by Delvoye, [4], at MARIN. The investigations were done on a 2D domain and a 3D domain with different grid settings and turbulence models on a generic exhaust scoop geometry placed at the bottom of the hull.

3.2.1. 2D Domain

The simplified 2D domain used in the investigation is presented in Figure 3.3. It shows the 2D profile of a generic exhaust scoop geometry placed on the bottomside of the hull. For this investigation, only single phase flow with sea-water was considered and no exhaust flow from the outlet was allowed.

The investigation concluded the need for having sufficient length of the domain in the flow direction to perform simulations for this simplified geometry. Furthermore, two different turbulence models namely $k-\omega$ SST model and the Spalart-Allmaras model were used. It was established that even though the Spalart-Allmaras model takes little calculation time, the $k-\omega$ SST model was more appropriate to model flow separation occurring due to the presence of the scoop.

Albeit the 2D analysis provides a good indication of the pressure distribution around the 2D scoop shape, it fails to predict the possible flow interaction that would take place in a 3D environment. In this analysis, the scoop geometry is constrained within 2D and the flow lacks the freedom to move around the scoop. Also, the entire flow domain would need an extension to avoid the solution being influenced by the boundaries. To conclude, a 2D analysis could be useful to check the grid sensitivity and the impact of turbulence models but it is not useful to analyze a 3D scoop geometry.

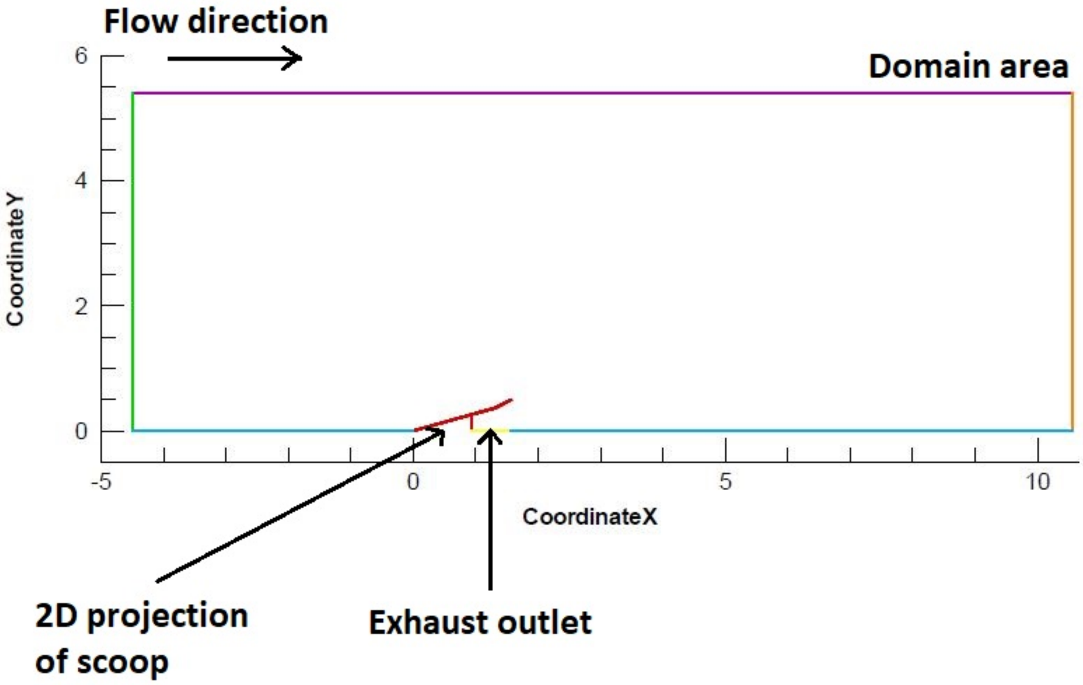

Figure 3.3: 2D Domain, [4]

3.2.2. 3D Domain

A 3D domain used in this investigation is presented in Figure 3.4. Here the hull was represented by a flat plate with the scoop geometry placed on its surface. The free surface was replaced by a slip wall boundary condition.

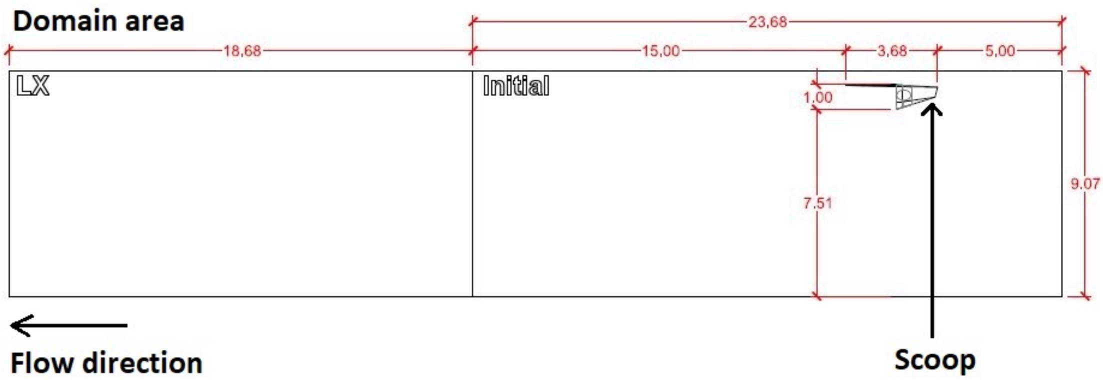

Figure 3.4: 3D Domain, [4]

It was found that the flow behaves very differently around the scoop in a 3D environment compared to that of a 2D domain. Furthermore, the analysis has more resemblance to the real environment around the scoop.

However, even this approach has some major drawbacks. The stated method is useful to determine the resistance offered by the scoop and to determine the pressure difference created due to scoop. But the 2D and 3D cases with an unsteady state approach discussed here do not represent the actual flow scenario at the underwater exhaust outlet. It must be noted that the interaction between two different phases namely exhaust gases and sea water significantly affects the scoop performance.

Apart from the absence of exhaust gas flow in the simulation, the presence of a free surface also affects the results. The geometry of the scoop when placed near the waterline tends to create a local elevation in waves thereby increasing the hydrostatic pressure. Also, the hydrostatic pressure due to the water column was not modelled here. These factors lead to a higher back-pressure than that observed in the above mentioned approach.

To conclude, a 2D approach results in inaccurate values of the pressure distribution. The 3D approach used here is fairly effective to quantify the pressure around the different scoop geometries for comparison purpose, but does not represent the real flow behaviour.

3.3. Multiphase flow

A multiphase flow is defined as a flow in which more than one phase (i.e., gas, solid and liquid) occurs. With respect to the present study, we will deal with the gas-liquid type of multiphase flow. This type of flow can further be classified into different types of interfacial distribution, commonly called flow regimes, [12].

Two common type of flow regimes can be observed here i.e. stratified flow and dispersed bubble flow. When the two phases are separated from each other by a continuous interface, it is described as a stratified flow, [8]. Such a flow is dominated by gravity force, which causes the liquid to stratify at the bottom. Examples of such a flow are oil on water and a free surface flow. Bubble flow is defined as a two-phase flow where small bubbles are dispersed or suspended as discrete substances in a liquid continuum, [15]. Examples of such a flow are raindrops through air and transportation of particles in a flow.

In the current study, the free surface acts as the stratified flow regime with air and sea-water as the two separate phases. The exhaust gas in the sea-water acts as the dispersed bubble flow. The two flow regimes are shown in Figure 3.5.

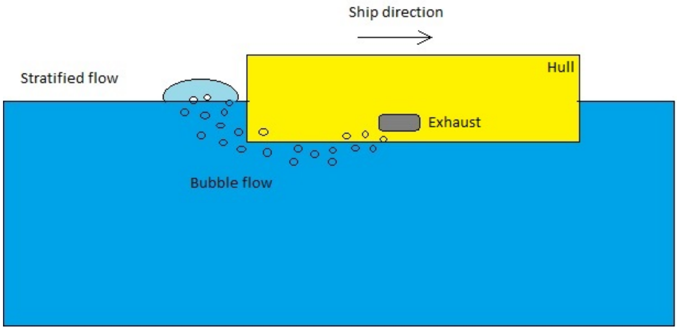

Figure 3.5: Multiphase flow regimes around underwater exhaust system

3.3.1. Bubble flow

Ideally, the exhaust gas (without water injection) flowing out of the underwater outlet in sea-water would behave as the bubble flow. Depending on the interactions between the two interfaces, bubble flow is classified into four different flow regimes, [15]. The different flow regimes are shown in Figure 3.6.

- Ideally-separated bubble flow - There are no direct or indirect interaction between the bubbles in this type of flow. Thus, they behave like single bubbles.
- Interacting bubble flow - In this type of flow, bubble number density becomes so large that the bubbles begin to interact with each other directly or indirectly due to collisions or the effects of wakes caused by other bubbles.
- Churn turbulent bubble flow - With a further increase in bubble number density, the bubbles tend to coalesce to form so-called cap bubbles in this type of flow. There are many interactions between bubble motions and the turbulent flow in this flow type.
- Clustered bubble flow - Here large bubbles cluster and behave as a gas slug, these slugs can merge even further or separate into individual bubbles.

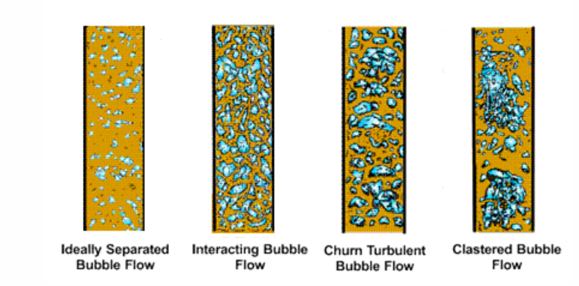

Figure 3.6: Types of bubble flow regime, [15]

However, the focus of the current study would be on the slug flow behaviour of the exhaust mixture. This is due to the reason that an ideally separated bubble flow is difficult to model computationally in case of a full scale yacht geometry. Furthermore, the exhaust mixture (exhaust gas with injected water) flowing out of the underwater outlet are separated by a clear interface and behaves as a slug flow.

3.4. Application of multiphase model

The exhaust gas flow from the underwater outlet is characterized by the presence of water vapour and liquid, [27]. To model such behaviour, a possible approach using a multiphase flow model is discussed here. First, a simplified case for a turbulent jet through a nozzle is described to understand the working of multiphase models. Finally, the case including the plume of exhaust gas for a submarine is discussed to check the limitations of the multiphase model.

3.4.1. Turbulent jet flow

Turbulent jet through a single nozzle can be considered as a simplified form of the exhaust flow from an underwater outlet. A detailed study on this topic has been carried out by Klapwijk, [16]. As shown in Figure 3.7, a buoyant jet was modelled in 3D in a cylindrical tank and a multiphase flow model was used to simulate the turbulent jet. Multiphase modelling will allow solving the continuity equation separately for the liquid and gas phase thereby allowing separate modelling for dynamics and thermodynamics of the liquid and gas phases, [18]. A number of parameters like the grid size, density and the volume flow of the gas was varied to check their respective effects alongside testing different turbulence models.

It was found that for an exhaust gas jet, the system is driven by buoyancy. Furthermore, it is absolutely necessary to have a complete 3D model to accurately model the plume of the exhaust gas. Apart from a 3D geometry, it is necessary to have a fine grid with sufficient refinement to capture the air pockets within the flow, [19]. Also, since the simulation is unsteady, the system should be simulated for a sufficiently long time.

Additionally, it is noted that the choice of turbulence model affects the result significantly. It was observed that the conventional turbulence models have little effect on the spread and surface elevation, but it strongly affected the distribution of the exhaust plume.

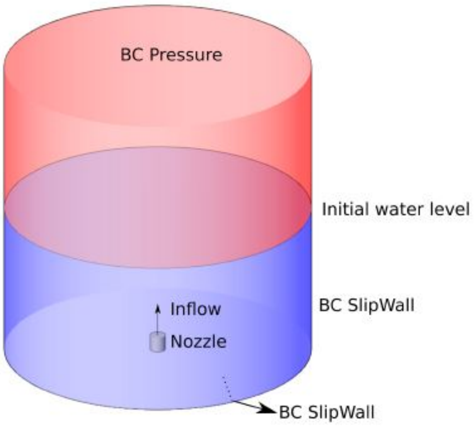

Figure 3.7: Flow domain for the turbulent jet, [16]

3.4.2. Modelling exhaust flow for submarines

Klapwijk, [16] modelled the plume of exhaust gas for the underwater exhaust system of a submarine. Several simplifications were considered for the simulation like only the sail of the submarine was considered to reduce the computational time and the investigation was carried out only for still water i.e. no waves on the free surface were considered. The simplified flow domain is shown in Figure 3.8

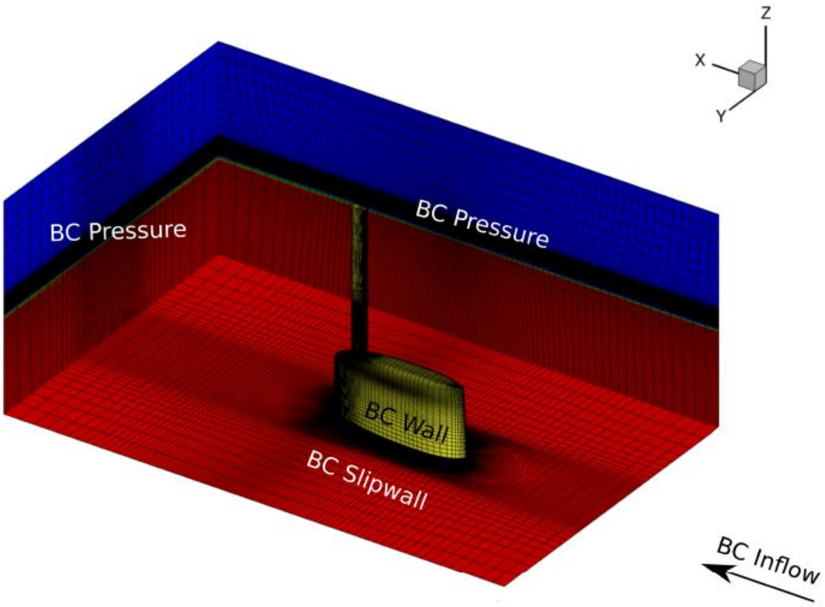

Figure 3.8: Flow domain for the submarine simulation, [16]

The results obtained were able to successfully capture the plume of exhaust gas rising from the submarine sail but the solution lacked the proper convergence near the exhaust. Although this can be improved with the use of a smaller time step, the calculation time required was not feasible. Based on the results obtained, incorporating the multiphase flow method to model underwater exhaust of submarines can lead to the an uncertainty in the order of 15 - 20%. It must be noted that no study into the design of the exhaust outlet was performed in this work.

To conclude, the mutliphase model can be combined with the approach presented by Delvoye, [4], in a 3D domain for designing scoops for underwater exhaust outlets. Nonetheless, care should be taken with respect to the grid size and the use of turbulence models. Additionally, the numerical model to be used should be validated against the existing scoop design to check for uncertainties and possibilities for improvement.

3.5. Effect of sea-trial conditions on model validation

This section reviews the impact of the sea-trial conditions on the validation of the numerical model. The data required for validation will be obtained from sea trials of Feadship yachts. Several factors like tidal currents, wind speed and water depth influence the data measurements at the sea-trials. On the other hand, computational models are prepared assuming a specific sea state or recreate identical situations as that of sea trials. Consequently, the scoop design for underwater exhaust outlet will be analyzed based on those computational models. Neglecting the influence of the above mentioned factors can lead to significant discrepancies between measurements and numerical data, [2].

3.5.1. Wind effect

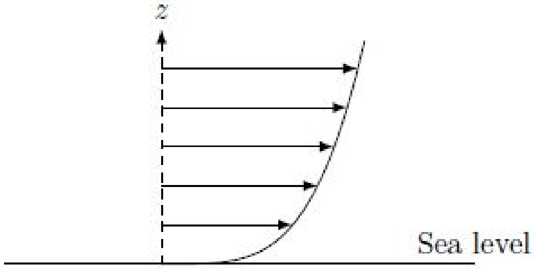

Figure 3.9: Velocity profile near sea surface [2]

The velocity of the wind depends on the altitude. The sea-water surface experiences zero velocity while the absolute wind velocity measured in a far-field area is relatively high. The wind velocity profile can be observed in Figure 3.9. Apparent wind perceived on the main deck of a ship moving at forward speed is different from absolute wind measured on the ground. The prime consequence of the wind effect is that the apparent wind measured on the ship is different at the top of the mast than close to the sea-level. Thus, appropriate corrections need to be applied to the measured data depending on the wind measurement location.

3.5.2. Shallow water effect

Two kinds of waves are produced from the bow and the stern of the ship namely transverse waves and divergent waves. Transverse waves travel in the direction of the ship while the divergent waves propagate away from the hull as seen in Figure 3.10, [2]. These waves are responsible for the wake region behind the hull. Additionally, the increases in wave height increases the hydrostatic pressure over the underwater exhaust outlet.

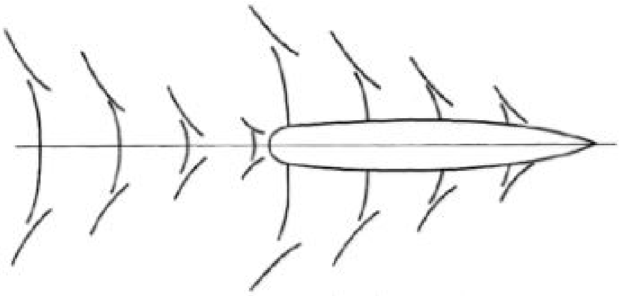

Figure 3.10: Wave formation due to bow and stern

A shallow water depth increases the back-flow in the wake and the flow speed of the water between the sea-bed and the wetted surface of the hull. This leads to a reduction in the pressure between the sea-bed and the hull pulling the hull downwards. Such a situation can increase the submergence depth of the underwater exhaust outlet compared to the design depth. Thus, the submergence depth should be checked thoroughly during the computational analysis to match the conditions of the sea-trials.

To conclude, caution needs to be exercised while measuring the required parameters during the sea trials with respect to the weather conditions (tidal currents, waves). In order to validate the computational model and reduce the experimental uncertainty, care should be taken while providing the input data with regards to the sea state.

4

Back-pressure Calculation and Solver Settings

This chapter presents the method to calculate the back-pressure for the underwater exhaust system. Furthermore, the chapter describes the solver setting used in the CFD simulation. The chapter ends with the description of the validation method.

4.1. Back-pressure calculation method

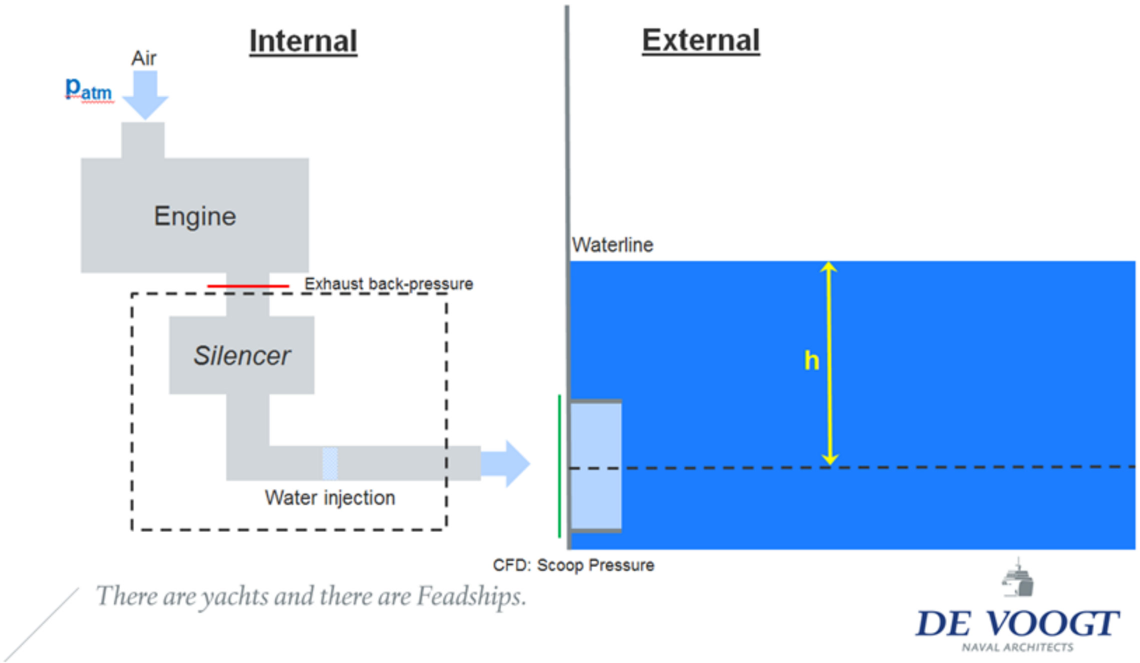

Figure 4.1: Division of underwater exhaust system

Figure 4.1 presents the simplified diagram of the underwater exhaust system. The exhaust back-pressure is measured at the exit of the engine exhaust outlet shown with the red line.

To calculate the exhaust back-pressure (at red line), (i) internal pressure losses of the exhaust system which includes the after-treatment systems and the exhaust pipes (shown within the dashed box) and (ii) the pressure at the scoop region is required (shown with green line).

The internal pressure losses are calculated analytically for the individual components of the exhaust system (inside the dashed box). In this thesis project, value for the total internal pressure loss taken into consideration is $5060\ Pa$. This value is based on the exhaust system of Feadship A which is shown in Chapter 5. This value for the total internal pressure loss will be kept constant throughout the research.

The pressure in the scoop region (at green line) will be measured from the CFD simulation. It should be noted that this value includes the hydrostatic pressure due to water column and the kinetic head due to water flow. Hence, no separate correction is required.

Now, if we consider the system presented in Figure 4.1 as a simple pipe flow problem then,

$$P_B = \Delta P + P_{scoop}.$$

Here, P_B is the exhaust back-pressure, ΔP is the total internal pressure lose in the exhaust system and P_{scoop} is the pressure in the scoop region from the CFD simulation.

This calculated value of the exhaust back-pressure is compared with the values provided by the engine manufacturer in Table 3.1. For safe-working of the diesel engine, the value of P_B should be less than the maximum back-pressure mentioned in Table 3.1.

It must be noted that for different yachts, the after-treatment systems and pipe layout may vary. Thus, it is advisable to calculate the total internal pressure loss for each yacht separately rather than generalizing to get accurate back-pressure values.

4.2. Solver settings

Star-CCM+ provides multiple flow solvers that address different categories of fluid flow. These solvers include a viscous flow solver, a segregated flow solver and a coupled flow solver, [34]. The different types of flow solvers are discussed in Section 4.2.1. Furthermore, it is necessary to choose a proper time-step for the simulation in order to reduce the temporal discretization error. The formulation of a dynamic time-step condition is shown in Section 4.2.2.

4.2.1. Flow solver

The viscous flow solver is only available for laminar flow. Thus, it will not be applicable for the current study.

With the coupled solver, the conservation equations for continuity, momentum, energy, and species are solved in a coupled manner, that is, they are solved simultaneously as a vector of equations. The velocity field is obtained from the momentum equations. From the continuity equation, the pressure is calculated and the density is evaluated from the equation of state, [34].

The segregated flow solver solves the integral conservation equations of mass and momentum in a sequential manner. The non-linear governing equations are solved iteratively one after the other for the solution variables such as velocity components and pressure. The segregated solver is applicable for constant-density flows. Although it can handle mildly compressible flows and low Rayleigh number natural convection, it is not suitable for shock-capturing, high Mach number, and high Rayleigh number applications.

In the current study, the flow around the hull is incompressible with an extremely low Mach number. Thus, a segregated flow solver along with an unsteady implicit time stepping model is a suitable choice for such a simulation. The option for using the coupled flow solver also exists but this model requires relatively large computational resources.

4.2.2. Simulation time-step

In order to decide upon a suitable time-step for the unsteady implicit time model, a new variable called time per flow-past (Tfp) is defined as shown in equation 4.1.

$$Time\,per\,flow\text{-}past\ (Tfp) = \frac{Length\,of\,the\,body}{Flow\,velocity}. \tag{4.1}$$

Here, the length of the body is taken as the diameter of the underwater exhaust outlet. Additionally, the user needs to provide the number of flow-past (Nfp) and the number of time-steps per flow-past (Ntfp). Based on these inputs, the simulation time-step and the simulation physical time can be calculated as per below equation:

$$Simulation\,time\text{-}step = \frac{Tfp}{Ntfp}, \tag{4.2}$$

$$Simulation\,physical\,time = Tfp\ \times Nfp. \tag{4.3}$$

Additionally, a time-step condition is implemented in the beginning to develop a good initial solution, thereby helping the solution to converge.

4.3. Ramp condition for the mass flow rate

In order to replicate the real condition for the release of the exhaust mixture from the underwater outlet, a ramp condition is applied to the mass flow inlet boundary condition. This condition allows the gradual increase in the mass flow rate of the exhaust mixture with the increase in flow-past. The condition is defined as shown in equation

```
IF $Cfp < 10$
    $MFR = (Cfp/10) \times Total\,MFR$
ELSE
    $MFR = Total\,MFR$
END
```

Here, Cfp stands for the current flow-past and MFR represents mass flow rate of exhaust mixture. This argument will allow gradual increase in the mass flow rate of the exhaust gas mixture for initial ten flow-past. After the tenth flow-past, the total mass flow rate is applied to the boundary condition.

4.4. Validation method

To validate the results, the method described by Rijpkema and Vaz, [28], will be used. The procedure described here compares two quantities: The validation uncertainty

$$U_{val} = \sqrt{U_{\phi}^2 + U_{inp}^2 + U_{exp}^2}\,, \tag{4.4}$$

and the validation comparison error

$$E = \phi_i - \phi_{exp}. \tag{4.5}$$

Here, U_{ϕ} is the numerical uncertainty which depends on the apparent convergence condition and the apparent order of convergence, [7]. U_{inp} is the parameter uncertainty related to the fluid properties, flow geometry and boundary conditions. U_{exp} is the experimental uncertainty. Also, ϕ_i represents the arbitrary flow quantity obtained from CFD and ϕ_{exp} represents the experimental value.

In order to check the validation, the following conditions are checked:

- If $|E| > U_{val}$, the comparison error is probably dominated by the modelling error.
- If $|E| < U_{val}$, the modelling error is within the range imposed by the three uncertainties.

This could mean two things: if E is considered sufficiently small, the model and its solution are validated against the given experiment; else the quality of the numerical solution and/or the experiment should be improved before conclusions can be drawn about the adequacy of the numerical model, [28]. However, if the validation is successful, it cannot be said that the numerical model is validated but only that the model is valid for that specific problem.

5

Model Validation

This chapter discusses the validation case for the numerical model. The first section describes the sea-trials of the Feadship yacht. The next section presents the computational domain and mesh. Lastly, the numerical results are validated against the data obtained from the sea-trials of the yacht.

5.1. Sea-trials for Feadship yacht

Feadship A is equipped with four diesel engine - two on the starboard side and two on the portside. The underwater exhaust system has one underwater outlet for each diesel engine. The sea-trials for Feadship A were performed to investigate the reasons for hull fouling. These trials were performed at Tivat, Montenegro by Lloyd's Register Technical Investigation Department (TID) on behalf of De Voogt Naval Architects B.V. (The name of the yacht is not disclosed due to the confidentiality reasons.)

5.1.1. Sea-trial description

All sea trials for Feadship A were conducted in the open sea approximately 10 kilometers west of Tivat, Montenegro. The water depth was more than 100 meter for the duration of the trial. The trials were conducted with wind speeds no higher than 17 knots and with sea waves having a significant wave height of less than 0.3 meter in the direction opposite to the sailing. The average temperatures of air and sea were 18^oC and 18^oC respectively. Figure 5.1 shows the typical sea-state during the sea-trial.

Figure 5.1: Sea-state during sea-trial

To explore the hydrodynamic effects, such as the development of the vessel's wave pattern in relation to the exhaust outlet position, as well as smoke emissions and overall performance of the engines, a series of reciprocal speed power trials were conducted over a number of speeds.

The vessel was loaded to its maximum draught, and to maintain zero heel, fuel was transferred between tanks. The maximum draught was selected for the trials as it results in the highest possible engine loading and largest hydrostatic head, resulting in expected maximum operational back pressure for each speed. The measured operational back pressures are evaluated in this report against the recommended maximum, 5000 Pa, and absolute maximum, 8500 Pa, as specified by the engine manufacturer.

The development of the vessel's wave profile through the speed range was recorded on both the port and starboard side of the vessel, with particular attention to the engine exhausts and the fin stabilizers locations. The reciprocal runs were conducted for each speed-power setting over the same track. This not only allows for subsequent speed correction towards ideal conditions (no wind and waves) afterwards, but more importantly, provides a balanced insight in the engine performance.

5.1.2. Instrumentation for Sea-trials

Pressure transducers with a range of zero to one atmosphere were installed to measure the engine exhaust back-pressures. The location was downstream from the turbocharger and before gas entry into the silencer.

Before the trials, the transducers were calibrated to ensure a linear output over the operating full scale and additionally to ensure that the sensitivity at the expected measurement range was acceptable and gave a satisfactory output. The transducers were calibrated again on completion of the trials. The sampling rate used during the measurements was 2 kHz.

A grid was installed, both on the port side and the starboard side above the exhausts, to enable measurement of wave elevation and spray. Figure 5.2a shows a sketch of the grid with the relevant dimensions. The vertical lines were aligned with the centre of the each underwater exhausts. Figure 5.2b shows the grid placement on hull.

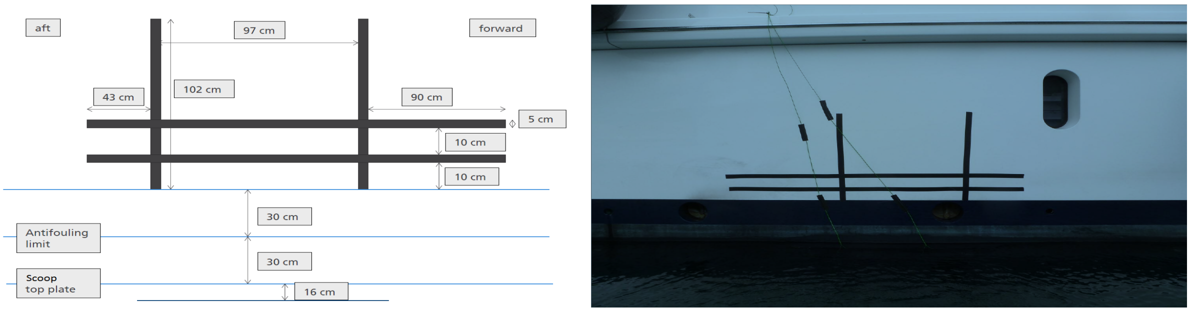

(a) Grid arrangement schematics

(b) Grid arrangement on Feadship A

Figure 5.2: Grid arrangement

The vessel's performance will be influenced by the environmental conditions. In order to correct for these, observations were made for wave height, period and direction of both sea and swell waves. In addition, the relative wind speed and direction was logged using the on-board equipment. During the trials the weather and sea state were calm and the tidal currents were very low, therefore the need to correct any data due to weather conditions was considered unnecessary.

The output from the pressure transducers, draw-wires and GPS were coupled to the input of a National Instruments data acquisition system and recorded onto a laptop using LabView, Signal Express software. Data analysis was carried out using MATLAB 2013.a and MS Excel.

The results of the sea-trials significant to this research project are discussed in Section 5.3 alongside validating the numerical model.

5.2. CFD simulation for Feadship yacht

The computational domain and the yacht model used in the CFD simulation is described in this section. Several assumptions and simplifications have been made to the numerical model due to the limitation of the computational resources. Their influence will be discussed below in detail.

5.2.1. Modelling assumptions

Ideally, the exact geometry of Feadship A should be used to model the exhaust flow from the underwater outlet. Due to the computational demand for such a simulation, some simplifications have been made to the geometry of Feadship A. Firstly, due to the symmetric body of the yacht, only half of the geometry is considered for the simulation. Additionally, the deck of the yacht is not considered in the geometry since it does not have any impact on the exhaust flow thereby reducing the computation time.

Furthermore, the fin stabilizers on the hull are not modelled on the geometry. There is a possibility that the active control surfaces like stabilizers can affect the flow around the hull thereby affecting the exhaust flow from the underwater outlet. However, from the sea-trials it was observed that the wave profile along the hull is smooth and progressive at higher speeds where the exhaust outlets are becoming exposed. In the zone where the exhaust outlets are situated, the wave profile is relatively flat suggesting that the influence of the stabilizers is minimal.

Finally, the simulation was carried out with a still sea-water condition, so no waves were modelled on the free-surface. In contrast, the sea-trials were performed in calm sea conditions with a wave height of less than 0.3 meter. This restriction in the modelling is due to the limited computational resources. Such a situation would rarely occur at sea, however, there are two reasons for implementing this restriction. First, the height of the exhaust plume from the underwater outlet in still water can be extrapolated for the specific wave behaviour. Secondly, the interaction of the exhaust plume with the hull can be observed clearly in the still water conditions. In case of severe sea state, this is not possible due to the rigorous interaction of waves with the hull.

5.2.2. Computational domain

The computational domain used for the validation is shown in Figure 5.3. The mesh is generated using the trimmer mesh model in Star-CCM+. The trimmed cell mesher provides a robust and efficient method of producing a high-quality grid for both simple and complex mesh generation problems. Additionally, this meshing model provides flexibility in refining the wake regions.

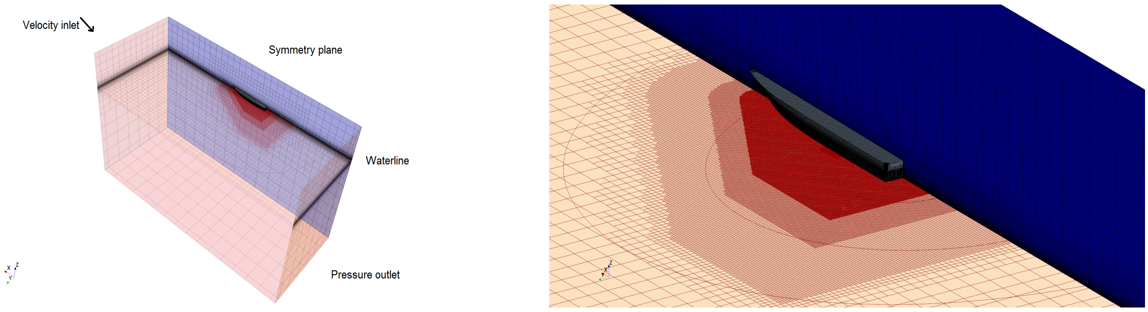

(a) Complete domain (b) Wave refinement area

Figure 5.3: Computational domain

A detailed mesh scene is shown in Figure 5.3b. The free surface region near the hull is refined using a volumetric refinement in three stages. This is essential to capture the wave interaction with the exhaust gas in high detail. Additionally, the mesh uses the anisotropic trimming in the refinement region. This allows to specify a different cell size in the flow direction thereby helping to avoid excessive cell formations in the mesh. The detailed mesh around the underwater exhaust outlet is shown in Figure 5.4.

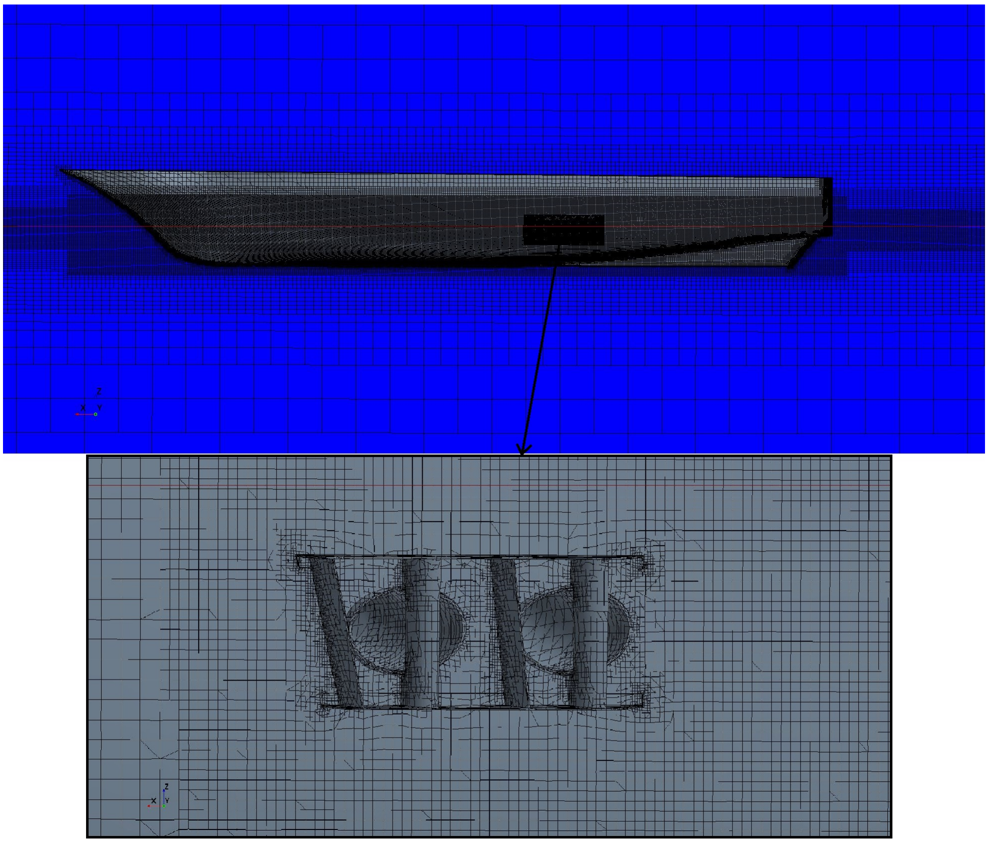

Figure 5.4: Underwater exhaust outlet

A velocity inlet boundary condition has been applied at the inflow, top, bottom and the side surface of the domain. The reason for defining multiple surfaces as velocity inlet is to replicate the motion in sea which moves in all three coordinate axis. In order to avoid any wave reflection from these boundary surfaces, wave damping is introduced to suppress the vertical motion of the wave. A pressure outlet boundary condition is applied at the outflow surface.

The mass flow rate of the exhaust gas is fixed at the inlet of the exhaust pipe by applying a mass flow inlet boundary condition. In order to replicate the real scenario, a ramp condition is applied at the exhaust gas inlet. This condition allows the mass flow rate to start from zero and reach the prescribed mass flow rate value in a specified time.

The no-slip boundary condition is applied to the scoop surface and the hull surface. Furthermore, the required roughness parameters are defined for the hull surface to accurately predict the resistance.

Three different mesh cases were prepared for the model validation. The $y+$ for the fine mesh setup and the coarse mesh setup is shown in Figure 5.5. For good results, the $y+$ value should be kept in the range of 50 to 100, [24]. As observed from Figure 5.5a, $y+$ values are in the range of 50 to 100 in the region under the influence of the waves. The region near the exhaust outlet has $y+$ values lower than 50. For the coarse mesh, the $y+$ values are slightly higher than 100 as seen in Figure 5.5b.

Table 5.1: Mesh data

Mesh type	Number of cells
Coarse	$3.48 \cdot 10^6$
Medium	$6.12 \cdot 10^6$
Fine	$12.74 \cdot 10^6$

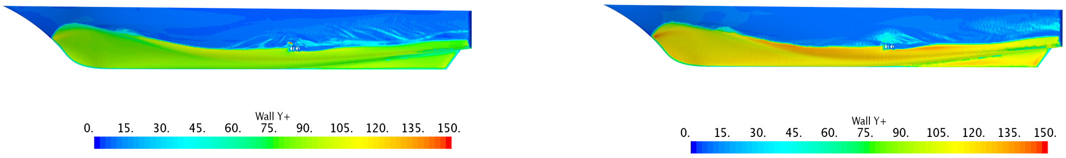

(a) Fine mesh

(b) Coarse mesh

Figure 5.5: $y+$ value for the yacht geometry

5.2.3. Exhaust region refinement

Additional refinement is provided to further improve the solution details around the exhaust outlet region. The effect of the refinement can be clearly observed in Figure 5.6. The refinement was helpful to capture the exhaust spray in detail near the underwater outlet. Without refinement, the maximum elevation of exhaust spray was 47% lower than the same obtained with the refined mesh.

(a) Without refinement (b) With refinement

Figure 5.6: Exhaust spray around underwater outlet

Additionally, the mesh refinement had an impact on how the exhaust flow interacts with the hull after escaping the sea-water. This can be observed from Figure 5.7. Thus, to observe the effect of exhaust spray on the hull contamination, mesh refinement at the exhaust region is necessary.

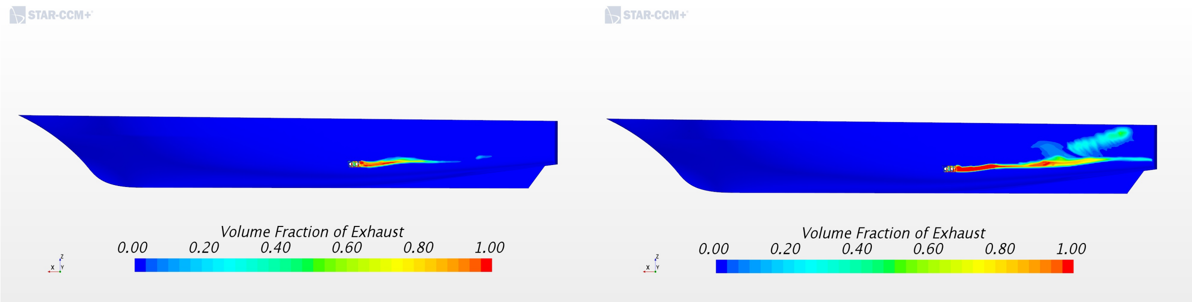

(a) Without refinement (b) With refinement

Figure 5.7: Exhaust spray around the hull

Furthermore, the mesh refinement also impacts the pressure measurement for the underwater outlets. The difference can be observed from Figure 5.8 which shows the back-pressure over time. Without mesh refinement, the peak back-pressure is overestimated by 6% as compared to the same with mesh refinement. The same trend can be seen for the mean back-pressure as well.

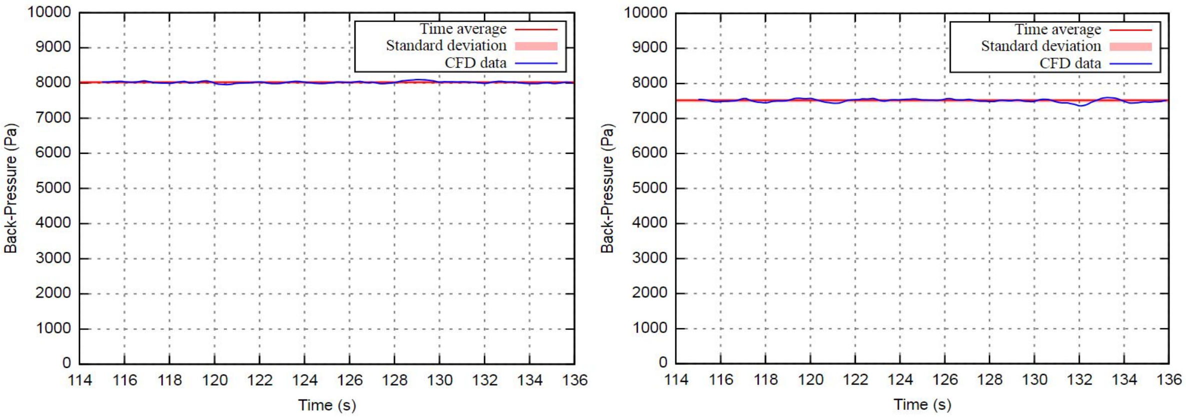

(a) Without refinement (b) With refinement

Figure 5.8: Exhaust back-pressure

These effects can be explained by looking at the variation in cell sizes around the underwater outlet region and the free-surface near those outlets. The smaller cells in the refined region are able to obtain more detailed solution as compared to the large cell size in the mesh without refinement.

5.2.4. Numerical results

All the three types of mesh setup mentioned in Table 5.1 were used for the simulation with exhaust region refinement. The simulation was carried out for the full engine load leading to the maximum mass flow rate of exhaust gas mixture. Here, the exhaust gas mixture comprises of the exhaust gases from the diesel engines and the water/water-vapour released from the water injection unit. The mass flow rate for the exhaust gas mixture was fixed at $42\,kg/s$.

All the simulations were performed for 30 flow-pasts across the hull. The number of flow-pasts determines the simulation time and time-step as explained in Section 4.2.2. To obtain proper convergence, the time-step is reduced to $1/10^{th}$ of the original value during the first flow-past to develop a good initial solution around the hull. Additionally, the mass flow ramp condition allows a slow release of the exhaust mixture. The residuals are shown in Figure 5.9. The sudden increase in the residual quantities after the 200^{th} iteration is due to the increase in time-step as well as the increase in the mass flow rate due to the ramp condition. There is a possibility to continue with the small time-step after the initial flow-past but that would lead to an increased computation time for such a complex geometry. Thus, it is not feasible to continue with small time-step in this study.

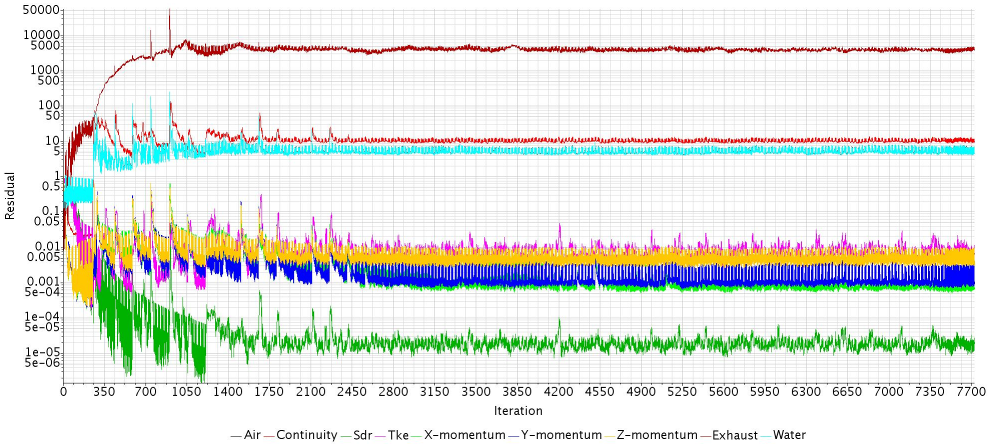

Figure 5.9: Residuals

Also, it should be noted that cells near the hull surface preserve the air phase due to the no-slip boundary condition. This leads to a decrease in the convergence. However, the cells near the underwater outlet lead to a decreased convergence in the entire domain. The phase replacement model is used to replace the air with sea-water in those specific cells.

The exhaust plume from the underwater outlet and its spread around the hull is shown in Figure 5.10. It can be observed here that a trough is formed at the position of the underwater outlet. This trough formation allows only the partial submergence of the exhaust outlet and the scoop. Furthermore, it can be noted that the exhaust plume is restricted near the hull surface due to the high speed flow around the hull. The hull contamination can also be seen near the hull. A possible explanation is the rapid rise of exhaust gases due to the partial submergence of the outlet. Such a situation prevents the exhaust mixture from mixing with the sea-water and facilitates hull contamination. Behind the stern, the wake aids the spread of the exhaust plume away from the hull.

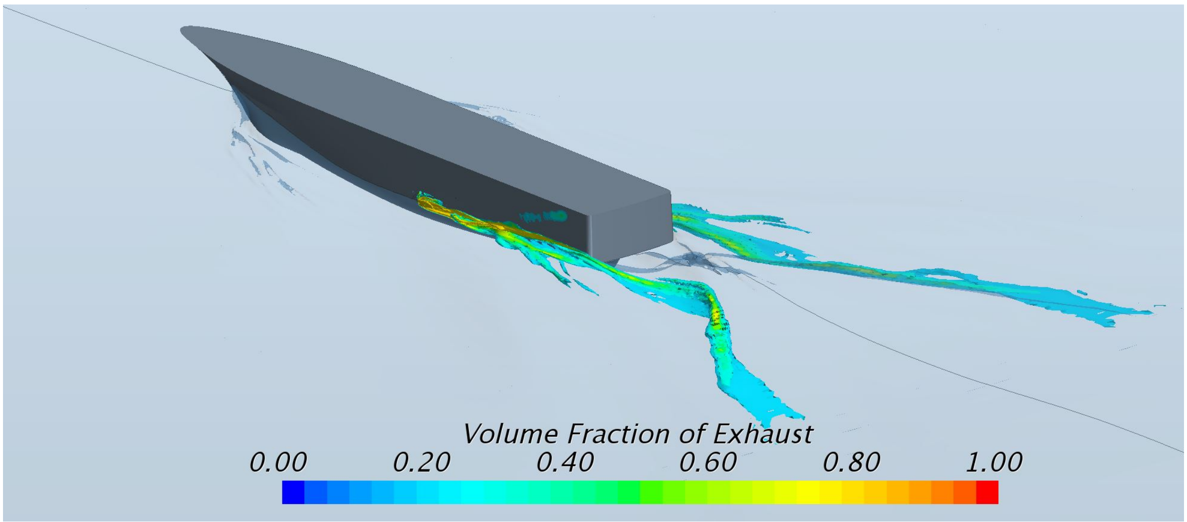

Figure 5.10: Exhaust plume around the hull

Figure 5.11 provides clear details of the spread of the exhaust plume around the hull. The wave height is represented as 'Position in Waterline Transom [Z]' in Figure 5.11. The image shows the spread of the exhaust plume with respect to the wave height around the hull. It can be observed here that the exhaust plumes are carried away from the hull by the rising crest wave. This phenomenon can be seen at two location in Figure 5.11. Near the stern, the transverse waves from the bow deflect a small part of the exhaust plume but the majority of the exhaust mixture is pulled in the wake of the hull. Behind the stern, the crest of the divergent waves from the stern deflects a significant part of the exhaust plume away.

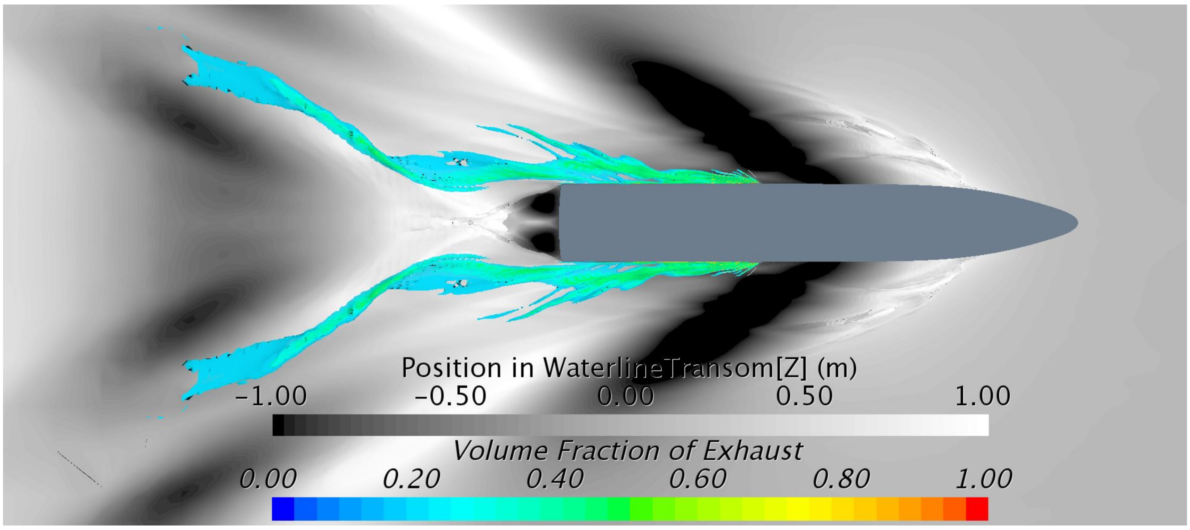

Figure 5.11: Top view of the hull ('Position in Waterline Transom [Z]' refers to wave height)

Furthermore, it is observed that the transverse wave near the stern also facilitates the rise of the exhaust mixture near the hull. This is the probable cause of the hull contamination near the free-surface as observed in Figure 5.7b.

Figure 5.12 presents the exhaust plume from the side view. The exhaust spray is clearly visible from this image. As discussed above, the partial submergence of the scoop is one of the reason for such a spray. The incoming sea-water strikes against the front surface of the scoop generating a splash of water. Additionally, the exiting exhaust mixture from the partially submerged outlet pushes the water away and generates the exhaust spray spanning across the length of the scoop. This explanation can be further verified from Figure 5.13. The average height of the exhaust spray is measured to be 1.7 m from the top of the scoop plate.

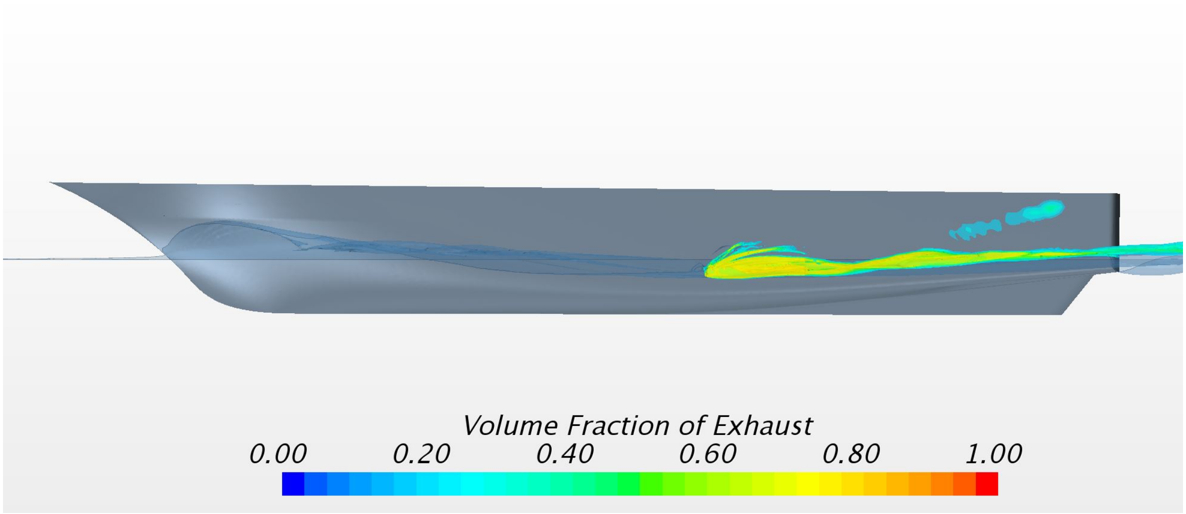

Figure 5.12: Side view of the hull

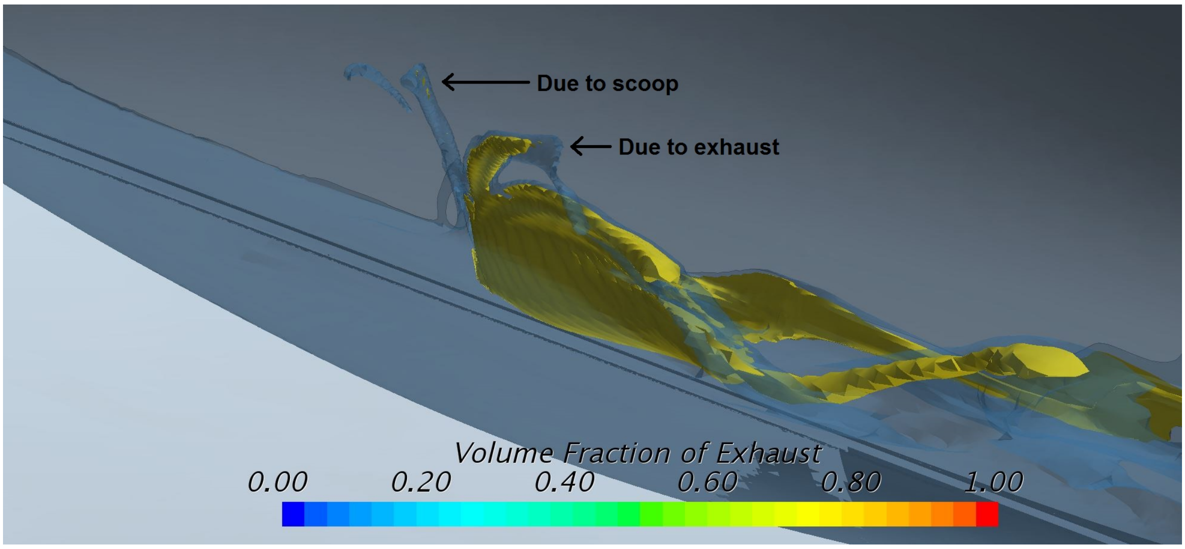

Figure 5.13: Exhaust spray near the underwater outlet

5.3. Validation

Validation of the numerical model is carried out with a qualitative and quantitative approach. For validation, only the results of the sea-trials with the full engine load have been considered in this study. This condition allows all the underwater exhaust outlets to be active. This will also result in the maximum back-pressure produced at the engine exhaust outlet and the maximum height of the exhaust spray generated near the hull.

Furthermore, due to the significant computational expenses for the validation case, simulations are only performed for the different mesh setups.

5.3.1. Qualitative Validation

Qualitative validation is carried out with the images of the wave profile and the exhaust spray captured during the sea-trials.

Figure 5.14 provides a comparison for exhaust spray development at the exhaust outlet on the starboard side for different mesh setups and the sea-trials. As seen from Figure 5.14b, the coarse mesh is able to capture the exhaust spray around the underwater outlet. However, the height of the exhaust spray is under predicted as compared to the sea-trial data. Figure 5.14c shows the exhaust spray from the medium mesh setup. The spray profile is relatively well captured and provides a close estimation of the spray height. Figure 5.14d shows the exhaust spray for the fine mesh setup. It can be observed that the fine mesh provides the most detailed view for the exhaust spray, however the required computation time to obtain these results is significantly high. More discussion on exhaust spray height is provided in Section 5.3.2.

Figure 5.15 illustrates the wave profile along the hull and the exhaust spray from the top view. The wave profile before the exhaust scoop stays relatively flat. The exhaust spray is satisfactorily captured in the CFD simulation as observed in Figure 5.15b. However, upon comparing the CFD results with the exhaust spray data from the sea-trials some discrepancies are observed. This is amongst others, due to the limitation of the multiphase model as this model is not able to capture the fine spray particles.

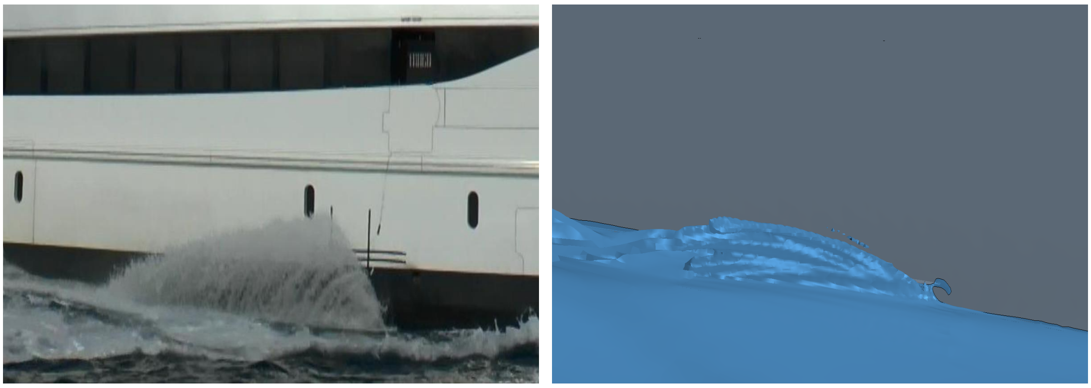

(a) Sea-trial (b) Coarse mesh setup

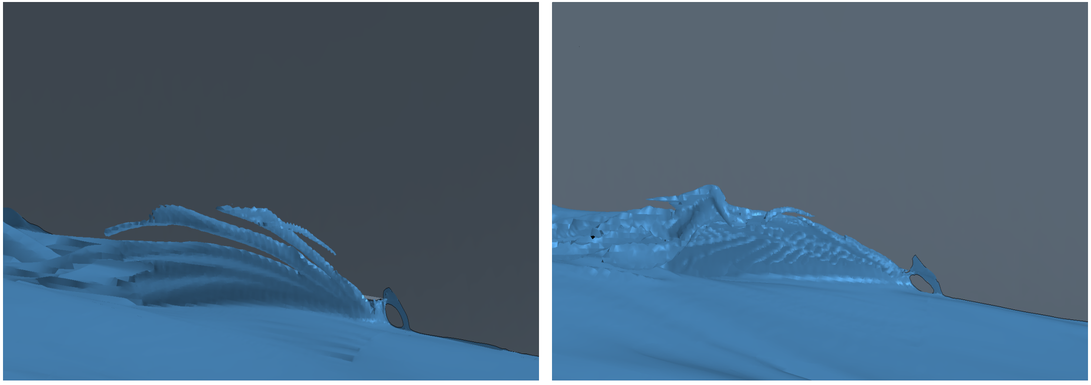

(c) Medium mesh setup (d) Fine mesh setup

Figure 5.14: Exhaust spray from side view

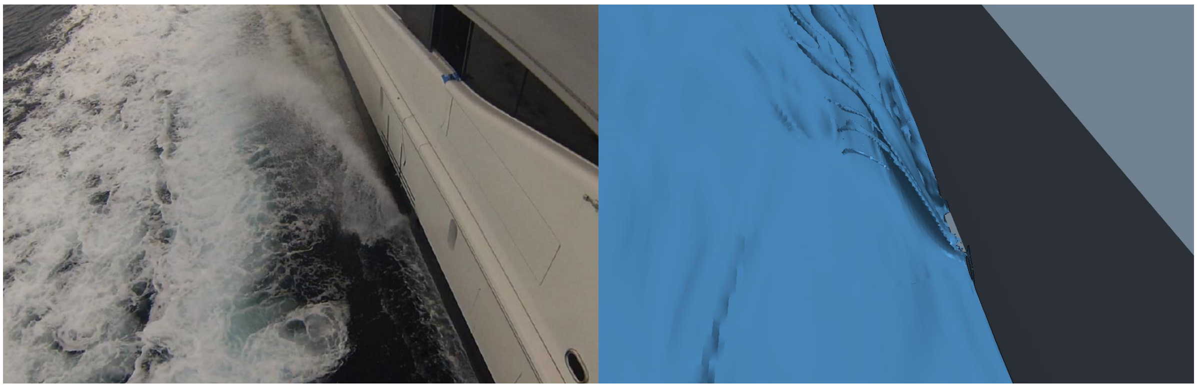

(a) Sea-trial (b) CFD

Figure 5.15: Exhaust spray from top view

Figure 5.16 and Figure 5.17 provide a detailed view of the exhaust spray across the scoop. CFD simulation is able to predict the partial submergence caused by the wave profile near the underwater outlet. As explained in Section 5.2.4, two factors are responsible for the exhaust spray. The water splash over the front surface of the scoop is not clearly captured as seen in Figure 5.15a. The tube of exhaust spray due to the exiting exhaust mixture is relatively well captured in the CFD simulation. Additionally, the CFD simulation gives a relatively good prediction for the depression of the waves behind the scoop and close to the hull caused by the partially submerged outlet as observed from both the figures.

Figure 5.16: Sea-trial: Top view of the scoop

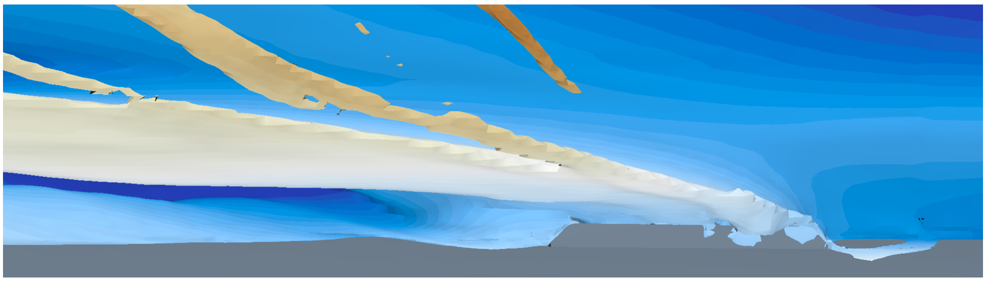

Figure 5.17: CFD: Top view of the scoop

The hull contamination caused due to the escaping exhaust mixture during sea-trial is shown in Figure 5.18. A similar area of hull contamination is obtained from the CFD simulation as shown in Figure 5.19. However, some differences can be observed between both the images. Figure 5.18 was taken post sea-trial and hence no exhaust spray can be observed as compared to the CFD result. Furthermore, the actual Feadship yacht is equipped with a bar like structure on the side of the hull which restricts the assimilation of soot particles to the region below the bar. In contrast, due to the absence of such a structure in the CFD geometry, the exhaust mixture is spread across the rear section of the hull.

Figure 5.18: Sea-trial: Hull contamination

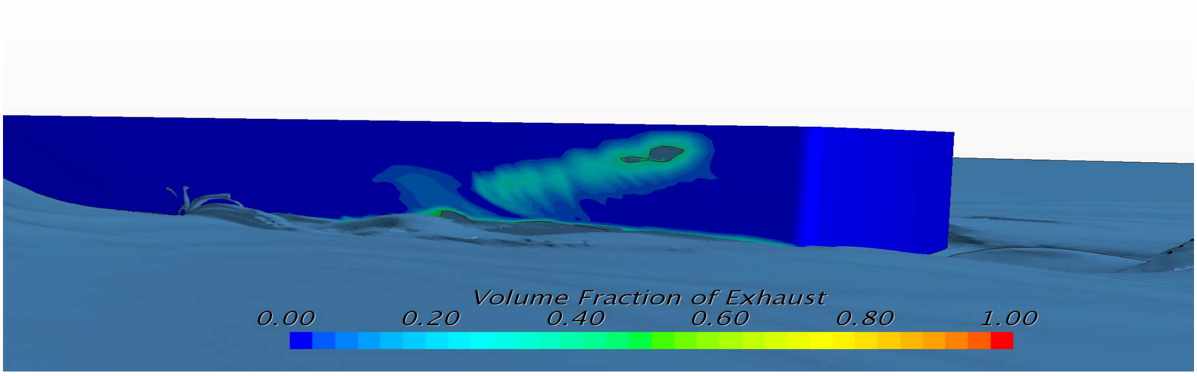

Figure 5.19: CFD: Hull contamination

To conclude, the numerical model provides a good qualitative prediction of the wave profile, the exhaust spray around the hull and the interaction of the exhaust plume with the hull.

5.3.2. Quantitative Validation

A Quantitative validation is carried out by performing a comparison of both the exhaust spray height and the exhaust back-pressure.

Table 5.2: Exhaust spray height for maximum engine load

	Maximum spray height (m)
Sea-trial	1.87
Coarse	1.52
Medium	1.69
Fine	1.78

The height of the exhaust spray during sea-trial was measured as explained in Section 5.1.2. The maximum height of the exhaust spray obtained during sea-trials and for the different mesh setups are mentioned in Table 5.2. The result obtained on the coarse mesh shows an under prediction by 14% compared to that on the fine mesh. With the results obtained here, it cannot be said that a grid independent solution is obtained for the used mesh setups. Keeping in mind the limitation of the computational resources and time, we will assume that a grid independent solution is obtained with the medium mesh setup.

For validation, the comparison error E and the validation error U_{val} are calculated for the three mesh setups. The explanation for both the terms is given in Section 4.4. The comparison error E is calculated by taking the percentage difference of the exhaust spray height obtained from the CFD simulation with that of sea-trial.

Here, we will assume the input uncertainty to be 0% and the experimental uncertainty to be 10%. Furthermore, the numerical uncertainty for the exhaust plume simulation is assumed to be 12%. All these values are taken from the work done by Klapwijk, [16] on the underwater exhaust flow simulations. The value of U_{val} is calculated by taking the square root of the sum of the squares of the above mention values. These results are presented in Table 5.3.

Table 5.3: Validation of exhaust spray height for maximum engine load

	E	U_{val}	Conclusion
Coarse	18.72 %	16.08 %	$E > U_{val}$
Medium	9.63 %	16.08 %	$E < U_{val}$
Fine	4.81 %	16.08 %	$E < U_{val}$

From Table 5.3, it can be concluded that the results for the medium and the fine mesh are within the range imposed by the three uncertainties. However, results can be improved by refining the mesh further and reducing the comparison error E.

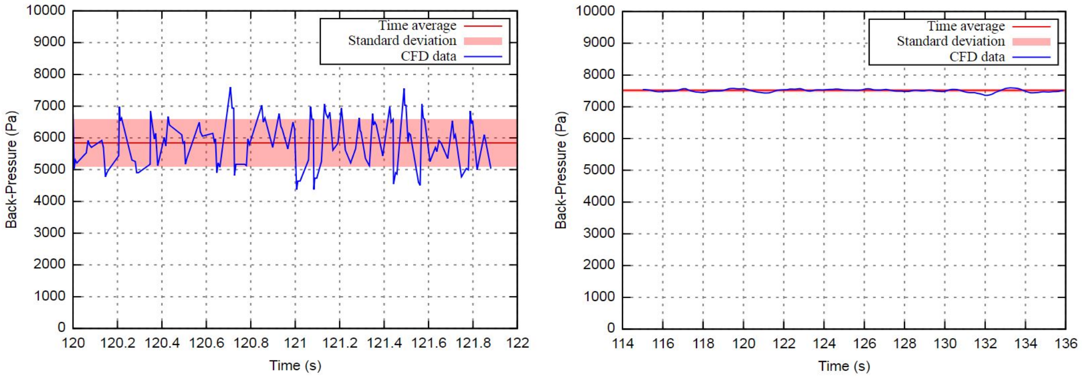

(a) Sea-trial

(b) Medium mesh setup

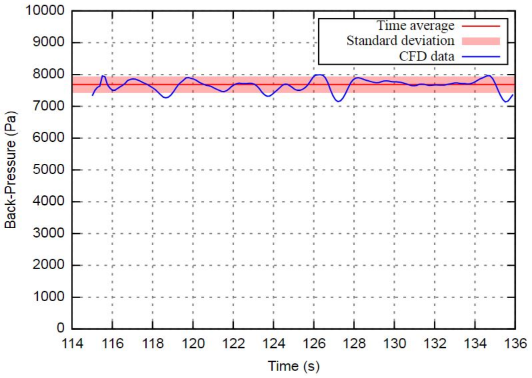

(c) Fine mesh setup

Figure 5.20: Exhaust back-pressure

Figure 5.20 presents the exhaust back-pressure obtained from the sea-trials and the CFD prediction for the starboard engine. It is difficult to directly validate the results of the back-pressure due to the following reasons. Firstly, the effect of the diesel engine is not simulated in the CFD model. Thus, the pulsating behaviour of the back-pressure as observed in Figure 5.20a is not seen in the CFD results. This creates a significant difference in the direct comparison of the mean back-pressure. For both mesh setups, the mean back-pressure is overestimated by 30% as compared to the sea-trial.

Secondly, the numerical uncertainty increases for the back-pressure since the internal pressure losses in the exhaust system are analytically calculated and not modelled in the CFD simulation. Furthermore, there is a complex interaction of the exhaust mixture with the waves at the underwater outlet which makes it difficult to predict the accurate back-pressure.

However, it is possible to compare the peak back-pressure for both scenarios. From Figure 5.20, the peak back-pressure is underestimated by 9% for the medium mesh setup as compared to the sea-trial data. In case of the fine mesh, this difference is reduced to 5%. However, care should be taken in using this approach as it is very dependent on the internal pressure losses in the exhaust system.

To conclude, the results for the height of the exhaust spray have been validated against the data obtained from the sea-trials. Additionally, it is possible to obtain an approximate value with the numerical model for maximum back-pressure prediction.

5.4. Notable observations

This section presents some of the significant observations from the CFD simulations which can be used to better understand and improve the underwater exhaust system.

5.4.1. Interaction between the two outlets

There is an important interaction taking place between the two underwater outlets at the maximum engine load which can impact the exhaust back-pressure at those outlets. Figure 5.21 shows the exhaust back-pressure for the front and the rear underwater outlet.

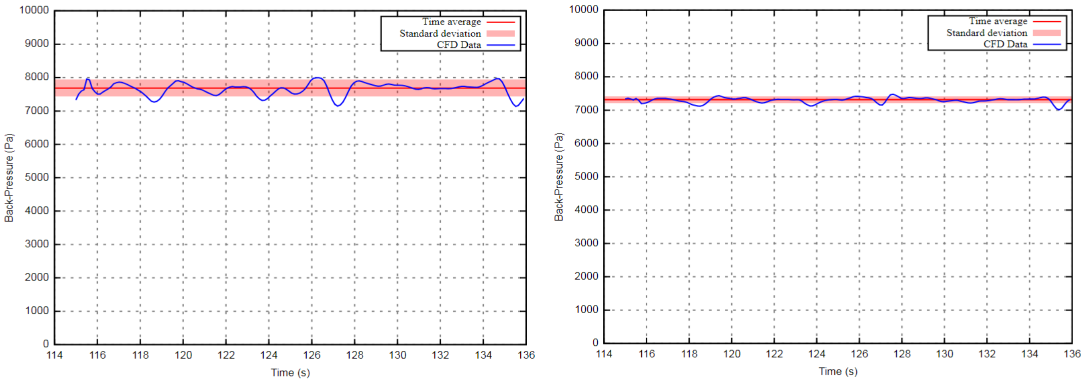

(a) Front outlet

(b) Rear outlet

Figure 5.21: Exhaust back-pressure

From the above images, it was observed that the mean back-pressure in the rear outlet is approximately 5% lower than the same in the front outlet. Furthermore, the maximum back-pressure observed in the rear outlet is approximately 6% lower than the same observed in the front outlet.

This phenomenon can be explained with the help of Figure 5.22. It can be observed here that the exhaust mixture being released from the front outlet comes directly into contact with the surrounding water layer which provides resistance to the exhaust flow. However, the exhaust mixture being released from the rear outlet initially comes into contact with the exhaust mixture from the front outlet. This reduces the resistance offered from the surrounding water layer thereby providing a reduced back-pressure for the rear outlet.

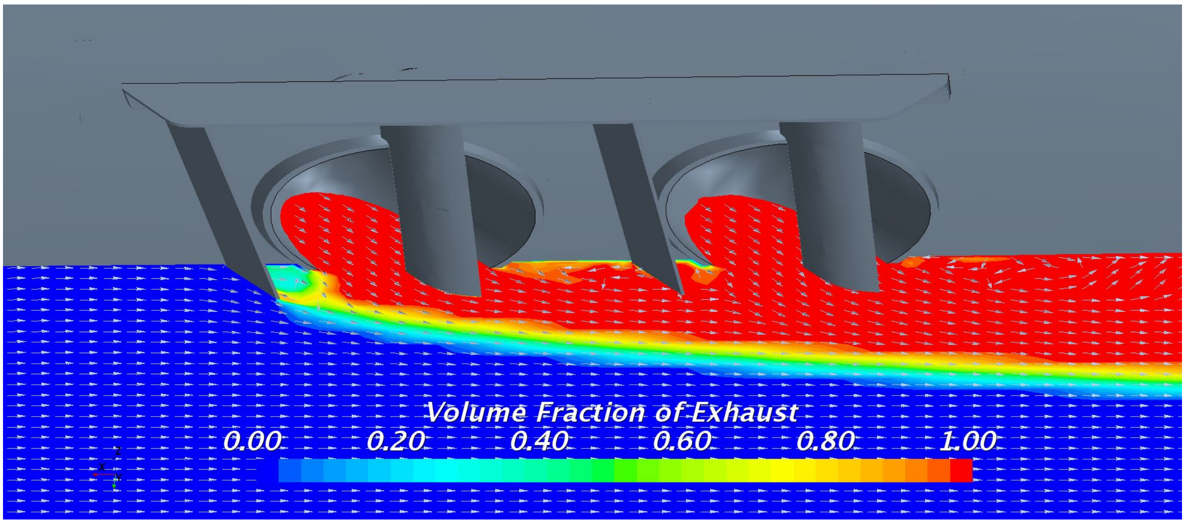

Figure 5.22: Exhaust mixture flow near underwater outlet

5.4.2. Effect of single functioning outlet

Figure 5.23 shows the flow development around the scoop when the front exhaust outlet is turned off. It can be observed that the partially submerged scoop deflects the water away from the rear exhaust outlet. This deflection creates an air gap between the water layer and the rear outlet. This air gap prevents the exhaust gases from mixing with the sea-water, thereby escaping and contaminating the hull. Furthermore, the exhaust back-pressure remains approximately the same for the rear outlet as in the case with both the outlets turned on. This is due to the phenomenon explained in Section 5.4.1; here the exhaust mixture layer is substituted by the air gap.

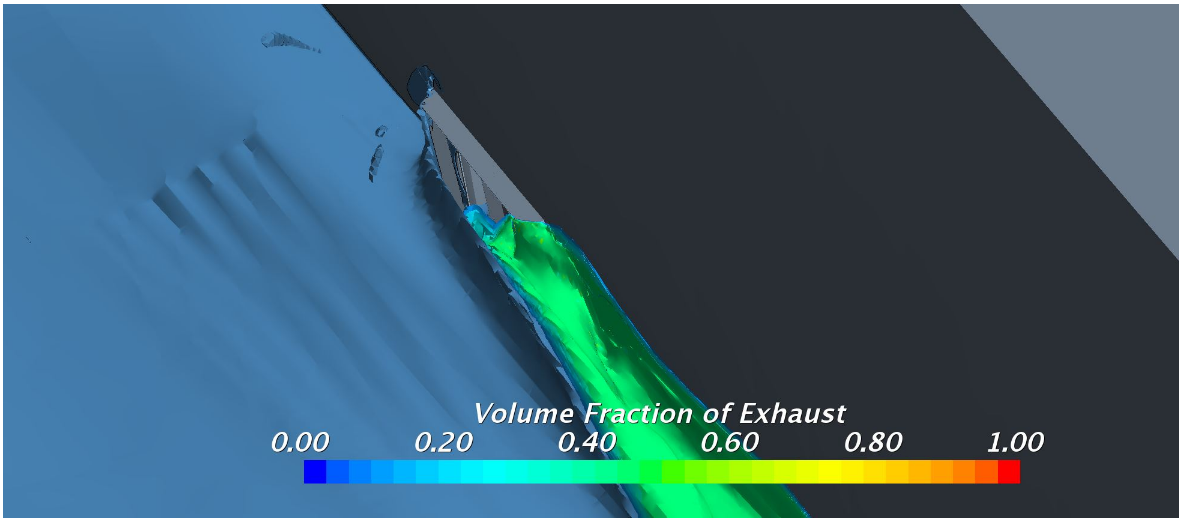

Figure 5.23: Front exhaust off

Figure 5.24 displays the flow development around the scope when the rear exhaust outlet is turned off. The exhaust spray observed here is very similar to that observed when both the outlets are turned on. However, this configuration shows that the front underwater outlet is solely responsible for the generation of exhaust spray. The mechanism of the exhaust spray formation is described in Section 5.2.4.

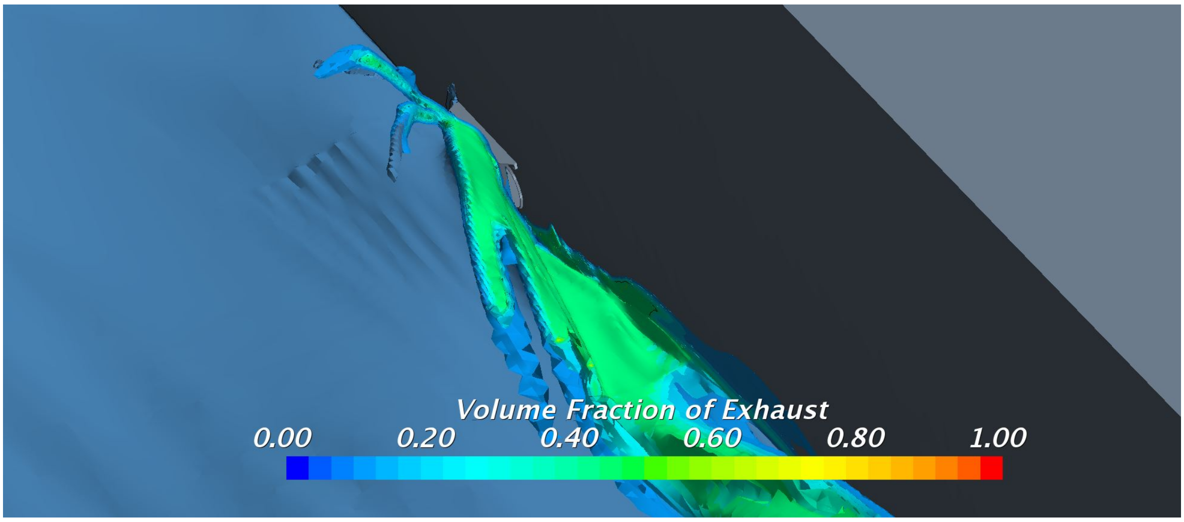

Figure 5.24: Rear exhaust off

Thus, it is evident that the observations described in Section 5.4.1 and Section 5.4.2 can be combined to improve the future design of the underwater outlets. This will be discussed further in the later chapters.

6

Analysis of Baseline Geometries

This chapter describes the baseline study carried out with the two scoop geometries mentioned in the previous chapter. This study is done by varying the yacht velocity for the two different scoop geometries and also the hull without any scoop. Based on the discussion of these results, the design criteria for a new scoop geometry will be decided. Furthermore, the performance criteria for the scoop will be laid out in this chapter.

6.1. Computational setup

The two baseline geometries of scoop are shown in Figures 6.1 and 6.2. These two designs are currently in use by most of the Feadship yachts equipped with the underwater exhaust systems. The effect of different parameters is studied with respect to these two baseline geometries. As seen from Figure 6.1, the scoop geometry 1 features a curved metallic plate surrounding the underwater exhaust outlet. Such a curvature allows the sea-water to flow around the underwater outlet uninterrupted. On contrary, scoop geometry 2 in Figure 6.2 features two vertical deflection plates attached to the horizontal metallic plates on either sides. The front deflection plate redirect the sea-water around the underwater outlet while the second deflection plate redirects the exhaust flow.

The computational domain for the baseline scoop geometries is shown in Figures 6.3 and 6.5. With reference to the diameter (D) of the underwater exhaust outlet, relative dimensions of the computational domain and the refinements are presented in the Table 6.1. For the current study, diameter (D) value is $500\,mm$. The domain presented here will be used to analyze the new scoop geometries in the upcoming chapters.

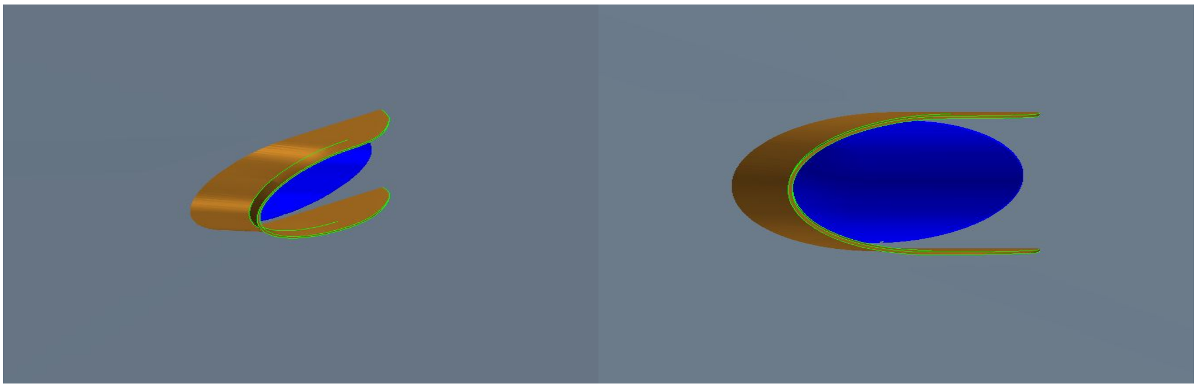

(a) Isometric view

(b) Side view

Figure 6.1: Scoop geometry 1 (grey region - hull; blue region - exhaust outlet; golden region - scoop)

(a) Isometric view (b) Side view

Figure 6.2: Scoop geometry 2 (orange region - hull; violet region - exhaust outlet; white region - scoop)

6.1.1. Domain

The computational domain shown here consist of only a part of the hull in the region of the underwater exhaust outlet as shown in Figure 6.3. The mesh settings and the boundary conditions are kept the same as explained in Section 5.2.2.

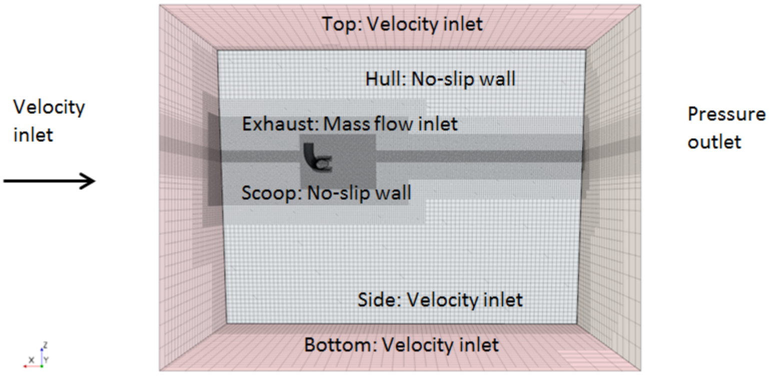

Figure 6.3: Side view - Computational domain with boundary conditions

Table 6.1: Relative dimensions of domain and refinement regions

Volume	Length	Width	Height
Domain	33*D	20*D	26*D
Fine refinement - Exhaust	16*D	7*D	6*D
Coarse refinement - Exhaust	18*D	9*D	8*D
Fine refinement - Free Surface	33*D	20*D	1*D
Medium refinement - Free Surface	33*D	20*D	2*D
Coarse refinement - Free Surface	33*D	20*D	4*D

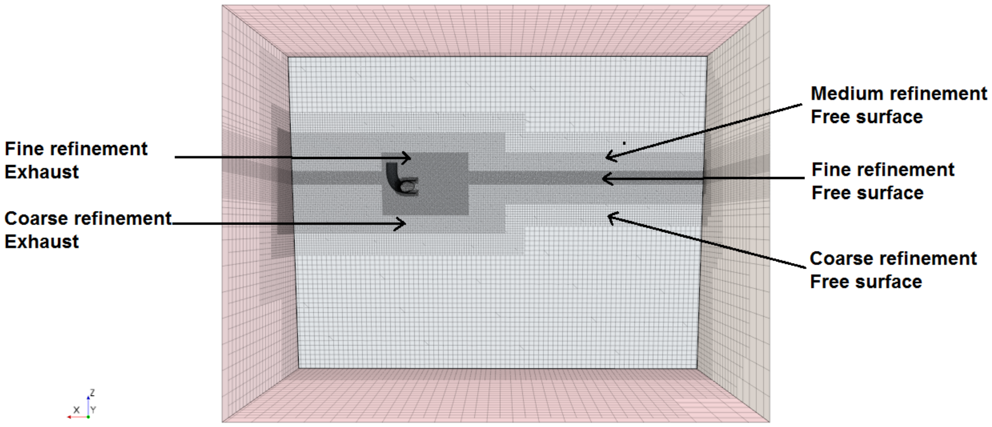

Figure 6.4: Side view - Computational domain with refinement region

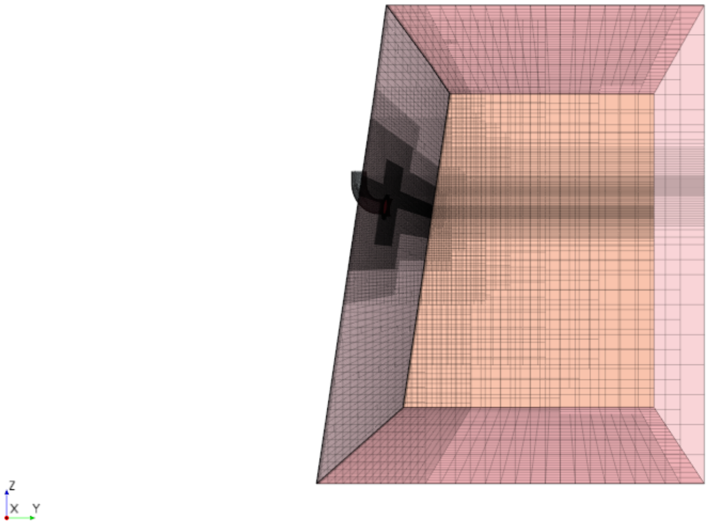

Figure 6.5: Front view - Computational domain

6.1.2. Solver initialization

Before you run the simulation, the solver is initialized in Star-CCM+. For this initialization, the volume fraction of the exhaust gas is kept zero while the volume fraction of the air and the water are set as a function of the VOF model. Furthermore, the pressure in the computational domain is fixed as a hydrostatic pressure function of the VOF model.

Before initializing the velocity in the computational domain, it must be noted that the velocity inside the exhaust pipe stays zero while in the rest of the domain it will be the specified input value. The initialized domain is shown in Figure 6.6.

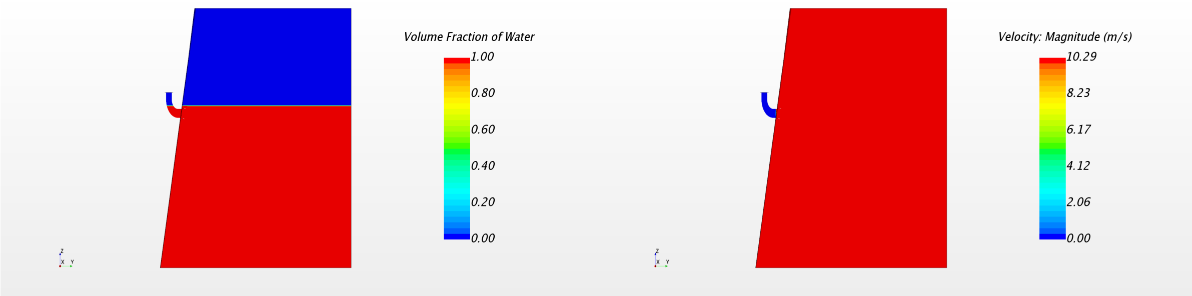

(a) Volume fraction of water (b) Velocity field

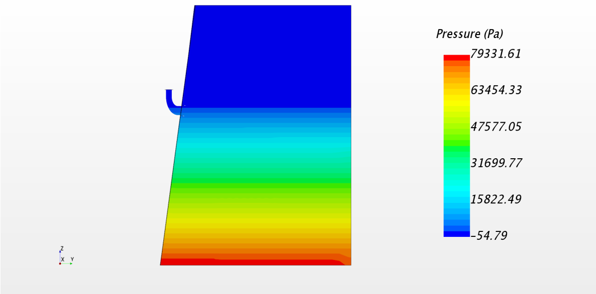

(c) Pressure field

Figure 6.6: Initialized domain

6.2. Observations of CFD simulation

Several different configurations were simulated to investigate the impact of the scoop on the performance of the underwater exhaust system. The observations from these simulations are described in the sections below. Additionally, this investigation would help understand the parameters of significance for the design of a new scoop geometry.

6.2.1. Effect of exhaust gas

Figure 6.7 provides a comparison for the simulation with and without the flow of the exhaust gas. This will help to study the effect of the exhaust gas on the pressure in the scoop region and to show how it shapes the flow around the scoop. The mass flow rate at the exhaust inlet is fixed at zero for the simulation without exhaust gas.

Figure 6.7 shows the pressure in the scoop region (explanation for pressure measurement is provided in Section 4.1 for better understanding). It can be observed from this figure that at the higher velocities the pressure at the underwater outlet is largely under-estimated for the simulation without exhaust gas. Thus, to accurately determine the exhaust back-pressure value, the flow of the exhaust gas is necessary during the simulation.

The reason for this under-estimation is the additional pressure from the exhaust gas. In the absence of the exhaust gas, the scoop interacts only with the water and a pressure difference is created within the single medium. Upon introduction of the exhaust gas, a new medium with an absolute pressure slightly higher than the atmospheric pressure is introduced in the scoop region. Thus, the interaction with this new medium is not able to create a large pressure difference as in the case without the exhaust gas flow.

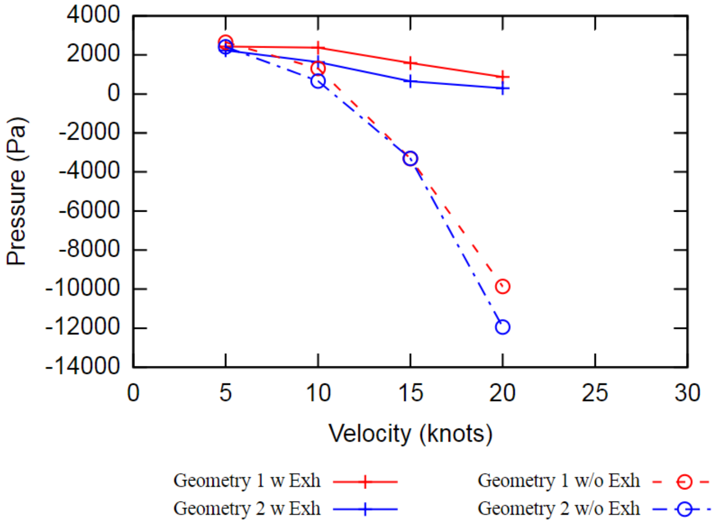

Figure 6.7: Pressure in scoop region

6.2.2. Effect of scoop

In this section, simulations were performed for the underwater exhaust system with and without a scoop attached to the hull. This study will provide a base to compare the effects of different scoop. For the study, simulations were performed at four different yacht velocities. Other parameters, like the density of the exhaust gas, the mass flow rate of the exhaust mixture and the submergence depth of the exhaust outlet were kept constant.

Figure 6.8 shows the back-pressure for the underwater exhaust system with and without a scoop for different yacht velocities. The back-pressure is calculated based on the method described in Chapter 4. The color scheme in the background of the graph represents the permissible and maximum exhaust back-pressure as provided by the engine manufacturer in Table 3.1. The lower limit of the orange zone represents the permissible exhaust back-pressure and the upper limit of the same represents the maximum exhaust back-pressure. This graphical representation will be used throughout the report for presenting the exhaust back-pressure.

As shown in Figure 6.8, the exhaust back-pressure without scoop crosses the maximum back-pressure limit for all simulated velocities. Here, the rise in the back-pressure is caused by an increase of the kinetic head caused by the increase in the hull velocity. The hydrostatic pressure component stays constant due to the fixed submergence depth of the exhaust outlet.

Figure 6.8 clearly shows that both geometries of the scoop significantly reduce the back-pressure. Furthermore, the back-pressure is reduced below the maximum limit with the introduction of a scoop and the performance of the scoop improves with increasing velocity.

To conclude, the presence of the scoop significantly reduces the back-pressure for the underwater exhaust system. Also, to accurately predict the back-pressure value and to check the flow behaviour around the scoop, the flow of the exhaust gas is necessary in the CFD analysis.

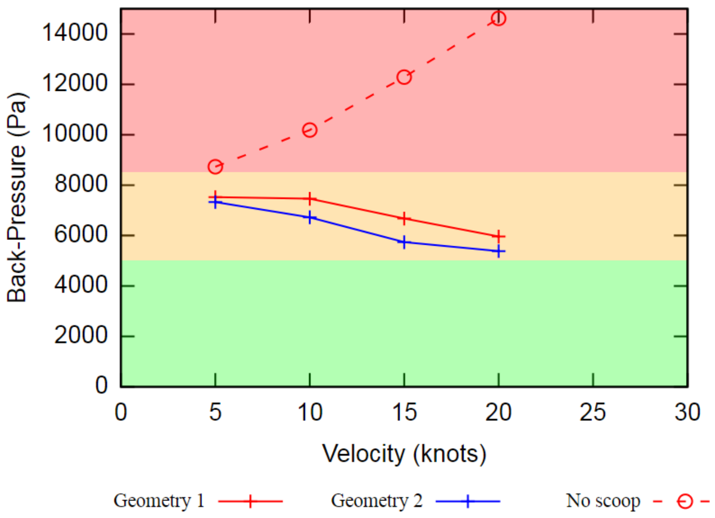

Figure 6.8: Exhaust back-pressure

6.2.3. Resistance of the scoop

From Figure 6.9, it can be seen that the resistance of the scoop increases with increasing velocity. Here, the increase in resistance is inversely proportional to the back-pressure. For high velocities, scoop geometry 2 has a relatively high resistance leading to a lower back-pressure. Thus, a trade-off is necessary between the scoop resistance and the back-pressure for an optimal scoop design.

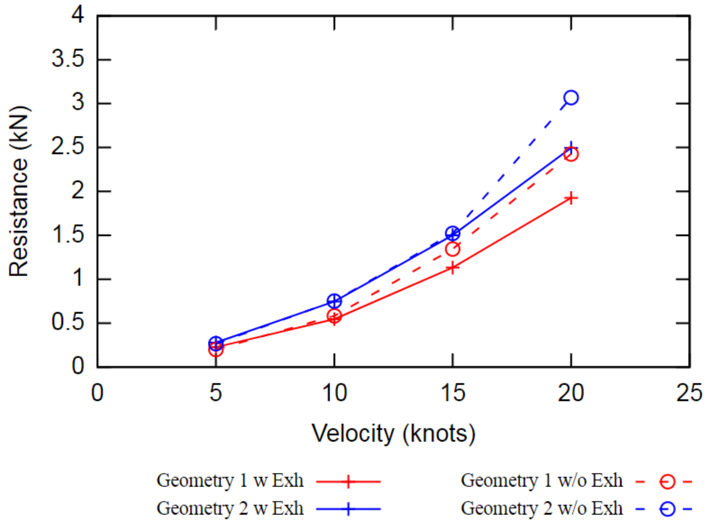

Figure 6.9: Scoop resistance

Furthermore, the flow of the exhaust gas also affects the scoop resistance as can be seen from Figure 6.9. The scoop resistance in presence of an exhaust gas flow is slightly lower compared to that without the exhaust gas flow. This is caused by a reduction in the friction due to a shear and pressure force on the internal surface of the scoop. The friction due to a shear and pressure force is lower in presence of the exhaust gas as compared to the sea-water

6.2.4. Local water elevation above scoop

Figure 6.10 shows the local wave elevation due to the exhaust gas flow near the underwater outlet for different velocities. This measurement is taken above the centre of the exhaust outlet and with respect to the initial waterline on the hull. This elevation of water above the exhaust outlet provides additional hydrostatic pressure, thereby increasing the back-pressure.

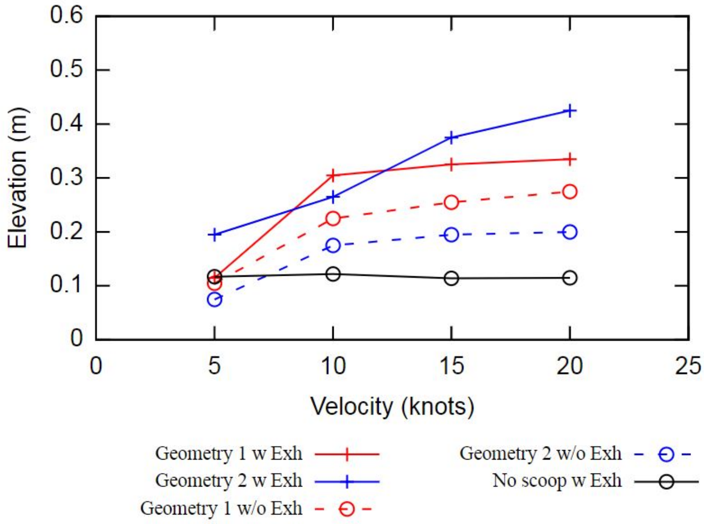

Figure 6.10: Local wave elevation

Apart from the increasing resistance, the local wave elevation also changes depending on the design of the scoop. It can be observed from Figure 6.10 that the elevation is significantly increased with the introduction of a scoop. This additional elevation increases the hydrostatic pressure which results in a higher exhaust back-pressure. Figure 6.11 shows the increase in wave elevation with increasing yacht velocity in absence of an exhaust gas mixture.

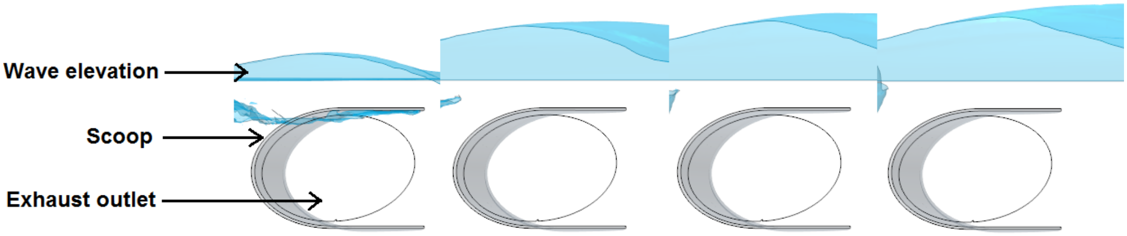

Figure 6.11: Side view - Local wave elevation over scoop geometry 1

Figure 6.10 also shows the effect of the gas flow on the local wave elevation above the scoop surface. Figure 6.12 shows this effect clearly on the scoop Geometry 1. Since a new medium in the form of an exhaust gas is introduced at the outlet, the sea-water surrounding the scoop is displaced. This displacement causes an increase in the local wave elevation. Additionally, the hydrostatic pressure also increases due to the increase in the overall water column above the scoop, thereby increasing the exhaust back-pressure.

However, the impact of the increased wave elevation is not strongly visible on the

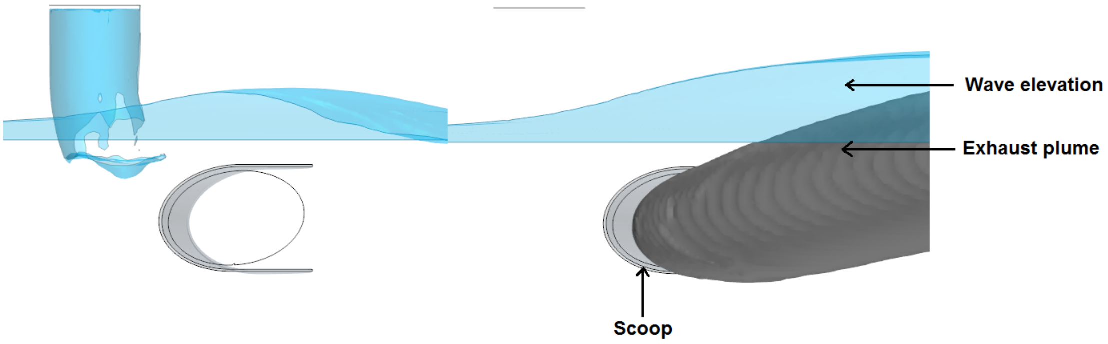

Figure 6.12: Side view - Local wave elevation without (right) and with (left) exhaust gas flow

exhaust back-pressure because the pressure difference created due to the scoop in the outlet region is relatively strong and masks the increase in hydrostatic pressure due to the wave elevation.

6.2.5. Flow development around the scoop

In this section, a qualitative analysis of the development of the flow around the two geometries of the scoop is presented. This will help to formulate the design criteria regarding the behaviour of the flow around the new scoop geometry.

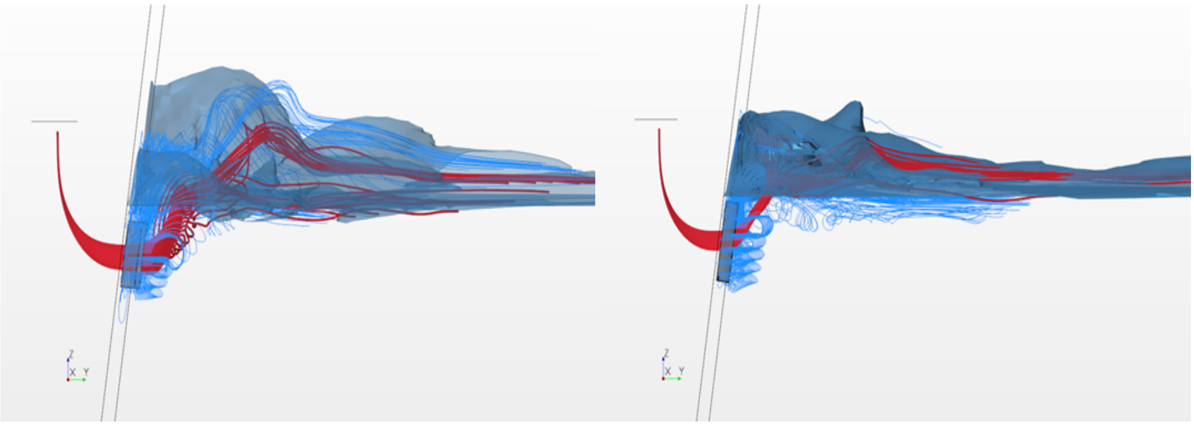

(a) Scoop geometry 1 (b) Scoop geometry 2

Figure 6.13: Front view - Streamlines around scoop

Figure 6.13 and Figure 6.14 show the exhaust gas streamlines in red and sea-water streamlines in blue from a front and side view respectively.

It can be observed that the current frontal shape of both the scoops redirects the sea-water to go over the scoop surface. This forms a local wave elevation above the scoop which increases the net water column.

Also near the rear section of the scoop, it can be observed that the exhaust gas tries to escape and rise above the water as soon as the scoop surface ends. This in turn creates an exhaust jet spray near the hull as the escaping exhaust gas tries to lift the water above it.

Since the exhaust gas filled region near the outlet is a low pressure region, the water flowing on the side of the scoop having a high pressure tries to move into the low pressure region. This forces the exhaust gases to move towards the hull upon rising out of the water, thereby discoloring the hull.

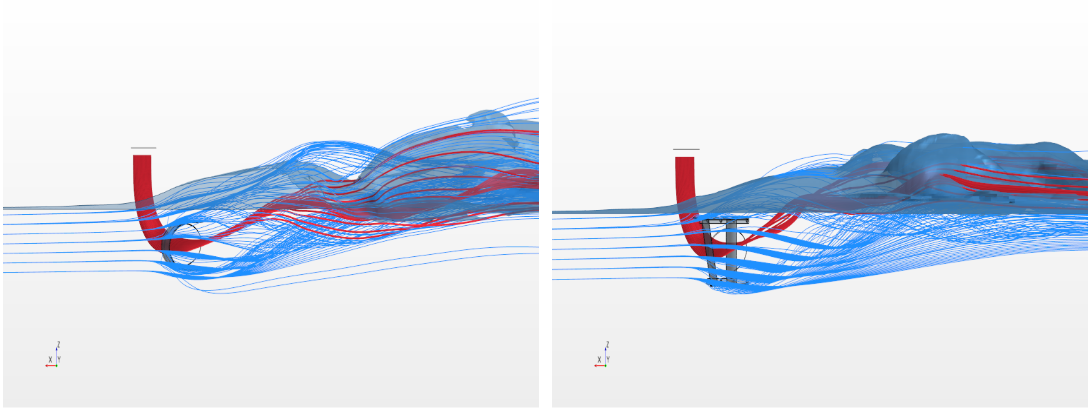

(a) Scoop geometry 1

(b) Scoop geometry 2

Figure 6.14: Side view - Streamlines around scoop

The smooth frontal section of the scoop geometry 1 redirects the flow in a better way than scoop geometry 2. Also, the vertical plate at the front of scoop geometry 2 creates a large area of stagnation pressure. Thus, as mentioned in the previous section, the resistance of scoop geometry 2 is higher than the resistance of scoop geometry 1. Additionally, the shape of scoop geometry 1 shows less unsteadiness in the wake of the scoop compared to the scoop geometry 2. The low amount of unsteadiness can also help in preventing the exhaust gas from escaping the water more quickly.

6.2.6. Air pocket formation

Figure 6.15 shows the volume fraction of air for both the scoop geometries. It can be seen in Figure 6.15b that air is diffused into the exhaust outlet region. This air can form air pockets as well as causes an immediate escape of the exhaust gas. A sufficiently thick layer of sea-water above the scoop and a smooth flow can prevent such diffusion of air in the outlet region.

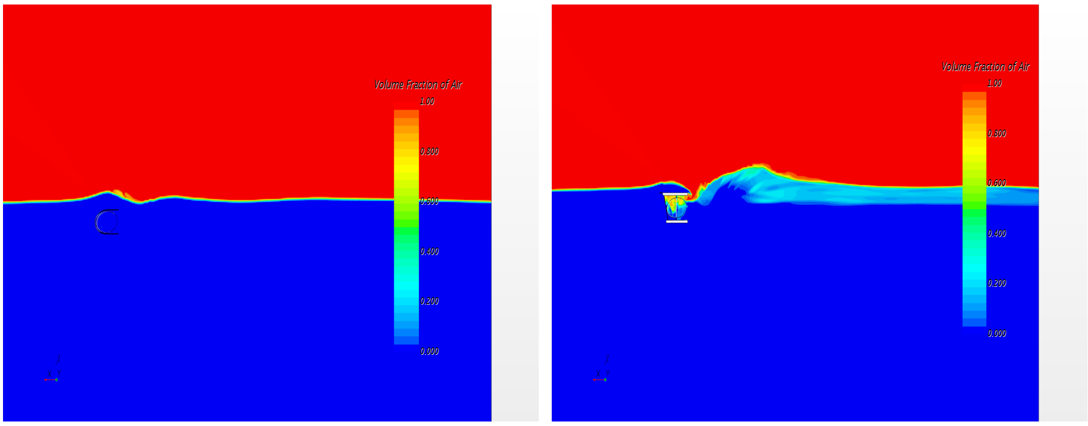

(a) Scoop geometry 1

(b) Scoop geometry 2

Figure 6.15: Side view - Volume fraction of air

6.3. Parameters of significance

This section describes the important parameters which affect the performance of the exhaust scoop.

6.3.1. Density of the exhaust gas

In this section, the density of the exhaust gas mixture is varied. The density is largely dependent on the amount of water sprayed from the water injector inside the exhaust system. A higher volume flow rate of water from the injector leads to a higher density of the exhaust gas due to the increased concentration of water vapour in the mixture.

It must be noted that the other parameters such as the yacht velocity ($10\ knots$), the submergence depth of the outlet ($0.375\ m$) and the mass flow rate of the exhaust gas ($42\ kg/s$) are kept constant. Furthermore, the sensitivity test is performed only with the scoop geometry 1.

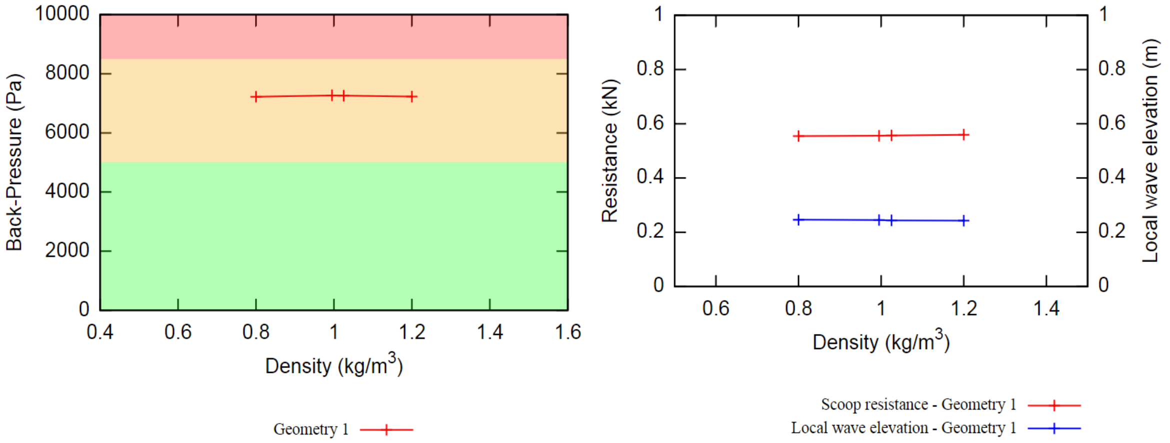

(a) Exhaust back-pressure vs. density (b) Scoop resistance and local wave elevation

Figure 6.16: Effect of exhaust gas density

Figure 6.16a presents the exhaust back-pressure values against the density of the exhaust gas mixture. It can be observed that there is no significant difference in the exhaust back-pressure with a variation in density. Figure 6.16b presents the resistance of the scoop and the local wave elevation above the scoop against the variation in density. Similar to the exhaust back-pressure, no significant change can be observed for both quantities.

Thus, it can be concluded that the density of the exhaust gas mixture does not significantly affect the performance criteria of the scoop.

6.3.2. Mass flow rate of the exhaust gas

In this section, the mass flow rate of the exhaust gas is varied. Apart from the engine loading conditions, the mass flow rate also depends on the volume flow rate of the water from the injector. The values considered in this test are based on the maximum loading conditions of different diesel engines.

Here, the other parameters such as the yacht velocity ($10\ knots$), the submergence depth of the exhaust outlet ($0.375\ m$) and the density of the exhaust gas ($0.995\ kg/m^3$)

are kept constant.

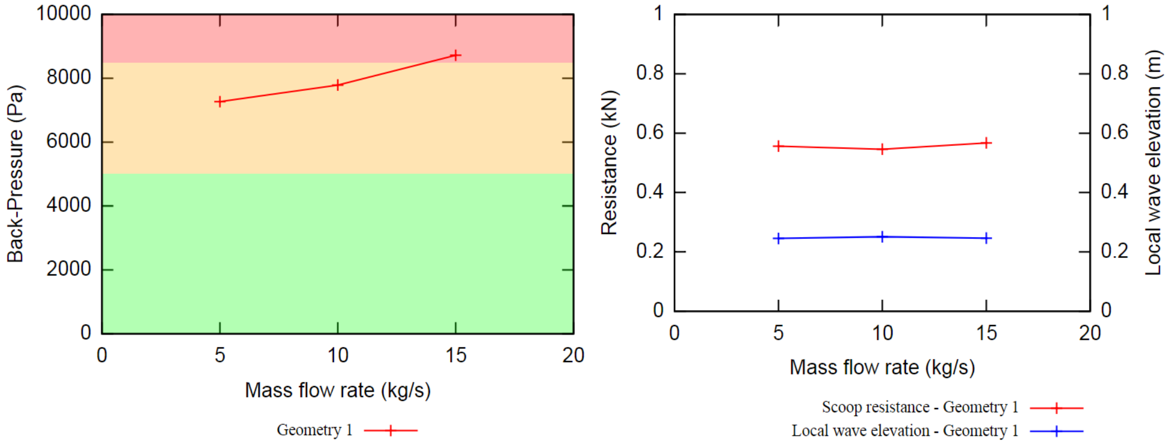

(a) Exhaust back-pressure

(b) Scoop resistance and local wave elevation

Figure 6.17: Effect of mass flow rate

Figure 6.17a shows the effect of the mass flow rate on the exhaust back-pressure. It can be observed that the exhaust back-pressure rises considerably with the increase in the mass flow rate of the exhaust gas.

The pressure drop in the after-treatment systems increases with an increase in the mass flow rate of the exhaust gas. In the computational domain, the after-treatment systems for the exhaust gas are not modelled, thereby the pressure drop in those systems is not calculated in CFD analysis. Instead the pressure drop due to the after-treatment systems are taken as a constant value from the external source. Thus, the additional pressure drop in the after-treatment systems due to the high mass flow rate is not accounted for in the exhaust back-pressure calculation in the CFD analysis.

To account for this pressure drop due to a high mass flow rate in the CFD calculations, the pressure drop value for the after-treatment systems should be calculated for the respective mass flow rate of the exhaust gas used in the CFD analysis. This value should then be used to calculate the exhaust back-pressure.

Figure 6.17b shows the effect of the mass flow rate on the scoop resistance and the local water elevation. It can be observed that there is no prominent difference in values due a variation in the mass flow rate.

To conclude, the pressure drop value from the after-treatment systems cannot be generalized for all cases as it is highly dependent on the mass flow rate of the exhaust gas. This pressure drop significantly affects the exhaust back-pressure. Additionally, as a rule of thumb, the diameter of the exhaust pipe or the number of exhaust outlets should be increased to avoid an excessive pressure loss due to a high mass flow rate.

6.3.3. Submergence depth of the exhaust outlet

In this section, the submergence depth of the exhaust outlet is varied. The submergence depth is measured from the initial waterline of the hull to the centre of the underwater outlet. The submergence depth is an important factor in determining the scoop performance as the hydrostatic pressure is directly proportional to this parameter.

For this sensitivity test, other parameters such as the yacht velocity ($10\ knots$), the mass flow rate of the exhaust gas ($42\ kg/s$) and the density of the exhaust gas ($0.995\ kg/m^3$) are kept constant.

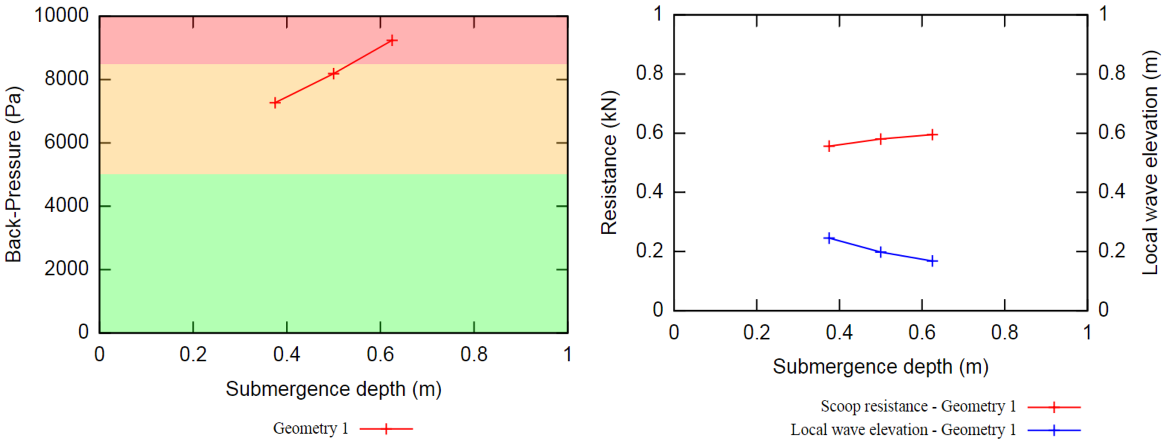

(a) Exhaust back-pressure

(b) Scoop resistance and local wave elevation

Figure 6.18: Effect of submergence depth

Figure 6.18a shows the effect of the submergence depth on the exhaust back-pressure. It can be observed that there is a sharp increase in the exhaust back-pressure with an increase in submergence depth. This is due to an increase in the hydrostatic pressure component, which increases linearly with the height of the water column above the scoop. At 0.625 m, the exhaust back-pressure crosses the maximum allowable limit set by the engine supplier. This could lead to excessive damage to the internal components of the engine.

Figure 6.18b shows the changes in the scoop resistance and the local water elevation due to a variation in the submergence depth. With respect to the scoop resistance, it can be seen that there is an increase in resistance with an increase in the submergence depth. This is due to an increase in the pressure forces due to a large water column acting on the upper surface of the scoop. In addition, the local water elevation reduces with an increase in the submergence depth. As the exhaust outlet is placed further below the waterline, the exhaust plume is dispersed further away from the hull, which reduces the local water elevation above the scoop. This helps in reducing the additional hydrostatic pressure caused by this local water elevation.

To conclude, the submergence depth of the exhaust outlet is an important variable in determining the performance of the scoop. To avoid excessive hydrostatic pressure, the submergence depth should be limited according to the scoop geometry.

6.3.4. Hull displacement

Hull displacement has a noticeable impact on the draft of the yacht. With the increase or decrease in the hull displacement, the draft will increase or decrease respectively. The change in draft directly alters the submergence depth of the underwater exhaust outlet.

Any change in hull displacement will have a similar consequence on the performance of the scoop as the change in the submergence depth which is described in Section 6.3.3. Thus, the scoop performance for any variation in the hull displacement can be directly extrapolated from the results of the variation in submergence depth.

6.3.5. Surface wave

Surface waves are formed on the free surface of the water body due to the action of wind. These surface waves result in the formation of crests and troughs during the propagation of a wave. When a crest is formed, it will increase the net submergence depth for the underwater outlet. This results in an increased back-pressure and a higher resistance as described in the Section 6.3.3.

In contrast, the formation of a trough will expose the exhaust outlet partially or completely above the free surface. This can lead to the formation of air pockets as explained in Section 6.2.6. Additionally, the back-pressure will be reduced considerably due to the removal of water column, leading to a zero net submergence depth.

Thus, the performance of the scoop under the impact of surface waves can be predicted from the results of the variation in submergence depth.

6.3.6. Internal pressure loss

The exhaust back-pressure is calculated as:

$$P_B = \Delta P + P_{scoop} \, . \tag{6.1}$$

In the above equation, the exhaust back-pressure P_B is dependent on the total internal pressure losses ΔP and the pressure at the underwater outlet P_{scoop}. The P_{scoop} remains constant for a specific geometry and a specific velocity. However, ΔP depends on the internal pipe layout and the after-treatment systems used for a particular yacht. Thus, ΔP is an influential parameter to accurately predict the range of back-pressure for a specific yacht configuration.

This parameter can be studied in detail by modelling the internal exhaust system for the specific yacht and examining its effect on the back-pressure. However, it lies outside the scope of this research work.

7

Analysis of Modified Geometries

The study in this chapter is based on the scoop geometry 1 presented in the previous chapter. This chapter describes the effect of varying several geometrical parameters of the scoop geometry on the performance of the underwater exhaust system. Based on the discussion of these results, the optimal geometry for the existing scoop will be decided.

7.1. Geometry selection

The design study in this research work is based on the assumption that the exhaust scoop is performing under a fully loaded yacht. There can be several instances where the yacht is partially loaded which directly affects the submergence depth of the underwater exhaust outlet. This can presumably lead to a partial submerged condition for the scoop. Moreover, a rough sea-state can lead to a similar condition for the scoop. In the above scenarios, a partially submerged scoop condition is defined as the state where the center of the underwater exhaust outlet coincides with the free surface. In such conditions, an ideal scoop geometry should make sure that the underwater exhaust outlet remains submerged and should provide the required performance.

Figure 7.1 shows the scoop geometry 1 and scoop geometry 2 in a partially submerged condition.

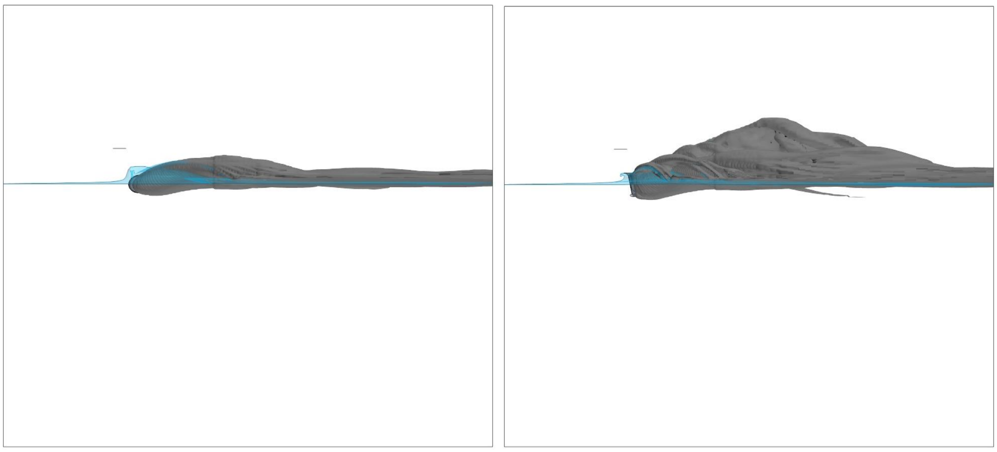

(a) Scoop geometry 1

(b) Scoop geometry 2

Figure 7.1: Side view - Partially submerged original scoop geometries at 10 knots

As observed from Figure 7.1b, scoop geometry 2 leads to a large amount of sprays.

Furthermore, the contaminated area on hull due to the exhaust mixture is significantly larger. On contrary, scoop geometry 1 stays covered with a layer of sea-water as observed in Figure 7.1a. This reduces the formation of exhaust sprays and also the contaminated area stays relatively low. Thus, scoop geometry 1 is chosen as reference to further improve the design and performance of the scoop.

7.2. Effect of the deflection angle

The first geometrical parameter considered in the study is the deflection angle of the scoop with respect to the hull surface. Further explanation is provided below.

7.2.1. Geometry explanation

Figure 7.2 shows a top view of the scoop geometry. The deflection angle is measured with respect to the vertical hull surface. The angle was kept at 120^o in the original scoop geometry 1 as seen in the Figure 7.2a (The figure shows the top view with the hull cross-section and the scoop attached to it).

As displayed in Figure 7.2b, the angle is varied in the range from 60^o to 150^o with a constant exhaust outlet diameter of $500\,mm$ and a constant extrusion length of $250\,mm$. Additionally, the yacht velocity was fixed at $10 knots$ and the mass flow rate of the exhaust gas is kept constant at $42\,kg/s$. With the excessive deflection angles outside the chosen range, the scoop geometry blocks the underwater exhaust outlet creating an undesirable blockage for the flow of the exhaust mixture.

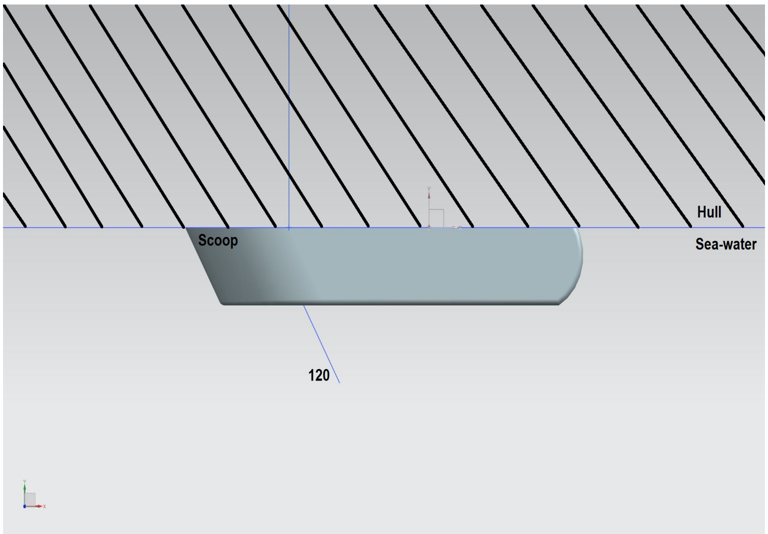

(a) Original scoop geometry 1

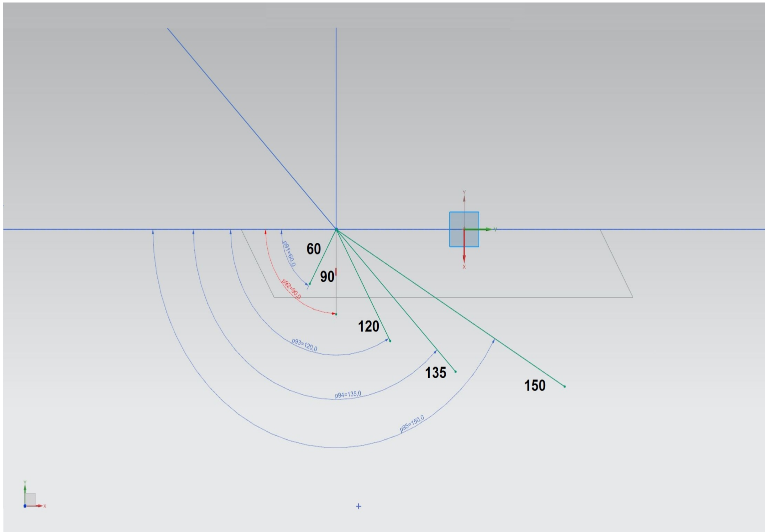

(b) Variation in deflection angle

Figure 7.2: Top view - Deflection angle for scoop geometry

7.2.2. Scoop performance

Figure 7.3a presents the effect of the deflection angle on the back-pressure of the underwater exhaust system. It can be observed that the back-pressure has small variations until 135^o. With a further increase in the deflection angle, the back-pressure increases rapidly. The rapid increase is attributed to the blockage of the exhaust outlet as a result of the increased deflection angle of the scoop.

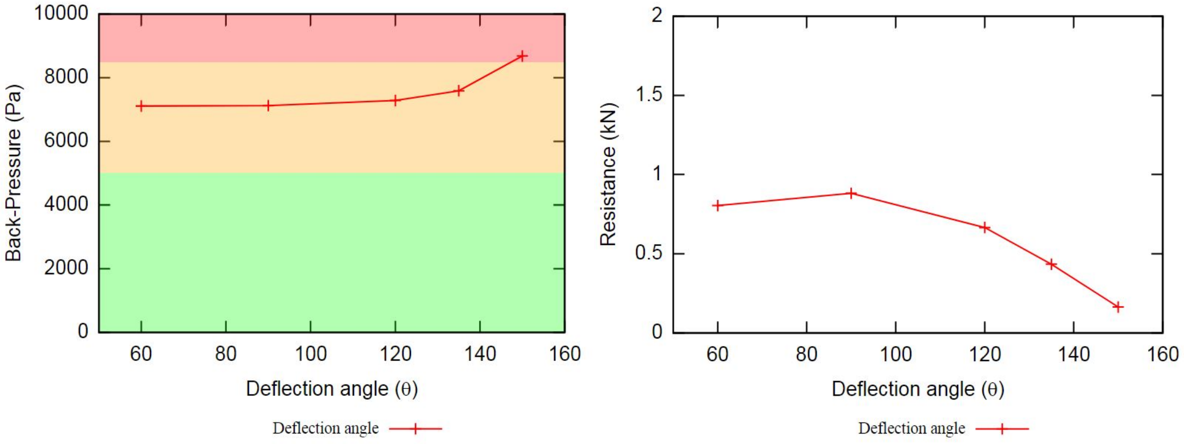

(a) Back-pressure (b) Scoop resistance

Figure 7.3: Effect of varying deflection angle

Figure 7.3b presents the effect of the deflection angle on the resistance of the scoop. As observed, the back-pressure and the scoop resistance are inversely related. There is a sharp decrease in resistance with the increase in the deflection angle of the scoop.

Scoop resistance can be divided into pressure drag and skin friction. Figure 7.4 shows the variation of both the components with the change in the deflection angle. The skin friction does not experience a significant change while the pressure drag reduces rapidly with increasing deflection angle. This is caused by decrease in frontal area of the scoop with the increased deflection angle.

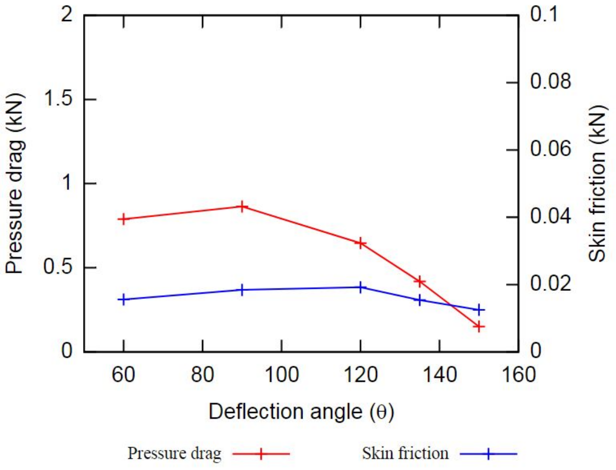

Figure 7.4: Pressure drag and skin friction

It can be concluded here that the scoop provides an optimal performance when the deflection angle is in the range of 60^o to 120^o. However, it is important to investigate the development of flow around the scoop to reach the final conclusion.

7.2.3. Flow development

Figure 7.5 shows the spread of the exhaust gas in the surrounding flow from a top view. It is observed that there is a significant difference in the presence of the exhaust gas near the hull. For the scoop geometry with a deflection angle of 60^o, the water flow above the scoop forces the exhaust gas away from the hull. In contrast, for the scoop geometry with a deflection angle of 120^o, the exhaust gas flow is parallel to the hull thereby helping the hull contamination.

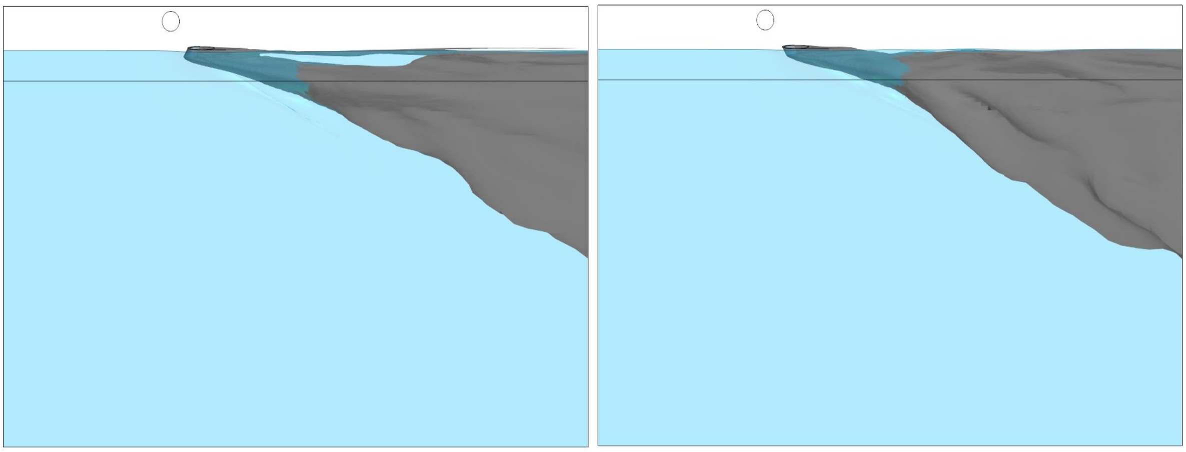

(a) Deflection angle: 60

(b) Deflection angle: 120

Figure 7.5: Top view - Flow development around scoop

Figure 7.6 shows the water and the exhaust gas streamlines around the scoop geometry with a deflection angle of 60^o. The inverted frontal shape of the scoop in the direction of the water flow guides the stream of water towards the hull instead of deflecting it away from the hull. Thereby, this stream of water pushes the exhaust gases away from the hull. The effect becomes more prominent at the high speed. Further comparison is presented in Section 7.4.

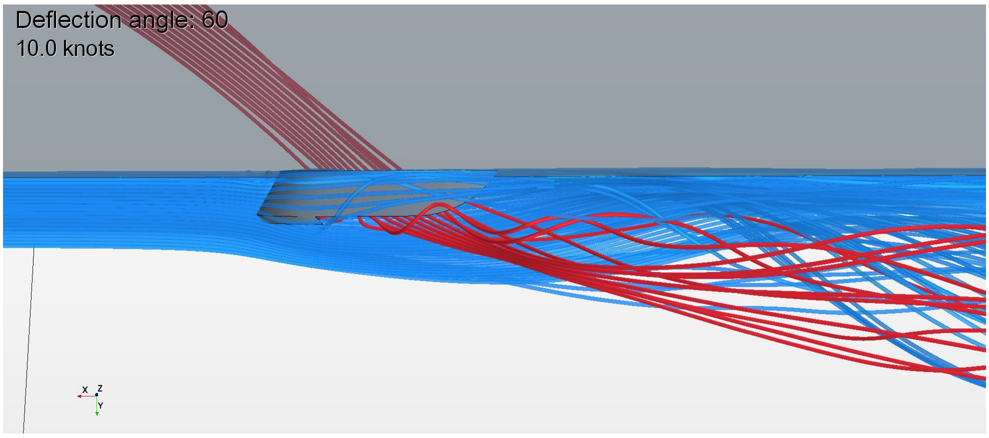

Figure 7.6: Top view - Flow streamline around scoop

Figure 7.7 shows the contaminated area of hull with the exhaust gas for varying deflection angle. The contamination area increases with an increase in the deflection angle.

Thus, it can be concluded that the scoop geometry with a deflection angle of 60^o has a better performance compared to that of the original scoop geometry 1. This modified geometry has a back-pressure value within the permissible limit as well as a low resistance. Furthermore, the flow develops around the scoop in such a way that it provides the least

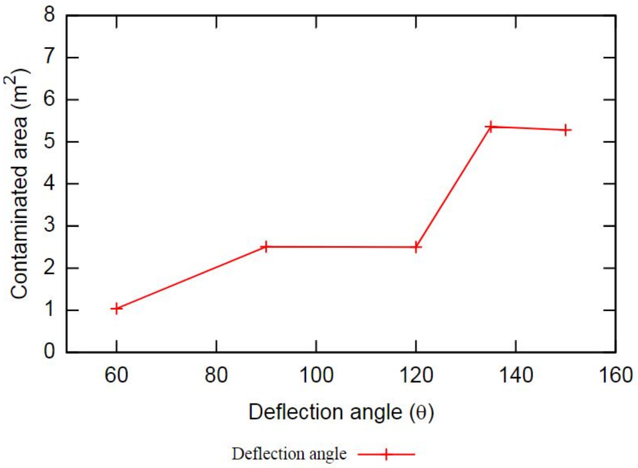

Figure 7.7: Exhaust contaminated area on hull

amount of hull contamination due to the exhaust gas.

7.3. Effect of the elliptical axis

Scoop geometry 1 is designed considering an ellipse as base. This provides two parameters in the form of the semi-major (a) and the semi-minor (b) axis of the ellipse for variation. The axes are presented in the Figure 7.8.

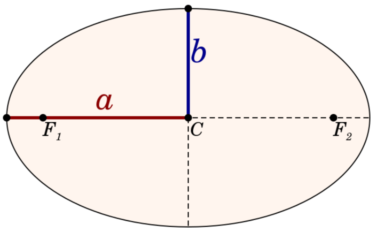

Figure 7.8: Semi-major and semi-minor axis of ellipse

7.3.1. Geometry explanation

Figure 7.9 shows the elliptical base for the scoop geometry. The two parameters i.e. the semi-major axis (a) and the semi-minor axis (b) are marked in the image. Both parameters are varied separately to study their effect on the performance of the scoop. The extrusion length of the scoop alongside the yacht velocity and the mass flow rate of the exhaust gas mixture are kept constant in this study (refer to Section 7.2.1 for values). The deflection angle is kept at 60^o based on the discussion provided in Section 7.2.

For the original scoop geometry, the length of the semi-major axis is $350\,mm$ while the length of the semi-minor axis $280\,mm$. The semi-major axis (a) is increased in the steps of 50 mm with respect to the original dimension. While the semi-minor axis (b) is increased in the steps of 20 mm with respect to the original dimension.

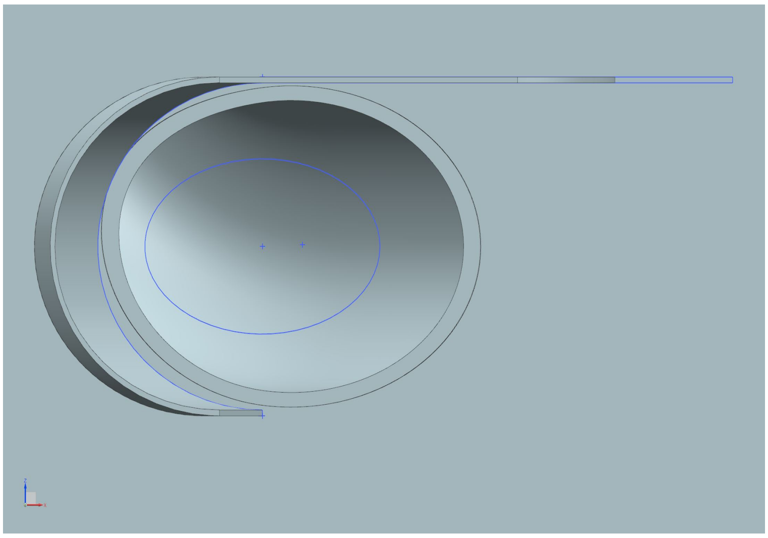

(a) Scoop geometry with deflection angle 60^o

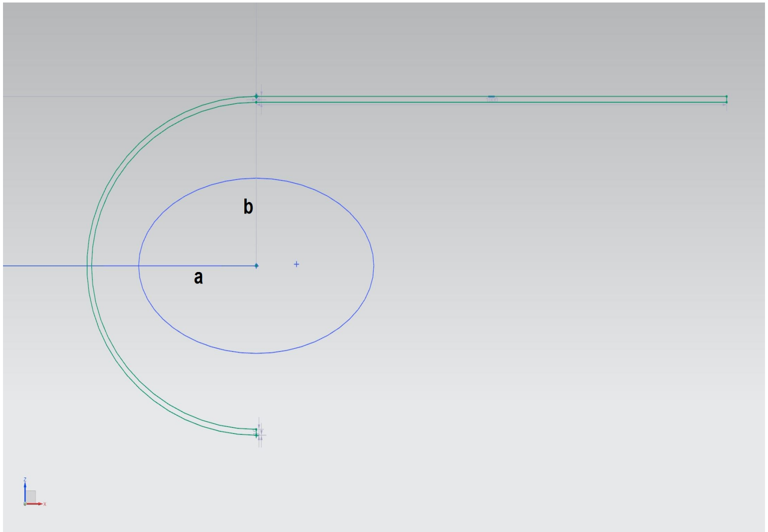

(b) Semi-major axis 'a' and semi-minor axis 'b'

Figure 7.9: Side view - Elliptical axis for scoop geometry

7.3.2. Scoop performance

Figure 7.10a presents the effect of the chosen parameters on the exhaust back-pressure. The back-pressure stays within the permissible limit given by the engine manufacturer for both parameter ranges. A slight difference in back-pressure is observed with increasing the given parameters individually. When increasing the semi-major axis, the back-pressure increases slightly, while in case of an increase in the semi-minor axis, the back-pressure is reduced marginally.

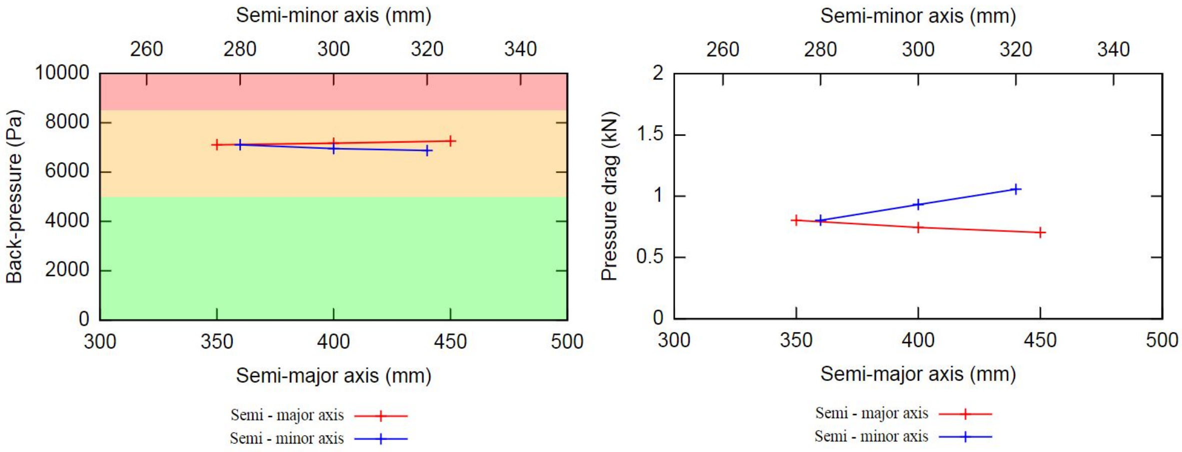

(a) Back-pressure (b) Scoop resistance

Figure 7.10: Effect of varying elliptical axis

Figure 7.10b shows the effect on the overall scoop resistance. As observed in the previous section, the scoop resistance is inversely related to the change in back-pressure. As observed from Figure 7.11, the pressure drag is a significant component in the scoop resistance. With the increase in the semi-major axis of the scoop, the frontal area decreases leading to a reduced pressure drag. For the semi-minor axis, the frontal area of the scoop increases with an increase in the semi-minor axis. This leads to an increased pressure drag. The skin friction is marginally affected with an increase in either of the parameter.

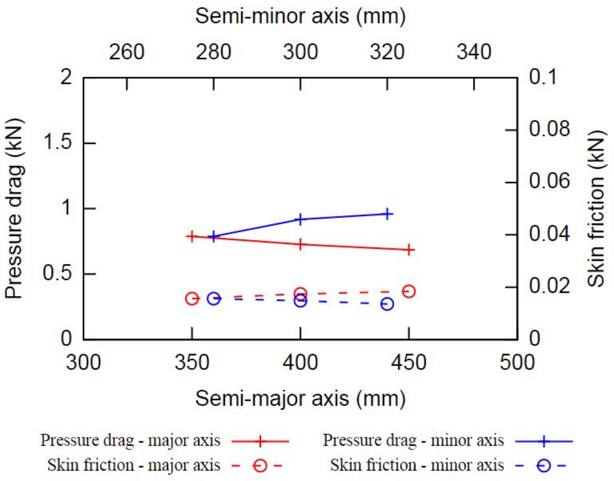

Figure 7.11: Pressure drag and skin friction

7.3.3. Flow development

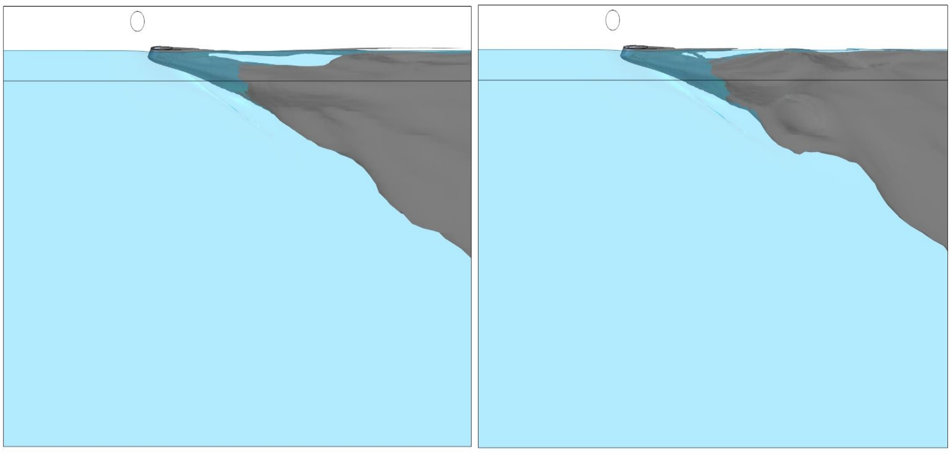

(a) Original dimension

(b) Semi-major axis: 450 mm

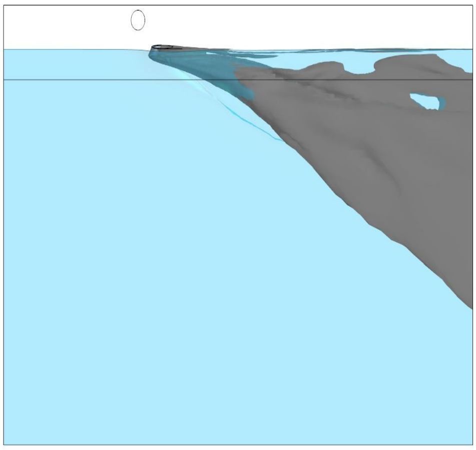

(c) Semi-minor axis: 320 mm

Figure 7.12: Top view - Flow development around scoop

Figure 7.12 presents the spread of exhaust gas mixture around the hull from a top view for three different modified scoop geometry. For the modified scoop with a semi-major axis of 450 mm, the separation of the exhaust gas mixture from the hull was slightly reduced compared to the original dimension. While for a modified scoop with a semi-minor axis of 320 mm, the separation area relatively increased guiding the exhaust gas mixture further away from the hull.

Furthermore, Figure 7.13 shows the contaminated area on hull due to the exhaust gas mixture. The contaminated area is slightly increased with an increasing semi-major axis. However the increase in the contaminated area is significantly higher for increasing the semi-minor axis.

To conclude, increasing the semi-minor axis provides a favourable behaviour for guiding the exhaust mixture away from the hull. In contrast, the resistance increases compared to the original scoop. Also, changing the semi-major axis does not provide any significant benefits in terms of back-pressure or flow development over the original scoop. Thus, the original geometry of the scoop will be retained.

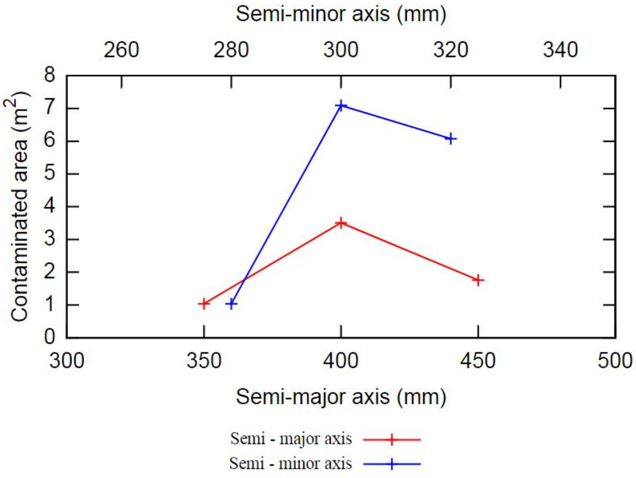

Figure 7.13: Exhaust contaminated area on hull

7.4. Optimal modification for scoop geometry

Based on the results described in Section 7.2 and Section 7.3, the scoop geometry 1 is modified with a deflection angle of 60^o. No changes were made with the elliptical axis. The performance of the modified geometry for different velocities and different submergence depths are discussed in the upcoming section.

7.4.1. Scoop performance

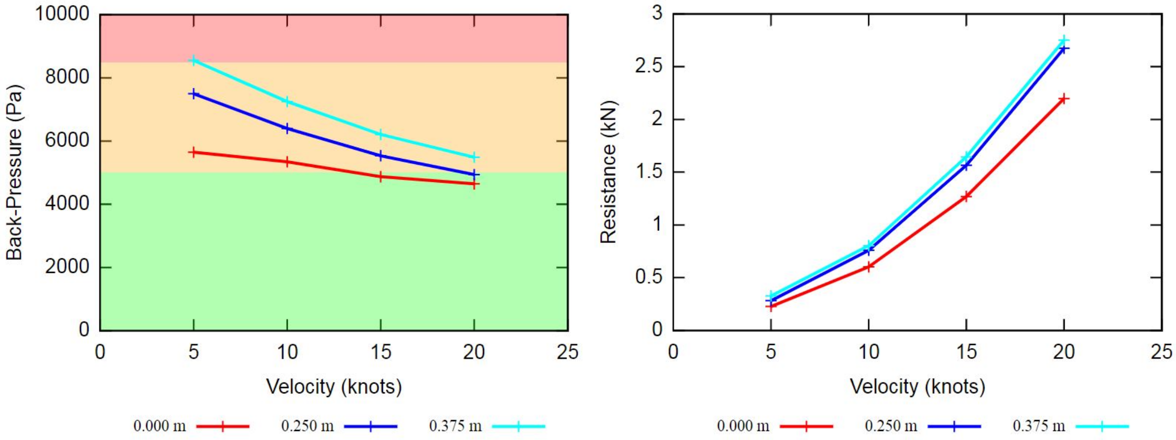

(a) Back-pressure

(b) Scoop resistance

Figure 7.14: Performance of optimal scoop geometry

Figure 7.14 presents the back-pressure and the scoop resistance of the modified scoop geometry for a range of yacht velocities. Furthermore, the modified geometry is tested for different submergence depths to study its impact on the scoop performance. 0.000m case refers to the partially submerged exhaust outlet. As observed from Figure 7.14a, the back-pressure reduces with an increasing velocity. Additionally, the back-pressure increases significantly with an increasing submergence depth. This impact is stronger at a low velocity where the increment is as high as 50%. However, for sufficiently high velocities, the increment in back-pressure is low (15%) when increasing the submergence depth.

Figure 7.14b shows the variation in scoop resistance for different velocities. The scoop resistance increases with the velocity. Furthermore, with increasing submergence depth, the resistance increases due to the additional hydrostatic pressure on the scoop surface. The increment in resistance is relatively small between 0.250 m and 0.375 m.

7.4.2. Flow development

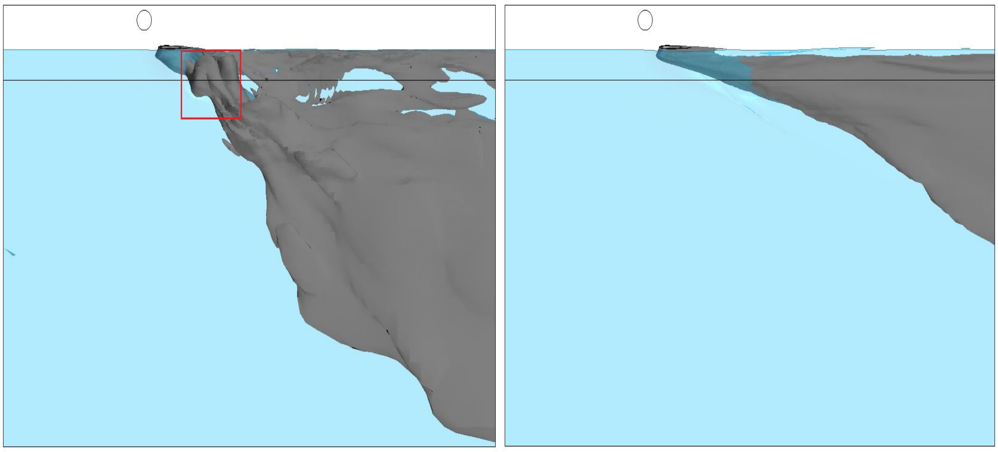

(a) 5 knots (b) 10 knots

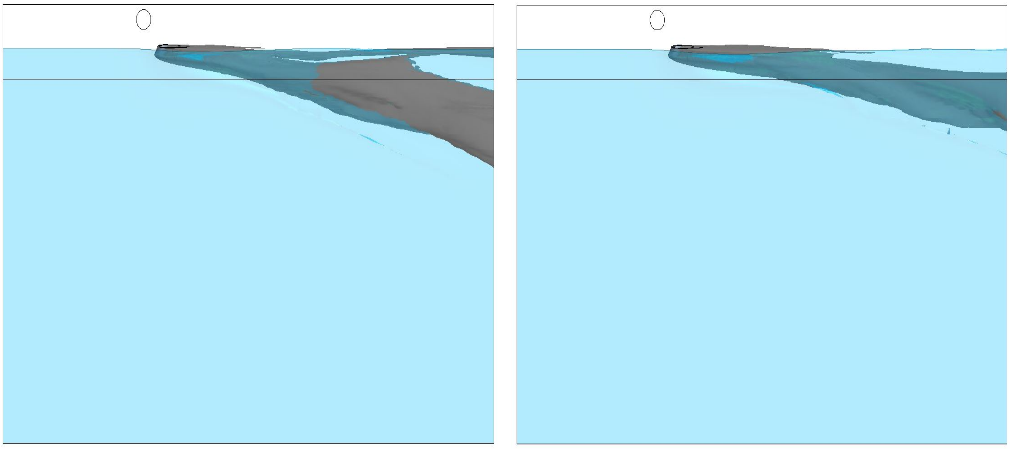

(c) 15 knots (d) 20 knots

Figure 7.15: Top view - Flow development around modified scoop

Figure 7.15 shows the spread of exhaust gas mixture in the surrounding sea-water at different velocities for the modified scoop geometry with a submergence depth of 0.375 m. At 5 knots, the exhaust mixture quickly escapes the surface of the water due to the low kinetic head as observed in Figure 7.15a. Furthermore, a quick escape of the exhaust mixture forms an exhaust spray near the scoop surface as seen in the red box. Additionally, even though the bulk of the exhaust mixture is redirected away from the hull at a low velocity, there is a considerable amount of exhaust mixture near the hull leading to contamination. This is also shown in Figure 7.17.

At 10 knots, the spread of the exhaust mixture is constrained to the surrounding sea-water. There is a very low contamination on the hull due to the presence of a stream of water as observed from Figure 7.15b. Furthermore, there is no formation of exhaust spray due to the slow escape of the exhaust mixture away from the scoop surface. The escape of the exhaust mixture is delayed further with the increase in the velocity as observed in Figure 7.15c.

At 20 knots, the spread of the exhaust mixture is extremely constrained as observed from Figure 7.15d. Also, the exhaust mixture stays submerged within the sea-water for a longer duration. The bulk of the exhaust mixture is redirected away from the hull leading to an extremely low hull contamination. This redirection of the exhaust mixture is due to the formation of the vortical structures as observed in Figure 7.16.

The vortical structures are formed due to differences in pressure between the exhaust mixture and the surrounding sea-water. The strength of this structures increases with increasing yacht velocities.

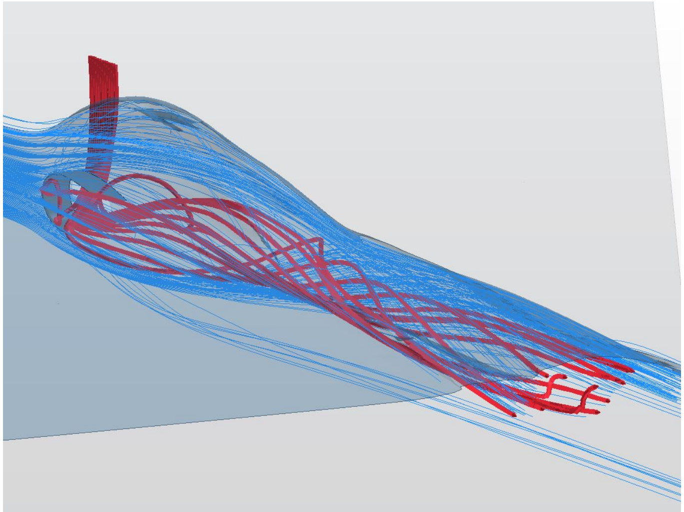

Figure 7.16: Vortical structures

Figure 7.17 presents the contaminated area of hull due to exhaust gas mixture for different velocities. It is observed that the contaminated area is large for low velocity. This is due to the formation of an exhaust spray at low velocities. Additionally, the contaminated area is the largest for a submergence depth of 0.375 m because the height of exhaust spray is increased with the increasing an submergence depth.

As the velocity is increased, the contaminated area on the hull decreases and becomes almost constant at high velocities. Furthermore, with an increasing submergence depth, the contaminated area becomes relatively small due to improved mixing of exhaust gas with the sea-water.

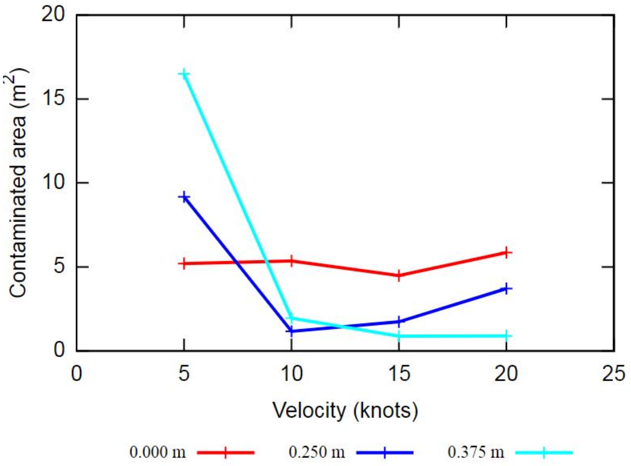

Figure 7.17: Exhaust contaminated area on hull

8

Analysis of New Geometries

The study in this chapter involves new concept geometries for the exhaust scoop. The chapter is divided into two sections: the first section shows the simple variations in scoop geometry and the second section shows a conceptual scoop design based on previous observations from Chapter 5.

8.1. Air-blown exhaust scoop

In section 5.4.1, an important phenomenon was observed for the case with two active underwater exhaust outlet. It was shown that the exhaust gas mixture from the rear outlet initially interacts with the exhaust mixture released from the front outlet. This interaction helped in achieving a low back-pressure at the rear outlet compared to that of the front outlet. The new concept geometry of the air-blown scoop is based on this phenomenon.

8.1.1. Geometry explanation

Figure 8.1 shows the air-blown exhaust scoop geometry. The geometry used for this concept is based on the modified scoop geometry 1 discussed in Chapter 7. The geometry is provided with the two outlets as seen in the figure. The front outlet is used as an air outlet which blows air along the scoop geometry. The rear outlet is the usual exhaust gas outlet. A small deflector is provided between the two outlets. This prevents the air from diffusing inside the exhaust outlet at the start of operation.

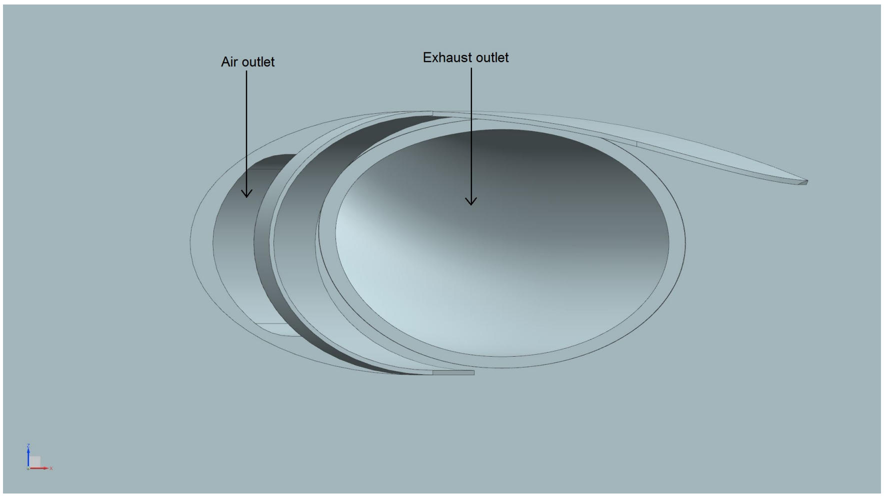

Figure 8.1: Side-view: Air-blown scoop geometry

8.1.2. Scoop performance

Figure 8.2 presents the exhaust back-pressure for different yacht velocities at a constant mass flow rate of the exhaust mixture. Furthermore, it shows the effect of varying the mass flow rate of air on the back-pressure. At $0\,kg/s$ (i.e. air outlet is closed), the back-pressure is relatively high compared to the back-pressure obtained under the influence of the active air outlet. At $2\,kg/s$, the exhaust back-pressure is approximately reduced by 15% compared to the back-pressure when the air outlet is closed. Upon increasing the mass flow rate of air to $5\,kg/s$, the back-pressure is reduced by approximately 26% compared to the back-pressure when the air outlet is closed. A significant decrease in back-pressure is observed especially at a high velocities where the engine is functioning at maximum load. At high velocities, the back-pressure drops within the safe limit (i.e. green area in figure) of engine operation.

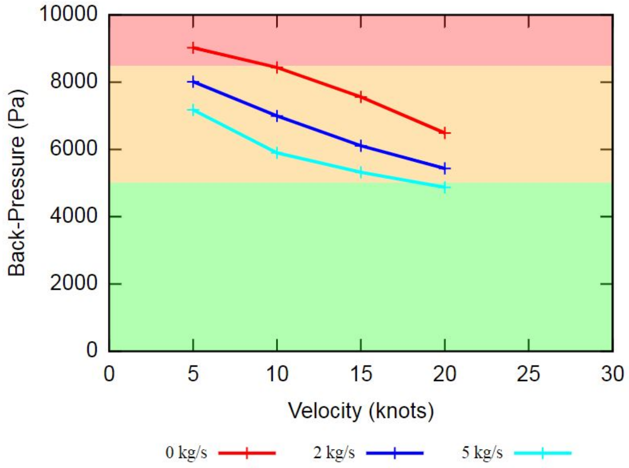

Figure 8.2: Back-pressure for air-blown scoop geometry

This reduction in back-pressure is due the interaction of the exhaust mixture with the air instead of sea-water. The surrounding air creates a region of low-pressure thereby reducing the pressure created by the sea-water at the exhaust outlet. This leads to an effective improvement in the scoop performance.

Figure 8.3a shows the effect of different mass flow rates of air on the exhaust back-pressure at a constant velocity of 10 knots. The back-pressure reduces considerably when increasing mass flow rate of air up to $7.5\,kg/s$. Upon further increasing the mass flow rate, the back-pressure increases. This is due to the excessive force of the air creating a turbulent region near the scoop as observed in Figure 8.3b. Thus to avoid such a condition, the safe limit for the mass flow rate of air is kept at $5\,kg/s$.

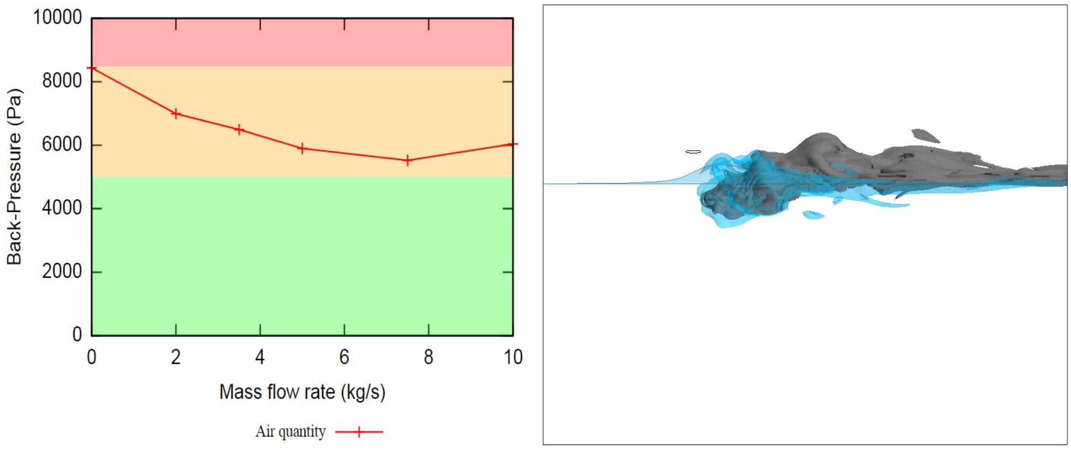

(a) Dependency on mass flow rate of air

(b) Excessive mass flow rate

Figure 8.3: Air-blown scoop resistance

Figure 8.4 presents the effect of the new geometry on the overall scoop resistance. It is observed that the resistance increases when the air outlet is active. At the highest velocity, the scoop resistance is approximately increased by 38% compared to the resistance when the air outlet is closed. This increase is due to the change in the flow velocity caused by the air around the scoop. This leads to an increase in the dynamic pressure over the scoop surface, thereby giving higher pressure drag.

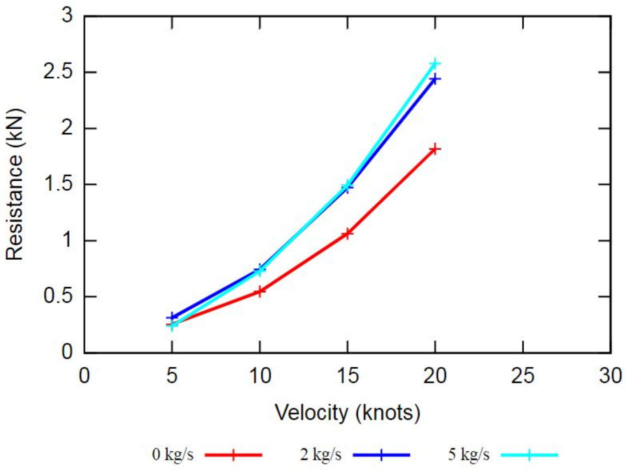

Figure 8.4: Total resistance

8.1.3. Flow development

Figure 8.5a shows the development of flow around the air-blown scoop geometry at 10 knots with an air mass flow rate of $5\ kg/s$. A layer of air can be observed covering the exhaust gas mixture exiting the underwater outlet. Furthermore, the formation of a water-column above the scoop delays the escape of the exhaust mixture from sea-water.

Also, as observed from Figure 8.5b, the bulk of the exhaust mixture is diverted away from the hull leading to a low contaminated area.

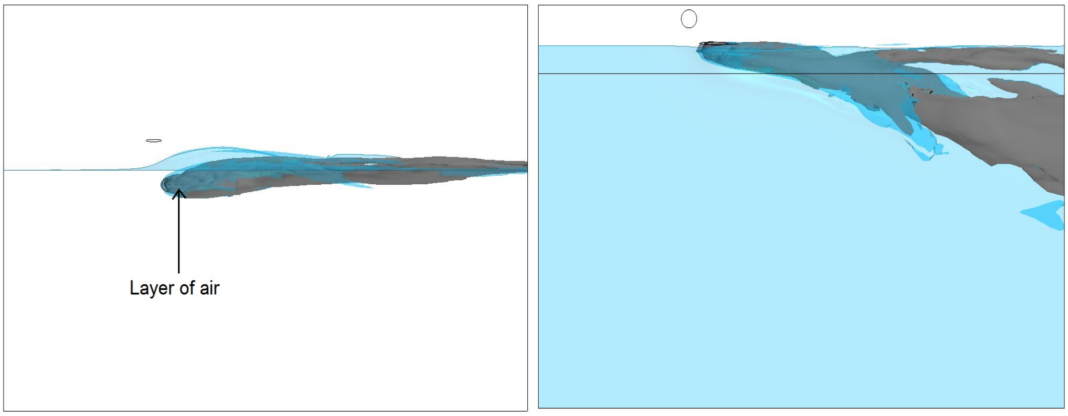

(a) Side-view (b) Top-view

Figure 8.5: Flow development around air-blown scoop geometry

Figure 8.6 shows the hull contamination due to the exhaust mixture for the new scoop geometry. At 5 knots, the contaminated area is significantly higher for air mass flow rate of $5\,kg/s$. This is due to the exhaust spray caused by the immediate escape of the air at a low velocity. At higher velocity, no considerable difference can be observed in the contaminated area.

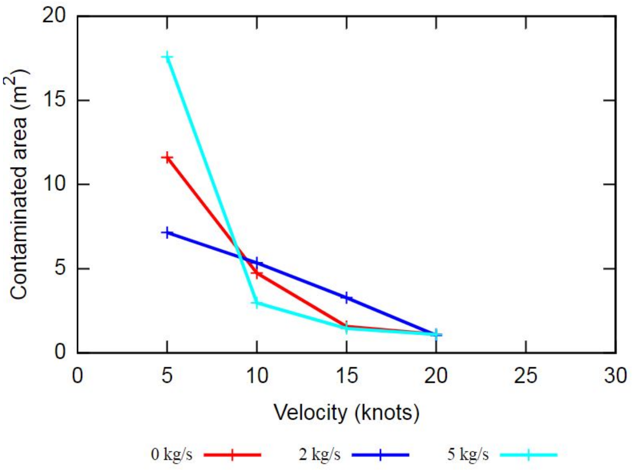

Figure 8.6: Exhaust contaminated area on hull

To conclude, the air-blown exhaust scoop provides significant improvements over the existing scoop geometry in terms of back-pressure and contamination area.

8.2. Design variation

This section explores alternate geometries for a scoop design and its influence on the performance of the scoop. Design 1 and Design 2 in Figure 8.7 are based on shapes that can provide a considerably low pressure drag. The smooth curved surface of these scoops would allow a smooth flow of sea-water around the underwater exhaust outlet. These designs can presumably lead to a high water-column above the scoop surface. In case of Design 2, it was presumed that such a geometry would help to reduce the exhaust spray by preventing the immediate escape of the exhaust gas mixture.

For Design 3 and Design 4, the main motivation was to create such a geometry that would have a minimum interruption with the wave profile of the hull. Such a geometry will prevent the exhaust sprays and local water elevation above scoop surface. Design 3 is based on the idea that a flat surface of the scoop would eliminate the formation of a water-column above the scoop surface. Design 4 is a combination of idea behind Design 1 and Design 3. It was presumed that such a geometry will be able to achieve a low pressure drag and a low water-column above the exhaust outlet.

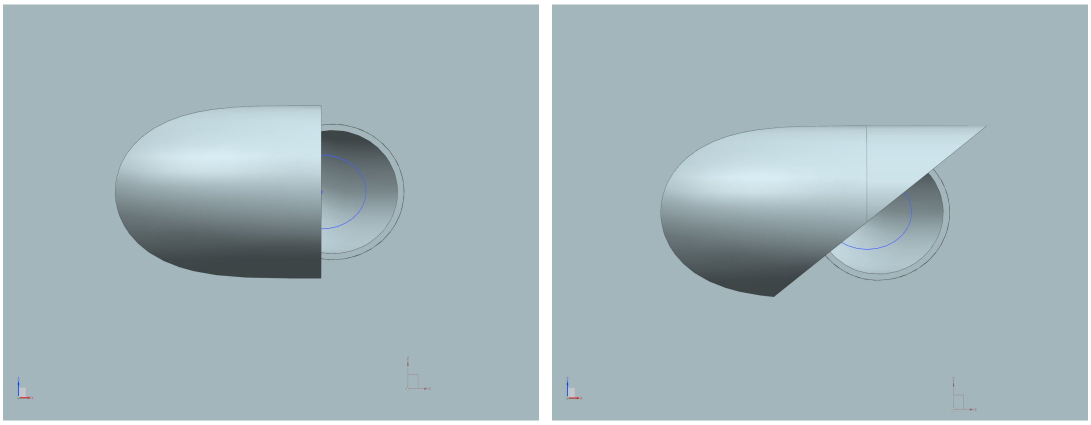

(a) Design 1 (b) Design 2

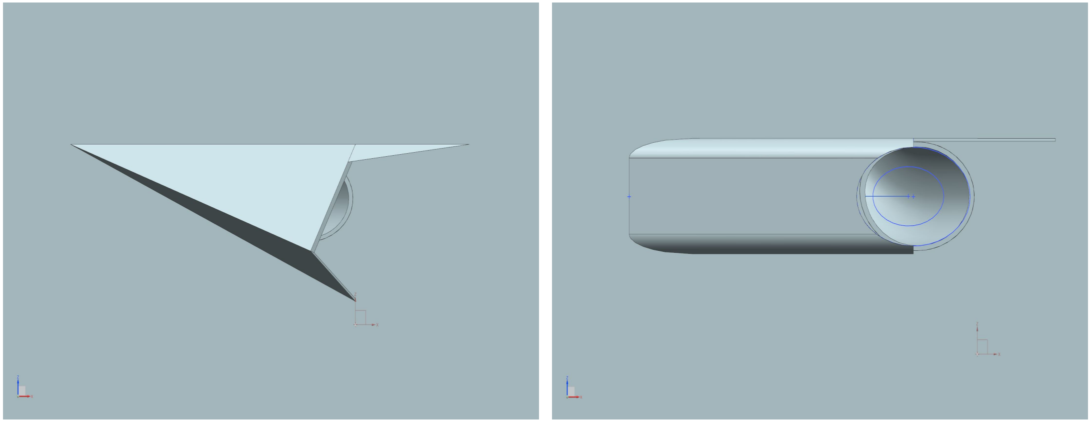

(c) Design 3 (d) Design 4

Figure 8.7: Scoop geometry variation

It must be noted that, there were several iterations carried out with the alternate scoop geometries mentioned here. Not all those iterations provided any considerable performance improvement over the existing geometries. Thus, only limited results with the above described alternate geometries are discussed in further sections.

Moreover, a concept similar to the air-blown exhaust scoop was implemented in an alternate scoop geometries. Such a geometry amplified the formation of the exhaust sprays around the hull. Thus, such a concept was not considered further.

8.2.1. Scoop performance

This section discusses the performance of the above mentioned scoop designs. The simulations are carried out with a constant yacht velocity ($10\,knots$) and a constant mass flow rate of the exhaust mixture ($42\,kg/s$) for various scoop designs.

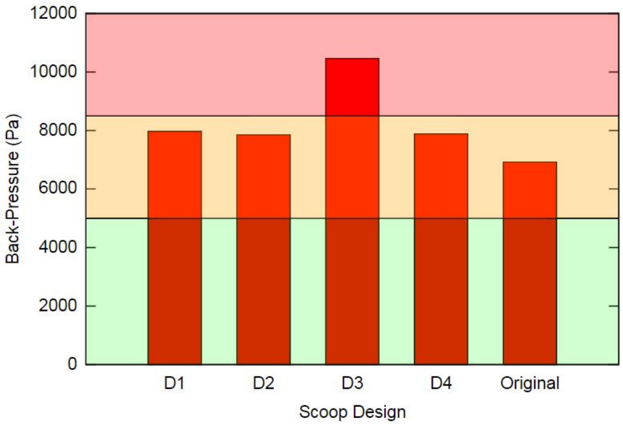

Figure 8.8: Back-pressure

Figure 8.8 shows the influence of the scoop design on the exhaust back-pressure. For Design 1 (D1), Design 2 (D2) and Design 4 (D4), the back-pressure is approximately 14% higher compared to the back-pressure of original scoop Geometry 1. Design 3 (D3) has a considerable increase in the back-pressure compared to the original scoop geometry. The reason for such a drastic increase is the blockage of the free outflow of the exhaust mixture created by the scoop plates facing over the exhaust outlet.

Figure 8.9 describes the influence of the scoop designs on the overall scoop resistance. A general observation shows that the pressure drag of all the new scoop designs is lower than that of the original scoop geometry. On contrary, the skin-friction of the new designs are considerably higher to that of the original scoop.

The decrease in pressure drag is due to the reduced frontal area of the new scoop designs. While the increased skin friction is the result of the overall increase in the surface area of these scoops.

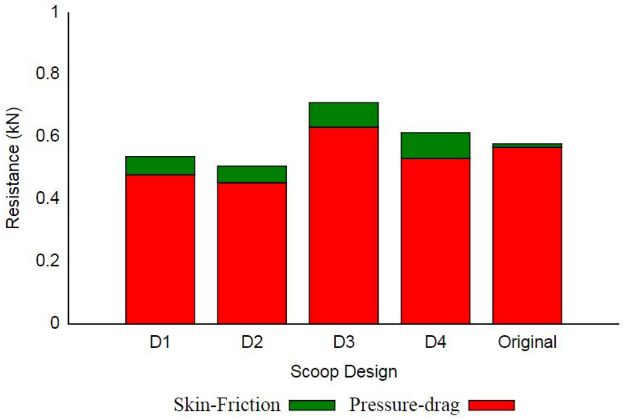

Figure 8.9: Total resistance

8.2.2. Flow development

Figure 8.10 shows the contaminated area of the hull due to the exhaust mixture for the alternate scoop designs. The new designs result in a significantly high contaminated area on the hull as compared to the original scoop. Design 2 (D2) shows the highest contamination on the hull. The large contamination area can be seen in Figure 8.11a.

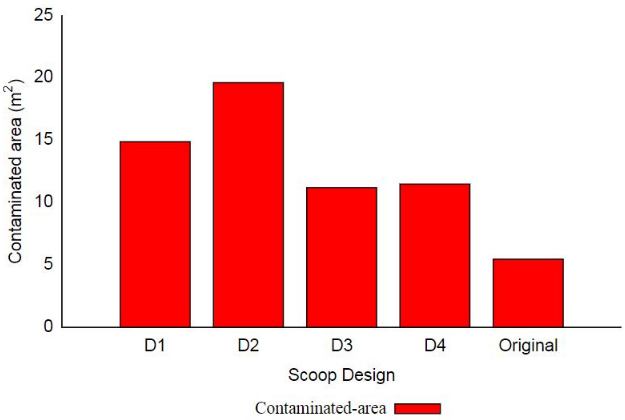

Figure 8.10: Contaminated area on hull

Design 3 was devised to eliminate the water-column over the exhaust outlet. As observed in Figure 8.11b, the scoop is successful in retaining a flat free-surface over the exhaust outlet. Furthermore, the immediate escape of the exhaust gas is delayed and the formation of exhaust spray is eliminated providing a lower contaminated area on hull.

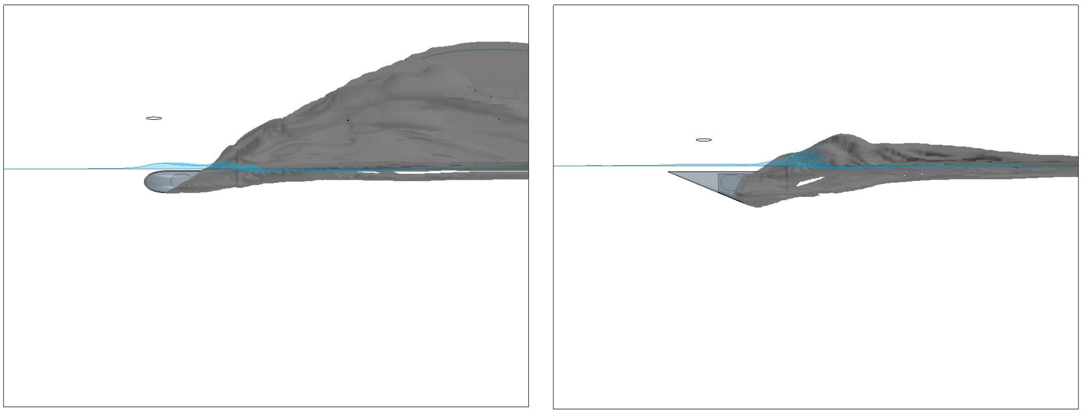
(a) Design 2 (b) Design 3

Figure 8.11: Side view - Flow development around the new scoop design

As initially expected, the new scoop designs achieved the criteria for low pressure drag but could not meet the desired back-pressure condition. Additionally, the skin friction and the contaminated area were relatively high for all new scoop designs. Thus, the new scoop designs do not provide a significant improvement over the existing scoop.

9
Discussion, Conclusions & Recommendations

This chapter compares the results of the selected scoop designs. The results will be discussed and the broader trends will be identified. Furthermore, the discussion will provide the use cases for the selected scoop designs. The chapter ends with the conclusions for the entire research work and further recommendations to expand the scoop designs.

9.1. Results discussion

As established from the results of Chapter 6 and Chapter 7, scoop geometry 1 is performing better than scoop geometry 2. Furthermore, the modified scoop geometry 1 obtained from the analysis mentioned in Chapter 7 provides significant improvements over the existing designs. Also, the conceptual air-blown exhaust scoop mentioned in Chapter 8 has some considerable advantages over the existing scoop designs. The above mentioned scoop designs will be used in this section to show their advantages and limitations over the existing scoop geometries. The scoops shown in Figure 9.1.

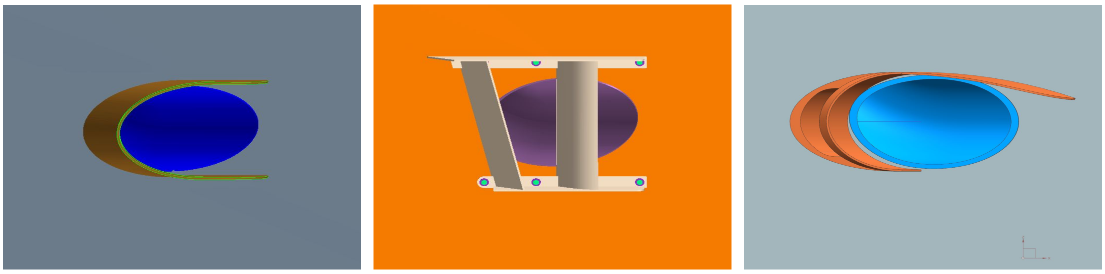
(a) Scoop geometry 1 (b) Modified geometry 1 (c) Air-blown exhaust scoop

Figure 9.1: Side view of different scoop geometries

Exhaust back-pressure

Figure 9.2 provides a comparison for the exhaust back-pressure obtained with different scoop geometries. modified scoop geometry 1 has an approximate increase of 5% in back-pressure over the entire velocity range. The air-blown exhaust scoop shows a significant advantage over the scoop geometry 1. The back-pressure stays almost the same at low velocities. However, the back-pressure reduces by approximately 12% in the range of velocities from 10 knots to 15 knots. This is beneficial as most of the Feadship yachts operate within this range of velocity in cruise condition. At the maximum velocity, the back-pressure is reduced by approximately 6% compared to Scoop geometry 1.

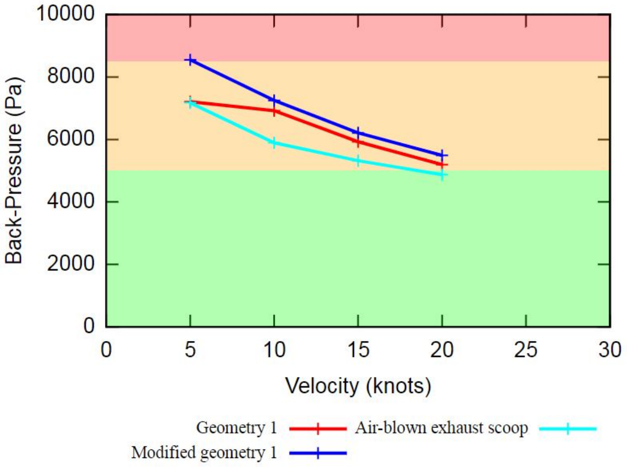

Figure 9.2: Back-pressure

Total scoop resistance

Figure 9.3 presents the total scoop resistance for different scoop geometries. At a low velocity, the increase in resistance is negligible between the different scoop geometries. However, the resistance of modified scoop geometry 1 is roughly 35% higher than that for scoop geometry 1 in the mid-range velocities. At the highest velocity, the resistance is increased by roughly 40% for the above mentioned scoops.

For the air-blown exhaust scoop, the increase in resistance is approximately 25% compared to scoop geometry 1 in the mid-range velocities. At the highest velocity, this increase is approximately 30%. However, the resistance of this scoop is roughly 10% lower compared to the modified scoop geometry 1 over the entire velocity range.

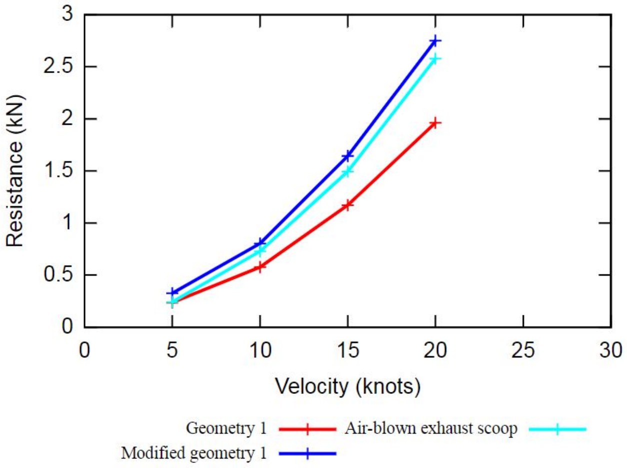

Figure 9.3: Total scoop resistance

Effect of submergence depth

Figure 9.4 presents the influence of the submergence depth on the back-pressure of the different scoop geometries. The difference in back-pressure between scoop geometry 1 and modified scoop geometry 1 is negligible over the given range of velocities. However, the air-blown exhaust scoop shows a significant advantage over the other scoops.

At low velocity, the back-pressure for the air-blown exhaust scoop remains similar to that of scoop geometry 1. However, as the velocity increases, the back-pressure obtained with the air-blown exhaust scoop shows a reduction of approximately 14% compared to scoop geometry 1. This expands the operating range of the air-blown exhaust scoop as it can provide a similar back-pressure condition like scoop geometry 1 at an increased submergence depth.

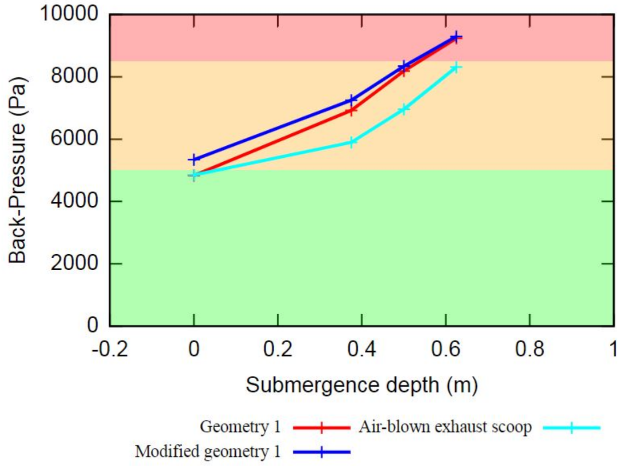

Figure 9.4: Submergence depth

Exhaust contamination on hull

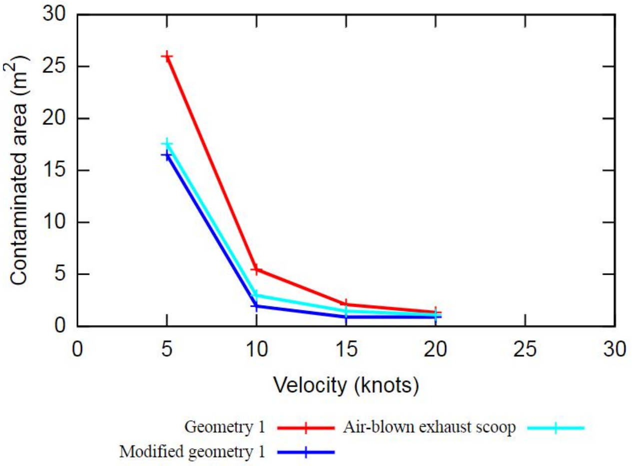

Figure 9.5: Exhaust contaminated area on hull

Figure 9.5 shows a measure of the hull contamination caused by the exhaust gas mixture for different scoop geometries. The contaminated area on the hull for both the modified scoop geometry 1 and the air-blown exhaust scoop is approximately the same. However, it is significantly lower compared to scoop geometry 1.

At low velocities, the contaminated area is roughly 32% smaller compared to that of Scoop geometry 1. In the mid-range velocities, this difference is approximately 53%.

Since, most of the Feadship yachts have a cruising velocity in this range, this reduction in contaminated area provides a significant benefit over scoop geometry 1. However, at high velocities, the contamination area is almost the same for both the scoop geometries.

Flow development around the hull

Figure 9.6 shows a top view of the spread of exhaust gas mixture around the hull for different scoop geometries at 10 knots. For scoop geometry 1, the exhaust mixture stays in contact with the hull throughout its length. This leads to a large contaminated area on the hull as discussed in the previous section. For modified scoop geometry 1, a stream of water prevents the exhaust mixture from contacting the hull leading to a low contamination. In case of the air-blown exhaust scoop, a similar effect is observed. Here the bulk of exhaust mixture is diverted away from the hull.

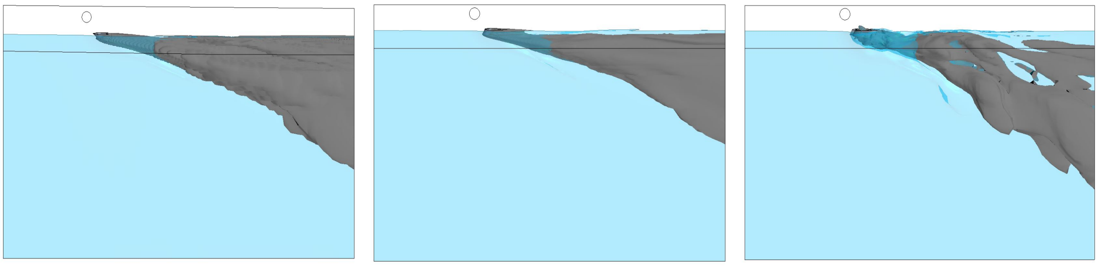
(a) Scoop geometry 1 (b) Modified geometry 1 (c) Air-blown exhaust scoop

Figure 9.6: Top view at 10 knots

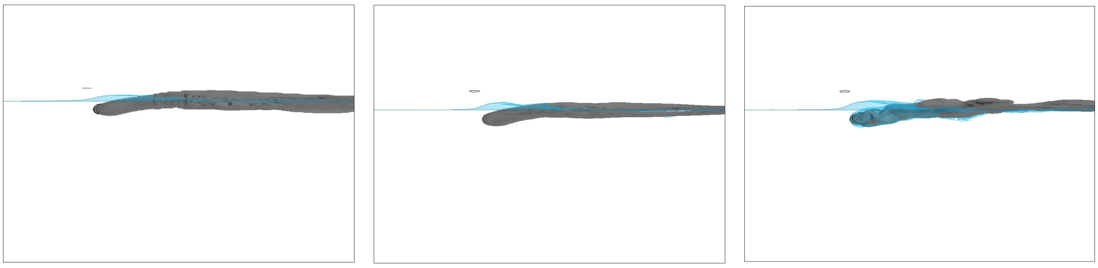
(a) Scoop geometry 1 (b) Modified geometry 1 (c) Air-blown exhaust scoop

Figure 9.7: Side view at 10 knots

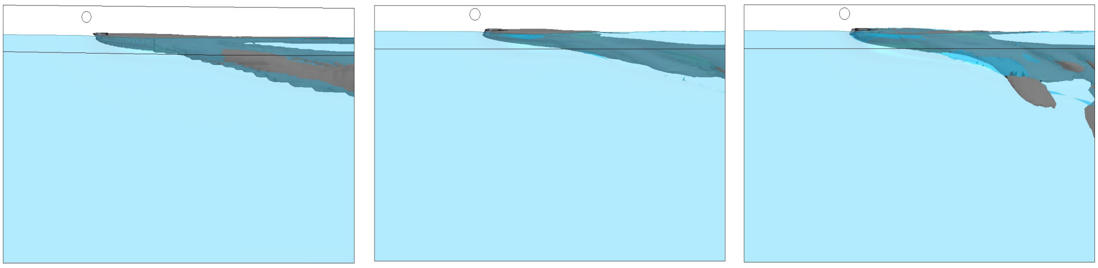
(a) Scoop geometry 1 (b) Modified geometry 1 (c) Air-blown exhaust scoop

Figure 9.8: Top view at 20 knots

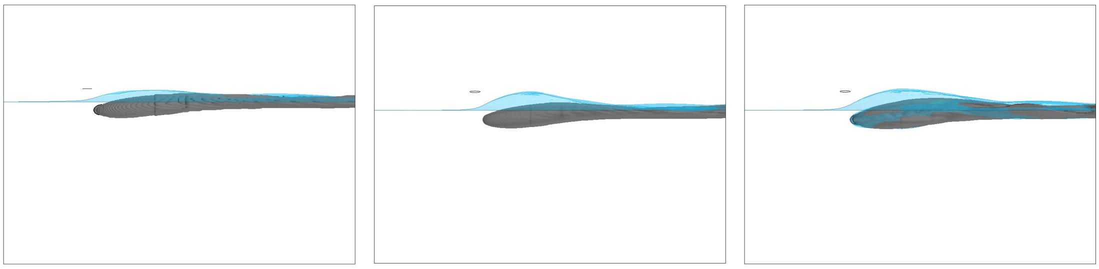
(a) Scoop geometry 1 (b) Modified geometry 1 (c) Air-blown exhaust scoop

Figure 9.9: Side view at 20 knots

Figure 9.7 shows a side view of the spread of the exhaust gas mixture at 10 knots. From the side view, the spread looks almost identical for scoop geometry 1 and modified scoop geometry 1 with a presence of a small water-column above the underwater outlet. However, for the air blown exhaust scoop, the flow looks disturbed due to the presence of air blowing from the outlet.

Figure 9.8 shows a top view of the spread of the exhaust gas mixture at 20 knots. Here, the spread of the exhaust mixture looks more constrained compared to 10 knots. For scoop geometry 1, a small stream of exhaust mixture stays attached to the hull thereby leading to hull contamination. In case of modified scoop geometry 1, the exhaust gas spread stays submerged in the sea-water and away from the hull. A similar pattern can be observed for the air-blown exhaust scoop.

Figure 9.9 shows a side view of the spread of the exhaust gas mixture at 20 knots. The pattern observed here is similar to that observed at 10 knots. However, the height of water-column above the underwater outlet for modified scoop geometry 1 and the air-blown exhaust scoop is higher compared to that of 10 knots. Such a high water-column makes sure that the exhaust mixture stays submerged.

9.2. Advantages and limitations

Modified scoop geometry 1 has a substantial advantage over scoop geometry 1 in terms of exhaust flow management around the hull. This scoop geometry makes sure that the majority of exhaust gas mixture is diverted away from the hull. This helps to provide a low contamination area on the hull. Furthermore, the modified geometry provides a considerable advantage in performance when the scoop is only partially submerged by maintaining a constant flow of water above the scoop. This provides a suitable mixing condition for the exhaust mixture. Additionally, the geometry is simple to manufacture with low production costs.

However, there are some limitations with the modified scoop geometry 1. This geometry is not suitable for a deep submergence depth operation as the hydrostatic pressure would increase the back-pressure and resistance excessively. This would make it inoperable at excessive submergence depth. Thus, modified scoop geometry 1 provides excellent performance in the partially submerged conditions and at a low submergence depth.

The air-blown exhaust scoop proved efficient in controlling the exhaust back-pressure. This scoop has a significant advantage over Scoop geometry 1 as it is easily operable at a large submergence depth. Furthermore, it provides similar exhaust flow management around the hull like modified scoop geometry 1. This helps in achieving a low contamination area on the hull.

On contrary, this scoop is not suitable for partial or low submerged conditions. This is due to the high contamination of hull facilitated by the air blowing out of the scoop at low yacht velocities. This can be prevented by operating the scoop with closed air outlet at a partial or low submergence depth. Furthermore, this scoop requires an internal air pump which makes the manufacturing process more complex and relatively more costly.

9.3. Conclusions

The main objective of this research was to provide design recommendations for the scoop geometry which can help control excessive exhaust back-pressure. Additionally, the new geometry should be able to reduce hull contamination alongside having a low resistance geometry. Using the multiphase numerical simulation, different scoop geometries were investigated.

In Chapter 5, the numerical model was validated with a qualitative and a quantitative approach using the data obtained from a sea-trial of a Feadship yacht. The numerical model provided a good prediction of the wave profile and the exhaust spray around the hull through a qualitative approach. Additionally, the interaction of the exhaust plume with the hull was predicted accurately. Through a quantitative approach, the results for the height of the exhaust spray were validated against the sea-trial data. For the maximum back-pressure prediction, it was only possible to obtain an approximate value with this numerical model.

The two baseline geometries of the scoop (scoop geometry 1 and scoop geometry 2) already in use by Feadship were analyzed in Chapter 6. The advantage of having a scoop in front of the underwater outlet was clearly shown in this study. Furthermore, it was discovered that the smooth shape of scoop geometry 1 redirects the flow in a better way than scoop geometry 2 and also prevents the formation of air pockets. Thus, scoop geometry 1 was chosen for further modification and analysis.

In Chapter 7, two important parameters were identified to vary in scoop geometry 1 namely the deflection angle of the scoop plate and the two axis of the elliptical scoop geometry. It was concluded that the scoop geometry 1 with a deflection angle of 60^o had an optimal performance. Additionally, no significant benefits were observed in terms of back-pressure or flow development by varying the elliptical radii.

A conceptual design, namely the air-blown exhaust scoop using modified scoop geometry 1 was prepared in Chapter 8. This new concept provided significant improvements over the existing scoop geometry in terms of a low back-pressure at large submergence depths and a low contamination area. Furthermore, some new and radical scoop geometries were analyzed. These geometries showed a low resistance but could not satisfy the low back-pressure criteria.

Taking all the geometries into account, a final conclusion can be drawn. The most important parameter to regulate the flow around the scoop and to control the back-pressure is the deflection angle. Combining this improvement with the air-blown exhaust scoop satisfies the main objectives of this research study.

9.4. Recommendations

For further research, there are three main areas which can be investigated in more detail.

Internal exhaust pressure

The back-pressure value is dependent on the internal pressure loss throughout the exhaust system. An in-depth analysis of the internal system would help to accurately determine the internal pressure losses. This will enable one to calculate the back-pressure more accurately.

Furthermore, the internal system includes a sea-water injector to regulate the temperature of the exhaust gas. Currently, only limited amount of data is available regarding the effect of this system on the properties of the exhaust gas and sea-water mixture. A detailed study about the water injector and its effects could provide a more reliable value for temperature and density of the exhaust gas and sea-water mixture. This would eventually result in more accurate mass flow rate of the exhaust mixture through the underwater outlet and a more precise value for the pressure loss in the water injector system.

Experimental research

Currently, the full scale model of new geometries are analyzed in a simplified domain using CFD.

Firstly, it is highly recommended to scale the geometry and perform CFD analysis and towing tank tests. This would help to obtain a validation procedure for new scoop geometries.

Secondly, there is need to perform sea-trials with new scoop geometries. This would provide insights about the interaction of the exhaust flow from the scoop with the bow and stern waves. These results could lead to a further improvement in the scoop geometries. Furthermore, it would provide information regarding the adjustments to be made in placing the underwater outlet to gain optimal scoop performance.

Effect of bubble size

According to the research carried out by Talaia [35], it was concluded that the terminal velocity of the bubble is directly proportional to the equivalent diameter of the bubble. Currently, the underwater exhaust outlet disperses the exhaust gas in the form of large bubbles which looks like a churn flow. As per the study of Talaia [35], large size bubbles have a higher terminal velocity, thereby they escape the sea-water quickly. This acts as a deterrent to provide a better mixing condition with sea-water.

A possible solution for this problem has been provided in the research carried out by Kalbfleisch [14]. It was concluded that a mesh type bubble breaker is effective in reducing the size of the air bubbles in a two-phase flow. Unfortunately, the VOF model in Star-CCM+ is only suited for simulations of flows where each phase constitutes a large structure, with a relatively small total contact area between the phases due to its numerical efficiency. Thus, it is not possible to simulate the formation of bubbly flow and study the effect of bubble size simultaneously in such a large computational domain.

Although the effect of a bubble breaker cannot be analyzed for such a computational domain in Star-CCM+, it would be advisable to experimentally study its effect. It could be attached to the underwater outlet of a yacht during sea-trials. Such data obtained from sea-trails can help to understand the effect of a bubble breaker on the exhaust gas spray and the mixing conditions.

Bibliography

[1] Anderson, J. D. [2013], *Fundamentals of Aerodynamics*, 3rd edn, McGraw-Hill, New York.

[2] Bedos, A. [2017], *Effect of sea and weather conditions on superyacht speedtrial results*, M.Sc. Thesis. ENSTA Bretagne.

[3] Crowe, C. T., Schwarzkopf, J. D., Sommerfeld, M. and Tsuji, Y. [1998], *Multiphase Flows with Droplets and Particles*, CRC Press, Boca Raton.

[4] Delvoye, S. [2009], *Simulation and analysis of the flow around an underwater exhaust with FreSCo*, M.Sc. Thesis. Institut des Sciences de l'Ingénieur de Toulon et du Var.
URL: *http://www.refresco.org/?wpdmpro=2009-msc_thesis_simondelvoye-pdf*

[5] Eca, L. and Hoekstra, M. [2006], On the influence of the iterative error in the numerical uncertainty of ship viscous flow calculations, *in* '26th Symposium on Naval Hydrodynamics', Rome, Italy.
URL: *http://www.marin.nl/web/Publications/Publication-items/On-the-Influence-of-the-Iterative-Error-in-the-Numerical-Uncertainty-of-Ship-Viscous-Flow-Calculations.htm*

[6] Eca, L. and Hoekstra, M. [2014], 'A procedure for the estimation of the numerical uncertainty of cfd calculations based on grid refnement studies', *Journal of Computational Physics* **262**, 104–130.

[7] Eca, L., Vaz, G. and Hoekstra, M. [2010], A verification and validation exercise for the flow over a backward facing step, *in* 'European Conference on Computational Fluid Dynamics ECCOMAS CFD', Lisbon, Portugal.

[8] Fabre, J. and Liné, A. [2018], '*Stratified Gas-Liquid Flow*'. `https://doi.org/10.1615/AtoZ.s.stratified_gas-liquid_flow` [Accessed: 28/05/2018].

[9] Feadship yachts [2018]. `https://www.feadship.nl/en/fleet` [Accessed: 05/10/2018].

[10] Ganzeveld, P. D. [2004], *Backpressure of a 'wet' underwater exhaust system*, M.Sc. Thesis. Haarlem Poly-Technical University.

[11] *Guide for the Verification and Validation of Computational Fluid Dynamics Simulations (AIAA G-077-1998)* [2002], AIAA Standard.

[12] Hewitt, G. F. [2018], '*Gas-Liquid Flow*'. `https://doi.org/10.1615/AtoZ.g.gas-liquid_flow` [Accessed: 28/05/2018].

[13] Jääskeläinen, H. [2018], '*Diesel Exhaust Gas*'. `https://www.dieselnet.com/tech/diesel_exh.php` [Accessed: 28/02/2018].

[14] Kalbfleisch, A. [2016], *The Effect Of Mesh-Type Bubble Breakers On Two-Phase Vertical Co-Flow*, Master Thesis. University of Western Ontario.
URL: *https://ir.lib.uwo.ca/etd/3946*

[15] Kataoka, I. and Serizawa, A. [2018], '*Bubble Flow*'. `https://doi.org/10.1615/AtoZ.b.bubble_flow` [Accessed: 28/05/2018].

[16] Klapwijk, M. [2017], *Modeling of the exhaust plume of a submerged exhaust system*, M.Sc. Thesis. Delft University of Technology.
URL: *uuid:df3b1b02-94f6-427c-ad84-4c4342dddf57*

[17] Kulkarni, P. R., Singh, S. N. and Seshadri, V. [2005], 'The smoke nuisance problem on ships - a review', *Journal of Maritime Engineering* **147**(2).
URL: *https://doi.org/10.3940/rina.ijme.2005.a2.050257*

[18] Kunz, R., Chyczewski, T., Boger, D., Stinebring, D. and Gibeling, H. [1999], 'Multiphase cfd analysis of natural and ventilated cavitation about submerged bodies', *3rd ASME/JSME Joint Fluids Engineering Conference* .

[19] Liu, J., Shijie, Q. and Wu, D. [2015], 'Three-dimensional numerical simulation of air exhausted from submerged nozzles', *IOP Conference Series: Materials Science and Engineering* **72**.
URL: *https://doi.org/10.1088/1757-899X/72/4/042038*

[20] Marquip [2018], '*Emission Technology*'. `https://www.marquip.nl/exhaust-system-expertise/emission-technology` [Accessed: 28/02/2018].

[21] Mehta, U. B. [1991], 'Some aspects of uncertainty in computational fluid dynamics results', *Journal of Fluids Engineering* **113**(4), 538–543.
URL: *https://doi.org/10.1115/1.2926512*

[22] Menter, F. R. [1993], 'Zonal two equation $k - \omega$ turbulence models for aerodynamic flows', *AIAA Journal* .
URL: *https://doi-org.tudelft.idm.oclc.org/10.2514/6.1993-2906*

[23] Menter, F. R. [1994], 'Two-equation eddy-viscosity turbulence modeling for engineering applications', *AIAA Journal* **32**(8), 1598–1605.
URL: *https://doi-org.tudelft.idm.oclc.org/10.2514/3.12149*

[24] Pas, S. [2016], *The influence of y+ in wall functions applied in ship viscous flows*, University of Twente.

[25] Perry, R. H. [1984], *Perry's Chemical Engineers' Handbook*, McGraw-Hill, New York, 6th edition.

[26] Pope, S. B. [2000], *Turbulent Flows*, Cambridge University Press.

[27] Rijpkema, D. [2008], *Numerical Simulation of Single-Phase and Multi-Phase Flow over a NACA 0015 Hydrofoil*, M.Sc. Thesis. Delft University of Technology.
URL: $http : //www.refresco.org/?wpdmpro = 2008{-}msc\_thesis\_douwerijpkema{-}pdf$

[28] Rijpkema, D. and Vaz, G. [2011], Viscous flow computations on propulsors: Verification, validation and scale effects, *in* 'International Conference on Developments in Marine CFD 2011', Royal Institution of Naval Architects (RINA), London, UK, pp. 35–47.

[29] Roache, P. J. [1998], *Verification and Validation in Computational Science and Engineering*, Hermosa.

[30] Rosetti, G. F., Vaz, G. and Fujarra, A. L. [2012], Urans calculations for smooth circular cylinder flow in a wide range of reynolds numbers: Solution verification and validation, *in* 'Proceedings of the ASME 2012 31st International Conference on Ocean, Offshore and Arctic Engineering', Rio de Janeiro, Brazil.

[31] Sapra, H., Godjevac, M., Visser, K., Stapersma, D. and Dijkstra, C. [2017], 'Experimental and simulation-based investigations of marine diesel engine performance against static back pressure', *Applied Energy* **204**, 78–92.
URL: *https://doi.org/10.1016/j.apenergy.2017.06.111*

[32] Slater, J. W. [2008], '*Uncertainty and Error in CFD Simulations*'. `https://www.grc.nasa.gov/www/wind/valid/tutorial/errors.html` [Accessed: 28/02/2018].

[33] Spalart, P. R. and Allmaras, S. R. [1992], A one-equation turbulence model for aerodynamic flows, *in* '30th Aerospace Sciences Meeting and Exhibit, Aerospace Sciences Meetings', Nevada, USA.
URL: *https://doi-org.tudelft.idm.oclc.org/10.2514/6.1992-439*

[34] *Star-CCM+ User Guide* [2012], Siemens PLM software.

[35] Talaia, M. [2007], 'Terminal velocity of a bubble rise in a liquid', *World Academy of Science, Engineering and Technology* **28**.

[36] Tauzia, X., Chesse, P. and Maiboom, A. [2008], 'Simulation study of a ship's engine behaviour running with a periodically immersed exhaust', *Proceedings of the Institution of Mechanical Engineers, Journal of Engineering for the Maritime Environment* **222**(4), 195–205.
URL: *https://doi.org/10.1243/14750902JEME117*

[37] Underwater Marine Exhaust Systems [2015]. `https://www.sbmar.com/articles/underwater-marine-exhaust-systems/` [Accessed: 26/02/2018].

[38] Valentine, D. T. [1993], 'Reynolds-averaged navier-stokes codes and marine propulsor analysis', *Technical report, DTIC Document* .

[39] White, F. M. [2006], *Viscous Fluid Flow*, McGraw-Hill, New York.

[40] Wilcox, D. C. [1998], *Turbulence Modeling for CFD*, 2nd edn, DCW Industries Inc.

A

Numerical formulation in STAR-CCM+

A.1. Navier-Stokes equations

The Navier-Stokes equations are used to simulate the flow around the exhaust scoop. These equations consist of the continuity equation (mass conservation law) and the momentum equation (Newton's second law) which are described below. The derivation for the Navier-Stokes equation is provided in detail by Anderson, [1]. The continuity equation states that the mass is conserved in the fluid domain and it is given by equation A.1.

$$\frac{\partial \rho}{\partial t} + \nabla \cdot (\rho V) = 0 \cdot \tag{A.1}$$

The principle of conservation of momentum states that the rate of change of momentum in the fluid particle is equal to the sum of the forces on that particle. Body and surface forces are the prime contributors to these forces. The momentum equation for fluid flow is shown in equation A.2.

$$\begin{gathered}\frac{\partial \rho u}{\partial t} + \nabla \cdot (\rho u V) = \frac{\partial p}{\partial x} + p f_x + (F_X)_{viscous} \\ \frac{\partial \rho v}{\partial t} + \nabla \cdot (\rho v V) = \frac{\partial p}{\partial y} + p f_y + (F_Y)_{viscous} \cdot \\ \frac{\partial \rho w}{\partial t} + \nabla \cdot (\rho w V) = \frac{\partial p}{\partial z} + p f_z + (F_Z)_{viscous}\end{gathered} \tag{A.2}$$

A.2. RANS equations

Several numerical methods are available to solve a fluid flow problem. Direct Numerical Solution (DNS) solves all the turbulent scales in the fluid domain using the Navier-Stokes equations. Due to the large requirement of the computational effort, it is not possible to use this method to solve the flow around the exhaust scoop. In order to reduce the computational effort, modelling of turbulence is required. One such method is Large Eddy Simulation (LES) where the large scales of the turbulence are resolved everywhere in the fluid domain, and the small-scale motions are modeled. Nonetheless, it will require a large computational effort for scoop design. Thus, an additional simplification is required using Reynolds Averaged Navier-Stokes (RANS) equations.

In the approach involving RANS equations, the mean flow is calculated by solving the Navier-Stokes equations. The arising turbulent fluctuations are modelled using turbulence closure models.

In Star CCM+, to obtain the Reynolds-Averaged Navier-Stokes equations, each solution variable ϕ in the instantaneous Navier-Stokes equations is decomposed into a mean, or averaged, value $\bar{\phi}$ and a fluctuating component $\phi^{'}$, [34]:

$$\phi = \bar{\phi} + \phi^{'} , \tag{A.3}$$

where ϕ represents velocity components, pressure, energy, or species concentration.

The averaging process may be thought of as time averaging for steady-state situations and ensemble averaging for repeatable transient situations. The resulting equations for the mean quantities are essentially identical to the original equations. RANS equations can be written as:

$$\rho \frac{D\overline{u}}{Dt} = \rho g - \nabla \overline{p} + \nabla \cdot \tau_{ij} , \tag{A.4}$$

with

$$\tau_{ij} = \mu \left(\frac{\delta u_i}{\delta x_j} + \frac{\delta u_j}{\delta x_i} \right) - T_t \cdot \tag{A.5}$$

The first term in τ_{ij} represents Newtonian viscous stress while the second term represents the turbulent stress tensor, [39]. The tensor quantity T_t in equation A.5 is known as the Reynolds stress tensor, which is given by:

$$T_t = -\rho \begin{pmatrix} \overline{u\prime u\prime} & \overline{u\prime v\prime} & \overline{u\prime w\prime} \\ \overline{u\prime v\prime} & \overline{v\prime v\prime} & \overline{v\prime w\prime} \\ \overline{u\prime w\prime} & \overline{v\prime w\prime} & \overline{w\prime w\prime} \end{pmatrix} \cdot \tag{A.6}$$

The tensor term in the above equation represents the mean transport of the fluctuating momentum by turbulent velocity fluctuations, [39]. The turbulence models are required to model the Reynolds stress tensor (T_t) in terms of mean flow quantities thereby providing closure to the governing equations. The closure models are discussed in detail in Section A.3.

The detailed derivation of the RANS equation is provided by Valentine, [38].

A.3. Turbulence models

Turbulence models provide closure relations for the RANS equations to solve for the transport of mean flow quantities. There are four major classes of turbulence models present in STAR-CCM+.

1. Spalart-Allmaras models
2. $k - \epsilon$ models
3. $k - \omega$ models
4. Reynolds stress transport models

Spalart-Allmaras models are a good choice for applications in which the boundary layers are largely attached and separation is mild if it occurs. Typical examples would be flow over a wing, fuselage or other aerospace external-flow applications. The Spalart-Allmaras models for RANS equations are not suited to flows that are dominated by free-shear layers, flows where complex recirculation occurs (particularly with heat transfer), or natural convection, [33].

$k-\epsilon$ models provide a good compromise between robustness, computational cost and accuracy. However, the model performs poorly for complex flows involving severe pressure gradient and strong streamline curvature like the hull, [22].

$k-\omega$ models are similar to $k-\epsilon$ models where the two transport equations are solved, but differ in the choice of the second transported turbulence variable.

In this model, apart from the transport equation for the turbulent kinetic energy k, an equation for the specific dissipation rate

$$\omega = \frac{\epsilon}{k}, \tag{A.7}$$

is solved, instead for the dissipation rate ϵ, [40].

The disadvantage of the $k-\omega$ model, in its original form, is that the boundary layer computations are sensitive to the values of in the free stream. This translates into extreme sensitivity to inlet boundary conditions for internal flows, a problem that does not exist for the other models.

The problem of sensitivity to free-stream/inlet conditions was addressed by Menter, [23], who recognized that the ϵ transport equation from the standard $k-\epsilon$ model could be transformed into an ω transport equation by variable substitution. Menter, [22], also introduced a modification to the linear constitutive equation and named the model containing this modification the Shear Stress Transport (SST) $k-\omega$ model.

Reynolds Stress Transport (RST) models are the most complex and computationally expensive models offered in STAR-CCM+. Also, the model carries significant computational overhead. Seven equations must be solved (as opposed to the two equations of a $k-\epsilon$ or a $k-\omega$ model), [34]. Thus, considering the limited computational resources and time, RST models will be avoided in this thesis project.

Taking into account the highly accurate predictions of flow separation under the adverse pressure gradients for complex geometry by SST ω model, [23], and previously established results at De Voogt Naval Architects, the simulations will make use of the mentioned model in this research. The SST $k-\omega$ model will provide an optimal balance between accuracy and performance.

A.4. Multiphase model

Star CCM+ provides various multiphase models within the two frameworks, namely the Langrangian and the Euler framework, [34].

- The Euler - Lagrangian model: This model permits solving an arbitrary number of dispersed phases, each modeled in a Lagrangian framework. In a Lagrangian framework, [3], particle-like elements that are known as parcels are followed through the continuum. This method solves Navier-Stokes equations (Euler equations) for the continuous phase and Lagrangian equation of motion for individual particles. The method is mainly used to follow the motion of a rising bubble, for liquid fuel combustion or to model the granular flow. However, the method is not very accurate for complex geometry due to the large deformation in grid to track the particles. Thus, the method will not be used in this research due to the above mentioned limitation.

- The Euler - Euler model: In the formulation of this model, each distinct phase has its own set of conservation equations. The volume fraction of the dispersed phase is tracked with an additional transport equation. Furthermore, the model requires that the dispersed particles, bubbles, or droplets are much smaller than the grid size. The disadvantage lies in the fact that the model solves the Navier-Stokes equations for each phase which demands high computational cost. Thus, for the current study, this model will not be used.

- Mixture model: In this model, mass, momentum, and energy are treated as mixture quantities rather than phase quantities. Furthermore, it requires solving transport equations for the mixture as a whole, and not for each phase separately. The model is computationally more efficient than models that simulate each phase separately. The mixture model is intended for use as a replacement for the more computationally expensive Euler-Euler model. However, in some cases, large variations between phase quantities are not well-resolved. In the current study, we will make use of a specialized mixture model called Volume Of Fluid (VOF) model. The ability of the model to simulate stratified flow in complex geometry and it availability for three different phase makes it a perfect model for the current study.

A.4.1. Volume Of Fluid (VOF) model

In order to simulate the multiphase flow containing free-surfaces between sea-water and air and the introduction of exhaust gas, it is necessary to incorporate the Volume of Fluid (VOF) model.

The VOF model is a simple multiphase model. It is suited to simulate flows of several immiscible fluids on numerical grids capable of resolving the interface between the phases of the mixture. In mathematical terms, the VOF model utilizes a Eulerian framework in their formulation, [34]. Due to its numerical efficiency, the model is suited for simulations of flows where each phase constitutes a large structure, with a relatively small total contact area between phases. A good example of this type of flow would be the ship motion in calm sea-water, where the free surface always remains smooth. In the region of underwater exhaust outlet, the model would require a fine mesh to capture the exhaust gas and reduce the modelling error.

The equations are solved for an equivalent fluid whose physical properties are calculated as functions of the physical properties of its constituent phases and their volume fractions.

$$\rho = \sum_i \rho_i \alpha_i \,, \tag{A.8}$$

$$\mu = \sum_i \mu_i \alpha_i \,, \tag{A.9}$$

$$c_p = \sum_i \frac{(c_p)_i \rho_i}{\rho} \alpha_i \,, \tag{A.10}$$

where

$\alpha_i = \frac{V_i}{V}$ is the volume fraction and

ρ_i, μ_i and $(c_p)_i$ are the density, molecular viscosity and specific heat of the i^{th} phase respectively.

A.5. Wall model

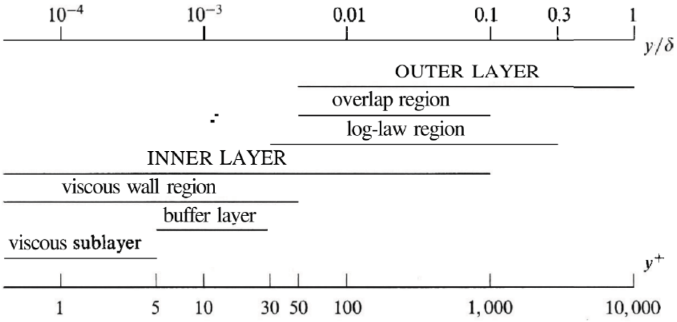

Figure A.1: Viscous wall region [26]

Walls are a source of vorticity in most flow problems of practical importance. Therefore, an accurate prediction of flow and turbulence parameters across the wall boundary layer is essential. The inner region of the boundary layer is presented in Figure A.1.

The viscous sublayer in contact with the wall is dominated by viscous effects and is almost laminar. The mean flow velocity only depends on the fluid density, viscosity, distance from the wall, and the wall shear stress. The log-law layer is dominated equally by viscous and turbulent effects. The buffer layer is a transitional layer between the viscous sublayer and the log-law layer, [26].

The non-dimensional wall distance y^+ can be used to define the extent of the sub-layers.

$$y^+ = \frac{y u^*}{\nu} \,, \tag{A.11}$$

$$u^* = \sqrt{\frac{\tau_w}{\rho}} \,. \tag{A.12}$$

In Figure A.1, the relation between the boundary layer thickness and the y^+ variable is explained. In the boundary layer three separate regions can be distinguished. In the viscous sublayer ($y^+ < 5$) the Reynolds shear stress is negligible compared with viscous stress. Between the viscous sublayer and the log-law region sits the buffer layer (5<y^+<30). For $y^+ > 30$ the log-law is valid and performs well for high Re flows where the turbulent boundary layer is fully developed [26].

In order to simulate the boundary layer with the least amount of computational resources, a wall model and the prism layer mesher is used in Star-CCM+. Prism layers allow the solver to resolve near wall flow accurately, which is critical in determining not only the forces and heat transfer on walls, but also flow features such as separation. Separation in turn affects integral results such as drag or pressure drop. Using a prism layer mesh allows you to resolve the viscous sublayer directly if the turbulence model supports it (low $y^+ \approx 1$). Alternatively, for coarser meshes it allows the code to fit a wall function more accurately (high $y^+ > 30$).

A.6. Numerical uncertainty

Numerical models are subjected to error similar to the experimental work, [29]. As per the definition provided in [11], error is defined as a recognizable deficiency in any phase or activity of modeling and simulation that is not due to lack of knowledge. This definition implies that the deficiency is identifiable upon inspection. The numerical errors can be classified into four types which are described in the sections below, [32].

Physical modelling error

Physical modelling errors are those due to uncertainty in the formulation of the model and deliberate simplifications of the model. These errors deal with the continuum model only. Even when a physical process is known to a high level of accuracy, a simplified model may be used within the CFD code for the convenience of a more efficient computation, [21]. The modelling error can be estimated by validating with the experimental results.

Computer round-off error

Computer round-off errors develop with the representation of floating point numbers on the computer and the accuracy at which numbers are stored. With advanced computer resources, numbers are typically stored with 16, 32, or 64 bits. Round-off errors are not considered significant when compared with other errors, [32].

Iterative convergence error

The iterative convergence is caused due to the non-linearity of the system of partial differential equations in CFD, [5]. Some of the sources of non-linearity in the RANS equations are the convective terms and the non-linear production and dissipation terms of the turbulence closure model. The iterative error could be minimized as far as the computation power permits. Although, it is difficult to achieve suitable level of convergence for the complex turbulent flow. Furthermore, the computation time required to attain minimum level of iterative error may be significantly higher than to obtain an acceptable level of iterative error. In order to have a minimal effect of the iterative error, it should be atleast two or three order smaller than discretization error, [5, 6].

In Star CCM+, the RMS (Root Mean Squared) value of a residual for all cells is determined from:

$$R_{rms} = \sqrt{\frac{1}{n}\sum_{n} r^2}\,, \tag{A.13}$$

where n is the number of cells, [34].

As the residuals can vary widely in absolute value, by default a normalized residual R_{pres} is used. It is determined as:

$$R_{pres} = \frac{R_{rms}}{R_{norm}}\,. \tag{A.14}$$

The normalization value R_{norm} is selected automatically in Star CCM+ as follow:

$$R_{norm} = max[|R_1|, |R_2|, ..., |R_m|]\,, \tag{A.15}$$

where R_1,R_2,...,R_m are residuals at each iteration.

Here m is the normalization number property and by default it is kept to 5 in Star CCM+. This setting removes the influence of the initialization values (reflected in R_1,R_2) but provides a sensible value for observing convergence that does not change after every iteration. The term R_{pres} is similar to the L_2 norm described by Eca and Hoekstra, [5]. It is the most appropriate norm to estimate the iterative error.

Discretization error

Discretization errors are those errors that occur from the representation of the governing flow equations and other physical models as algebraic expressions in a discrete domain of space (finite-difference, finite-volume, finite-element) and time, [32]. The discrete spatial domain is known as the grid or mesh. The temporal discreteness is manifested through the time step taken.

Discretization error is estimated based on the method given by Rosetti et al. [30]. This method is similar to the process given by Eca and Hoekstra, [5], but it is extented for the unsteady simulations. The method used here requires at least five data points to estimate the discretization error. This requires solving at least five calculations with different time-steps and mesh size.

As explained in Section 4.2, to keep the temporal discretization error minimal, a dynamic time-step formulation is used in the simulation. To estimate the spatial discretization error, mesh sensitivity tests will be carried out.